

Cryogenic Micropunching of Polymeric Films for Tissue Engineering Applications

A dissertation submitted by

Amrit Sagar

in partial fulfillment of the requirements for the degree of

Doctor of Philosophy

in

Mechanical Engineering

Tufts University

February 2015

Adviser: Prof. Thomas P. James

Abstract

Three dimensional synthetic tissue scaffolds with simulated micro-vascularity can be produced by multilayer stacking of 2D porous membranes. In order to make 2D porous membranes, cryogenic micropunching of thin Polycaprolactone (PCL) films was investigated experimentally and through finite element simulation using DEFORM 3D. Material properties of PCL, below its glass transition temperature, were determined experimentally through uniaxial compression testing of samples immersed in liquid nitrogen. Micropunching experiments were carried out for two film thicknesses, 40 μm and 70 μm . Three different die clearances were considered for each film thickness: 15%, 30%, and 45% clearance for 40 μm thick films, and 8.6 %, 17.1 %, and 25.7 % clearance for 70 μm thick films. For each experiment, the peak punching force was measured for a nominal hole diameter of 200 μm . Experimentally determined material properties of PCL were used in the finite element simulation to predict peak punching forces for comparison to experiments. The predicted peak punching forces matched the measured forces with best case error of 2% and worst case error of 31 %. Maximum achievable porosity was also investigated experimentally and through simulation by punching one hole close to a pre-existing hole and reducing the minimum web thickness between holes gradually by steps of approximately 10 μm in 70 μm thick PCL films. The maximum achievable porosity was determined to be approximately 75% for 200 μm diameter holes arranged in a hexagonally close packed pattern in 70 μm thick PCL film. Apart from PCL, thin copper foils were punched and peak punching force was measured and compared with the numerical results to study the predictive capability of conventional finite element simulation when feature dimensions are comparable in size to material grains. It was concluded that Crystal Plasticity Finite Element simulations are not necessary for predicting the peak punching force while micropunching copper foil for the range of die

clearances considered in the current research. Finally, a new analytical model was developed to study the effect of slanted punches on the punching force and verified by finite element analysis. An association between the instantaneous rate of shear area propagation and the punching force profile was predicted analytically and confirmed by finite element simulation.

Acknowledgement

First, I would like to thank Prof. Thomas P. James for supporting my research academically and financially. The experience of doing research with him has been very pleasant and rewarding. He is a very approachable and compassionate adviser. I would like to continue doing research with him in the future as well.

I would like to thank Prof. Anil Saigal for his constant support and suggestions within and outside the academic domain. I thank Prof. Robert D. White for his comments and suggestions for the design of the micro-punching setup. I would also like to thank Prof. William C. Messner for his input and suggestions during group meetings.

I would like to thank Jim Hoffman for generously helping me by fabricating most of the parts required for the experimental setups used in the research. I would also like to thank Vinnie Miraglia for promptly arranging different equipment and consumables for the experiments whenever needed.

I would like to thank Christopher R. Nehme for spending long hours of his time in helping me with the experiments. It would have been very difficult to finish the experiments in time without his generous help. I would also like to thank Eric Schmitt for designing the micropunching machine and helping during the initial phases of experiments.

Above all, I am blessed with caring parents who have always supported me in my decisions. I extend my deepest gratitude to my parents for their invaluable love, affection, encouragement, and support.

Contents

Abstract	ii
Acknowledgement	iv
List of Tables	ix
List of Figures	x
1. Introduction.....	1
1.1. Problem Statement	1
1.2. Purpose of the Study	3
1.3. Research Objectives.....	3
1.4. Hypothesis	4
1.5. Punching Process Terminology	4
2. Survey of Literature	7
2.1. Tissue Engineering.....	7
2.2. Micropunching Machines and Dies	17
2.3. Modeling Micropunching Using Finite Element Methods	25
2.4. Material Model for Polycaprolactone	33
3. Micropunching Copper Foils	39
3.1. Introduction.....	39
3.2. Materials and Methods.....	40
3.2.1. Micropunching Machine	40
3.2.2. Workpiece Characterization.....	42

3.2.3.	Die Sets	42
3.2.4.	Force Measurement.....	43
3.2.5.	Finite Element Method.....	44
3.2.6.	Workpiece Material Model	45
3.2.7.	Statistical Methods.....	48
3.3.	Results.....	48
3.3.1.	Copper Micropunching Experiments	48
3.3.2.	Finite Element Simulation Results.....	50
3.3.3.	Comparison of Modeling and Experiment.....	52
3.4.	Discussion	53
3.5.	Conclusion	56
4.	Modification of Punch Geometry	57
4.1.	Introduction.....	57
4.2.	Single Slanted Punch	59
4.2.1.	Stage I	60
4.2.2.	Stage II.....	65
4.2.3.	Stage III.....	70
4.3.	Double Slanted Punch.....	71
4.3.1.	Stage I	72
4.3.2.	Stage II.....	73
4.3.3.	Stage III.....	73

4.4.	Results.....	73
4.5.	Conclusion.....	77
5.	Material Modeling of Polycaprolactone.....	78
5.1.	Introduction.....	78
5.2.	Materials and Methods.....	81
5.2.1.	Sample Preparation.....	81
5.2.2.	Experimental Setup.....	84
5.2.3.	Procedure.....	86
5.2.4.	Calculation of Compressive True Stress and True Strain.....	88
5.3.	Results.....	92
5.4.	Discussion.....	100
6.	Cryogenic Micropunching of Polycaprolactone.....	104
6.1.	Introduction.....	104
6.2.	Material and Methods.....	106
6.2.1.	Polycaprolactone Membrane.....	106
6.2.2.	Cryogenic Micropunching Machine.....	107
6.2.3.	Male and Female Dies.....	110
6.2.4.	Finite Element Method.....	114
6.2.5.	Workpiece Material Modeling.....	120
6.2.6.	Design of Experiments.....	120
6.3.	Results.....	122

6.3.1.	Peak Punching Force.....	122
6.3.2.	Hole Quality.....	123
6.3.3.	Finite Element Simulations.....	126
6.4.	Discussion.....	137
6.5.	Conclusion.....	139
7.	Porosity Analysis of 2D Polycaprolactone Membranes.....	141
7.1.	Introduction.....	141
7.2.	Materials and Methods.....	144
7.2.1.	Micropunching in PCL.....	144
7.2.2.	Finite Element Modeling.....	144
7.3.	Results.....	145
7.4.	Discussion.....	160
7.5.	Maximum Porosity for a Porous Membrane in Tension.....	162
7.6.	Conclusion.....	165
8.	Summary.....	167
8.1.	Conclusions.....	167
8.2.	Future Scope.....	168
	References.....	171

List of Tables

Table 2.1	Example calculation of holes required to create a cartilage tissue implant by multilayer stacking.....	9
Table 2.2	Manufacturing capacity (holes per year) of one cryogenic micropunching machine	10
Table 2.3	Tensile properties of PCL reported by different researchers [21].....	35
Table 3.1	Description of dies sets used for micropunching copper foil (25 μm thick)..	42
Table 3.2	Material parameters for annealed copper [89]	46
Table 3.3	Comparison of measured hole sizes (mean +/- SD).....	49
Table 3.4	Measure of statistical significance (p values) for burr ring outside diameter	55
Table 5.1	Specimen dimensions for different aspect ratios	86
Table 5.2	Properties of PCL at room temperature based on compressive testing.....	94
Table 5.3	Properties of PCL from compression tests in liquid nitrogen ($l/d = 1.5$).....	98
Table 5.4	Properties of PCL from compression tests in liquid nitrogen ($l/d = 1.0$).....	99
Table 6.1	Summary of punching forces for a pilot study.....	121
Table 7.1	Summary of experimental results (200 μm diameter holes, 70 μm thick PCL)	154
Table 7.2	Summary of FE simulation results (200 μm diameter holes, 70 μm thick PCL)	155

List of Figures

Figure 1.1	Schematic of a typical punching or blanking process [5].....	5
Figure 1.2	Typical punched hole profile. Figure courtesy: [4]	6
Figure 2.1	Continuous widening of the gap between number of patients in waiting list and number of transplants. Figure courtesy: [6].....	7
Figure 2.2	Worldwide tissue engineering, cell therapy and transplantation market. Size and growth by region, 2009. Figure courtesy: [7].....	8
Figure 2.3	Demonstration of photomask technique to create micropatterned structures. A) Prepolymer is loaded into a container of specified dimensions with a transparent top surface containing the photomask. UV light passing through the photomask to the photosensitive prepolymer causes polymerization only in the regions where UV light is able to pass through. B) Subsequent UV light application enables layer-by-layer fabrication of 3D structures. C) Functional 3D hepatic tissue created using this technique. Figure courtesy: [9]	12
Figure 2.4	Hyaluronic acid (HA) micromolding process with Poly(dimethylsiloxane) (PDMS) structures as molds. A) without cells B) with cells. Figure courtesy: [10]	13
Figure 2.5	Schematic of stereolithography system for tissue engineering applications. A) Top-down approach where the platform is moved downwards after each layer of prepolymer is photopolymerized, B) Bottom-top approach where the prepolymer is pipetted one layer at a time, C) Digital micromirror arrangement for microstereolithography. Figure courtesy: [12]	14
Figure 2.6	SEM images of scaffold with controlled microporosity. A) Tropoelastin/elastin composite fabricated by using dense gas CO ₂ , B) the	

composite supported human skin fibroblast growth and migration. C) PCL/elastin scaffold produced by gas foaming/salt leaching process, D) the fabricated scaffold promoted primary articular cartilage chondrocyte adhesion and proliferation. Figure courtesy: [31]	16
Figure 2.7 Schematic of micro punch process. Figure courtesy: [42]	18
Figure 2.8 Vision system for die alignment during micropunching. Figure courtesy: [42]	19
Figure 2.9 Schematic of flexible punching process. Figure courtesy: [44].....	20
Figure 2.10 Forming and punching process with modified blanking die. (a) Initial state, (b) forming stage, (c) punching stage, (d) opening stage. Figure courtesy: [49].....	22
Figure 2.11 Schematic of setup for micro-punching process based on spallation delamination induced by laser driven flyer. Figure courtesy: [50].....	22
Figure 2.12 Ultimate Tensile Strength with respect to length scale. Figure courtesy: [51]	23
Figure 2.13 Effects of relative blanking clearance on maximum blanking force and ultimate shearing strength. (a) $t = 100 \mu\text{m}$ and (b) $t = 200 \mu\text{m}$. Figure courtesy: [52].....	24
Figure 2.14 Effects of the ratio of blanking clearance to grain size on ultimate shearing strength. Figure courtesy: [52]	24
Figure 2.15 Size effect model of grain size in micro-punching 1-micropunch; 2-microdie; 3-metal foil. (a) $c/d > 1$; (b) $c/d = 1$ and (c) $c/d < 1$. Figure courtesy: [52]	25
Figure 2.16 Comparison between experimental and simulated extruded micropins. Figure courtesy: [74].....	33
Figure 2.17 Different specimen geometries and their relative orientations with respect to load direction. Figure courtesy: [21]	34

Figure 2.18 Experimental results from tensile test of different PCL scaffold specimens. Figure courtesy: [21]	35
Figure 2.19 FEA simulation results for material properties of PCL scaffold specimens. Figure courtesy: [21]	36
Figure 2.20 Stress-strain curve of PCL at various strain rates and temperatures. Figure courtesy: [85].....	37
Figure 2.21 Experimental stress-strain data of PCL at various strain rates and temperatures. Figure courtesy: [85].....	37
Figure 3.1 Micropunching setup (a) microscope, (b) female die holder (c) vacuum pad, (d) male die holder, (e) spherical bearing, (f) dynamometer, (g) X, Y, Z and θ stage.....	41
Figure 3.2 Boundary conditions for a quarter model considered for all simulations to predict peak punching force	44
Figure 3.3 FE model of the micropunching process	48
Figure 3.4 Comparison of maximum punching force for each die clearance (mean +/- SD).	49
Figure 3.5 SEM images of a burr ring (arrow) surrounding the exit side of the micro- punched holes. Die clearance: (a) 7.6 %, (b) 18.6 %, (c) 24.0 % and (d) 48.0 %.....	50
Figure 3.6 Comparison stress distribution contours for clearances (a) 7.6 %, (b) 18.6 %, (c) 24.0 % and (d) 48.0 %	51
Figure 3.7 Comparison of strain distribution contours for clearances (a) 7.6 %, (b) 18.6 %, (c) 24.0 % and (d) 48.0 %	51
Figure 3.8 Comparison of simulation and experimental results (mean +/- SD) for maximum punching force.....	52

Figure 3.9 Correlation between die clearance and the outside diameter of the burr ring formed on the exit side of the micropunched holes.....	55
Figure 4.1 Schematic of a punching process using a single slanted punch.....	58
Figure 4.2 Schematic of three different stages of punch stroke.....	60
Figure 4.3 Schematic of shear area for Stage I stroke length.....	61
Figure 4.4 Top view for Stage I.....	62
Figure 4.5 Front projection view of Stage II shear area.....	66
Figure 4.6 Isometric projection of Stage II shear area at three different time steps	66
Figure 4.7 Parallelogram shaped shear area on the cylindrical surface of the punched hole.....	67
Figure 4.8 Top projection view of Stage II shear area.....	68
Figure 4.9 Three stages of punching with a wedge shaped punch.....	71
Figure 4.10 Comparison of the analytical (dashed line) and simulated (solid line) nondimensionalized punching force profile for a 0 degree single slant angle	74
Figure 4.11 Comparison of the analytical (dashed line) and simulated (solid line) nondimensionalized punching force profile for a 10 degree single slant angle	75
Figure 4.12 Comparison of the analytical (dashed line) and simulated (solid line) nondimensionalized punching force profile for a 20 degree single slant angle	75
Figure 4.13 Comparison of the analytical (dashed line) and simulated (solid line) nondimensionalized punching force profile for a single 30 degree slant angle	76

Figure 4.14 Comparison of the analytical (dashed line) and simulated (solid line) nondimensionalized punching force profile for a single 45 degree slant angle	76
Figure 4.15 Comparison between nondimensional peak punching force (FE simulation – solid line) and nondimensional peak shear area rate (analytical model – dashed line) for each of the five single slant angles (0, 10, 20, 30, and 45 degrees)	77
Figure 5.1 Ring opening polymerization for Polycaprolactone. Figure courtesy: [94] .	78
Figure 5.2 PCL punching at room temperature resulting in a bag like structure	80
Figure 5.3 CAD model of the injection mold used to fabricate a PCL test specimen for compression testing	82
Figure 5.4 Midsection view of the injection mold used to fabricate PCL specimens for compression testing	83
Figure 5.5 CAD model of the compression test fixture showing the liquid nitrogen reservoir.....	84
Figure 5.6 Cross sectional view of the compression test setup.....	85
Figure 5.7 Typical stress-strain curve for a rigid plastic. Figure courtesy: [97]	90
Figure 5.8 Engineering stress-strain curve for PCL compression testing at room temperature	92
Figure 5.9 Raw engineering stress-strain curve for a typical PCL specimen tested in compression at room temperature	93
Figure 5.10 Linear region of the raw engineering stress-strain curve for a typical PCL specimen tested in compression at room temperature	93
Figure 5.11 Zero corrected engineering stress-strain curve for a typical PCL specimen tested in compression at room temperature	94

Figure 5.12 0.2 % offset Yield strength from the zero corrected engineering stress - strain data of a typical PCL specimen tested in compression at room temperature	95
Figure 5.13 Engineering stress – strain curve of PCL samples submerged in liquid nitrogen during compression testing (aspect ratio = 1.5)	95
Figure 5.14 Experimental results and related Ludwik’s equation for PCL flow stress. Data from compression testing while the specimen is submerged in liquid nitrogen (aspect ratio = 1.5).	97
Figure 5.15 Engineering stress – strain curve of PCL in liquid nitrogen is given in Fig. 12 for specimen aspect ratio l/d equal to 1	97
Figure 5.16 Flow stress of PCL in liquid nitrogen from Ludwik's equation for specimens of aspect ratio of l/d equal to 1	98
Figure 5.17 Experimentally determined flow stress curves for PCL (reciprocal aspect ratios equal to 1.0 and 2/3). The experimental data was extrapolated to generate a flow stress curve for PCL in compression (dashed line) for $d/l = 0$.	100
Figure 5.18 Extrapolation of Strength Coefficient to $d/l = 0$	102
Figure 5.19 Flow Stress for three different values of the Strength Coefficient	102
Figure 6.1 DSM Xplore Micro 15 cc twin screw micro-compounder. Figure courtesy: [4]	106
Figure 6.2 Female die assembly with liquid nitrogen reservoir	107
Figure 6.3 Male die block assembly with liquid nitrogen reservoir	108
Figure 6.4 Exploded view of the female die cooling system	109
Figure 6.5 Material holder with XYZ translation staging	110
Figure 6.6 SEM image of a gage pin used as a punch.	111
Figure 6.7 SEM image of a slanted punch face	112
Figure 6.8 SEM image of sheared facet at the end of a punch face	112

Figure 6.9 SEM image of the entry side of a laser cut stainless steel female die (210 μm hole diameter, 150 μm thick stainless steel).....	113
Figure 6.10 SEM image of the exit side of a laser cut stainless steel female die. The arrow shows a small step along the perimeter of the hole. The step is an artifact from the laser cutting process.	114
Figure 6.11 FEA model of fully aligned die sets during cryogenic micropunching of PCL. Symmetry permits a quarter model. The mesh is refined in the shear zone (arrow).....	116
Figure 6.12 Peak punching force as a function of die clearance for 70 μm thick PCL film	122
Figure 6.13 Peak punching force as a function of die clearance for 40 μm thick PCL film	123
Figure 6.14 SEM image of a micro hole punched with 8.6 % die clearance (70 μm thick PCL film).....	124
Figure 6.15 SEM image of a micro hole punched with 17.1 % die clearance (70 μm thick PCL film).....	124
Figure 6.16 SEM image of an incomplete micro hole punched with 25.7 % die clearance (70 μm thick PCL film)	125
Figure 6.17 Effective stress distribution plot at 30 μm punch stroke for 8.6% die clearance in 70 μm thick PCL film.....	126
Figure 6.18 Effective stress distribution plot at 30 μm punch stroke for 17.1% die clearance in 70 μm thick PCL film.....	127
Figure 6.19 Effective stress distribution plot at 30 μm punch stroke for 25.7% die clearance in 70 μm thick PCL film.....	127
Figure 6.20 Effective strain distribution plot at 30 μm punch stroke for 8.6% die clearance in 70 μm thick PCL film.....	128

Figure 6.21 Effective strain distribution plot at 30 μm punch stroke for 17.1% die clearance in 70 μm thick PCL film.....	129
Figure 6.22 Effective strain distribution plot at 30 μm punch stroke for 25.7% die clearance in 70 μm thick PCL film.....	129
Figure 6.23 Effective stress distribution plot at 15 μm punch stroke for 15% die clearance in 40 μm thick PCL film.....	130
Figure 6.24 Effective stress distribution plot at 15 μm punch stroke for 30% die clearance in 40 μm thick PCL film.....	130
Figure 6.25 Effective stress distribution plot at 15 μm punch stroke for 45 % die clearance in 40 μm thick PCL film.....	131
Figure 6.26 Effective strain distribution plot at 15 μm punch stroke for 15 % die clearance in 40 μm thick PCL film.....	131
Figure 6.27 Effective strain distribution plot at 15 μm punch stroke for 30 % die clearance in 40 μm thick PCL film.....	132
Figure 6.28 Effective strain distribution plot at 15 μm punch stroke for 45 % die clearance in 40 μm thick PCL film.....	132
Figure 6.29 Finite element model for simulating misaligned micropunching.	133
Figure 6.30 Non-symmetric opening of micro hole due to misaligned punching.....	133
Figure 6.31 Stress (MPa) distribution plot for misaligned punch at punch strokes of a) 10 μm , b) 20 μm , c) 30 μm , d) 40 μm , e) 50 μm , and f) 60 μm	134
Figure 6.32 train distribution plot for misaligned punch at punch strokes of a) 10 μm , b) 20 μm , c) 30 μm , d) 40 μm , e) 50 μm , and f) 60 μm	135
Figure 6.33 Comparison of measured and simulated peak punching force for film thickness of 40 μm	136
Figure 6.34 Comparison of measured and simulated peak punching force for film thickness of 70 μm	137

Figure 7.1	A membrane with holes arranged in a squared pattern. The minimum web thickness is defined by f	142
Figure 7.2	Finite element model used to simulate micropunching a 200 μm hole adjacent to a pre-existing hole (70 μm thick PCL).....	145
Figure 7.3	Test case for 8.6% die clearance showing a linear pattern of micropunched holes to observe web tearing as the holes are punched progressively closer together (200 μm punch, 70 μm thick PCL).....	146
Figure 7.4	Test case for 17.1% die clearance showing a linear pattern of micropunched holes to observe web tearing as the holes are punched progressively closer together (200 μm punch, 70 μm thick PCL).....	146
Figure 7.5	Test case for 25.7% die clearance showing a linear pattern of micropunched holes to observe web tearing as the holes are punched progressively closer together. Partial shearing was observed, with a geometric consistency indicative of die misalignment (200 μm punch, 70 μm thick PCL).	147
Figure 7.6	Partially fractured, but unbroken web for 8.6% die clearance and a center-to-center hole distance of 230 μm resulting in a nominally 30 μm thick web (70 μm thick PCL)	148
Figure 7.7	Unbroken web for 17.1% die clearance and a center-to-center hole distance of 230 μm resulting in a nominally 30 μm thick web (70 μm thick PCL) ..	148
Figure 7.8	Broken web for 8.6% die clearance and a punch center-to-center distance of 220 μm resulting in a nominal 20 μm thick web (70 μm thick PCL).....	149
Figure 7.9	Broken web for 17.1% die clearance and a punch center-to-center distance of 220 μm resulting in a nominal 20 μm thick web (70 μm thick PCL).....	149
Figure 7.10	Fractured web for punch center-to-center distance of 210 μm , resulting in a nominal web thickness of 10 μm (8.6% die clearance, 70 μm thick PCL) .	150

Figure 7.11 Fractured web for punch center-to-center distance of 200 μm , resulting in a line-on-line condition between adjacent holes (8.6% die clearance, 70 μm thick PCL)	151
Figure 7.12 Fractured web for punch center-to-center distance of 190 μm , resulting in 10 μm overlap along the center line between adjacent holes (8.6% die clearance, 70 μm thick PCL)	151
Figure 7.13 Fractured web for punch center-to-center distance of 210 μm , resulting in a nominal web thickness of 10 μm (17.1% die clearance, 70 μm thick PCL)	152
Figure 7.14 Fractured web for punch center-to-center distance of 200 μm , resulting in a line-on-line condition between adjacent holes (17.1% die clearance, 70 μm thick PCL)	152
Figure 7.15 Fractured web for punch center-to-center distance of 190 μm , resulting in 10 μm overlap along the center line between adjacent holes (17.1% die clearance, 70 μm thick PCL)	153
Figure 7.16 Model geometry for the finite element simulation of micropunching a hole adjacent to a preexisting hole	155
Figure 7.17 Comparison of (a) simulated geometry from FE model and (b) SEM image from experiment for adjacent micro-hole punching at a center-to-center distance of 210 μm with a die clearance of 8.6 % (nominal 10 μm web thickness, 70 μm thick PCL)	156
Figure 7.18 Comparison of (a) simulated geometry from FE model and (b) SEM image from experiment for adjacent micro-hole punching at a center-to-center distance of 200 μm (line-on-line condition) with a die clearance of 8.6% (70 μm thick PCL)	156

Figure 7.19 Stress (MPa) distribution plot of the cross section during adjacent punching at center to center distance of 210 μm with die clearance of 8.6 % at punch stroke length of 30 μm	157
Figure 7.20 Stress distribution plot of the cross section during adjacent punching at center to center distance of 210 μm with die clearance of 8.6 % at punch stroke length of 40 μm	158
Figure 7.21 Comparison of (a) simulated geometry from FE model and (b) SEM image from experiment for adjacent micro-hole punching at a center-to-center distance of 230 μm (30 μm nominal web thickness) with a die clearance of 17.1% (70 μm thick PCL)	159
Figure 7.22 Comparison of (a) simulated geometry from FE model and (b) SEM image from experiment for adjacent micro-hole punching at a center-to-center distance of 210 μm (10 μm nominal web thickness) with a die clearance of 17.1% (70 μm thick PCL)	159
Figure 7.23 Stress (MPa) distribution plot of the web during adjacent punching at a center-to-center distance of 222 μm with die clearance of 17.1 % at punch stroke length of 31.5 μm	160
Figure 7.24 Hexagonally-Close-Packed arrangements of holes	161

Chapter 1

Introduction

1.1. Problem Statement

Development of tissues and organs from synthetic and natural scaffolds has been a persistent goal of research in the field of tissue engineering. The need for such research is pressing given that on average 18 people die every day as they wait for an organ transplant according to a recent study by the U.S. Department of Health and Human Services [1]. Presently, research in the field of tissue engineering has focused mainly on small scale development of tissue samples for testing and analysis, rather than on mass production technologies. However, as the market for tissue engineering and regenerative medicine increases, scaling-up laboratory prototyping methods to create efficient mass production processes will become paramount to delivering a cost effective solution.

A synthetic 3D engineered microarchitecture that is suitable for a cell scaffold is of interest to many researchers. Ideally, the microarchitecture has sufficient home sites for seeding of progenitor cells and adequate vascularity to facilitate transport of oxygen and nutrients, as well as to facilitate waste removal as the cells grow. The goal of a well designed synthetic scaffold is to have microfluidic channels that mimic natural tissue vascularity [2]. In general, microvascular structures are necessary for mass transport across length scales of approximately 200 μm to promote healthy cell growth [3].

Conventional scaffold development methods, such as solvent-casting with particulate leaching, gas foaming, phase separation, melt molding, freeze drying, and solution casting are not suitable for engineering a vascularized scaffold, due to their inability to produce a microarchitecture where pore size and arrangement are specified, as opposed to randomly distributed, in cases where microfluidic vasculature are needed.

Solid freeform fabrication methods (additive manufacturing) like 3D printing, stereolithography, fused deposition modeling, and phase-change jet printing can be used to fabricate engineered porous microstructures. However, most of these methods require an internal support structure, which needs to be dissolved at the end of the fabrication process. Residuals from the solvent process can be potentially toxic to the seeded cells. In addition, these methods are primarily intended for rapid prototyping and not for high volume industrialized manufacturing, where the demands for production efficiency are much greater.

A relatively new approach to fabricating synthetic 3D tissue scaffolds with engineered microporosity is multilayer stacking of 2D porous polymeric membranes. This is an attractive alternative to free form methods due to the potential for high throughput manufacturing without the use of solvents. In the current research, the 2D layers are created by rapidly punching micro-scale holes and patterns of holes in thin (25-70 μm) polymer films that can be mass produced by hot melt extrusion. Recently, a new micropunching machine and cryogenic process have been developed at Tufts University to manufacture 2D porous membranes with a specific pore size, geometry, and location [4]. The next step in the manufacturing process, which is outside the scope of this thesis, is to properly align, stack, and bond the individual 2D membranes to create a 3D tissue engineering construct with holes for cell seeding and with micro-tubules to simulate tissue vascularity.

1.2. Purpose of the Study

The aim of this research is to investigate the application of finite element analysis (FEA) to simulate the micropunching process and to predict cryogenic punching forces in Polycaprolactone (PCL), a biocompatible, biodegradable polymeric membrane. If the finite element method proves suitable, as verified by micropunching experiments, it will be a powerful numerical tool that can be used by engineers to optimally design robust die sets and related equipment for industrialization of the micropunching process. The research also focuses on analyzing maximum achievable porosity within a single polymeric membrane, the effect of die clearance on peak punching force, and the effect of processing parameters on hole quality.

It is desirable to have a high level of porosity to maximize the volume of seeded cells, while minimizing the degree of biodegradation necessary for resorption of the sacrificial scaffold. Finally, some aspects of punch geometry e.g. slanted punch face are investigated through the development of analytical and numerical models in an effort to design a punch that requires less force to produce a hole, thereby increasing die life and reducing energy consumption.

1.3. Research Objectives

- i. Characterize the uniaxial compression true stress-strain behavior (constitutive relationship) of Polycaprolactone (PCL) when cooled below the glass transition temperature;
- ii. Conduct research into validating a finite element model of the micropunching process through experiments with PCL membranes to predict final hole geometry, peak punching force, and minimum web thickness between adjacent holes;

- iii. Determine the relationship between punch clearance and maximum achievable porosity when creating thin webs between a line of adjacent holes in PCL membranes;
- iv. Characterize the relationship between punch clearance and peak stamping force to determine if there is an optimum clearance when creating microscale holes in PCL membranes;
- v. Study the effect of punch geometry on the punching force profile when the top surface of the punch is either parallel or skew to the surface of the workpiece, with the skewed surface causing a “can opener” effect when micropunching; and
- vi. Assess the predictive capability of a finite element model when micropunching copper foil where the grain size is comparable to material thickness and hole size.

1.4. Hypothesis

The finite element method can be used to accurately predict the effect of die clearance on punching force and on web tearing during cryogenic microscale hole punching of a polymer membrane.

1.5. Punching Process Terminology

Micropunching is a relatively new technology. However, macro-punching is a well understood, developed, and extensively used forming process. The basic steps and methods in a micropunching process are no different than the punching process at a macro scale. Therefore, details of a typical punching process are presented here. As shown in Figure 1.1, a typical macro-scale punching setup has four major components.

- i. Male Die or Punch
- ii. Female Die or Die Plate
- iii. Guide Plate or Stripper Plate
- iv. Workpiece

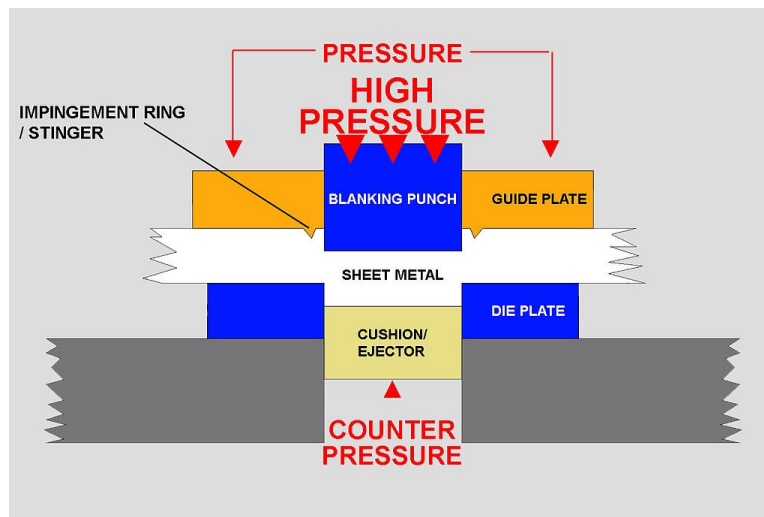


Figure 1.1 Schematic of a typical punching or blanking process [5]

The male die (punch) exerts a force on the workpiece, where a shearing process facilitates punching a hole or blanking an edge. When creating a circular hole, the diameter of the punch is typically the same size as the desired hole in the workpiece. However, the hole in the female die is slightly larger than the male punch, creating a clearance between the dies.

In general, the female die is fixed in place as the male die translates perpendicular to the workpiece surface. Often, a guide plate (stripper plate) secures the workpiece while the male die creates the desired hole geometry. In some cases, as shown in the schematic of Figure 1.1, the guide plate has an impingement ring to further constrain material flow near the male die i.e. fine blanking. Also, a cushion or ejector can be used to support and remove the punched or blanked part.

In the case of a sheet metal workpiece, the wall geometry of the sheared hole has some typical features as shown in Figure 1.2.

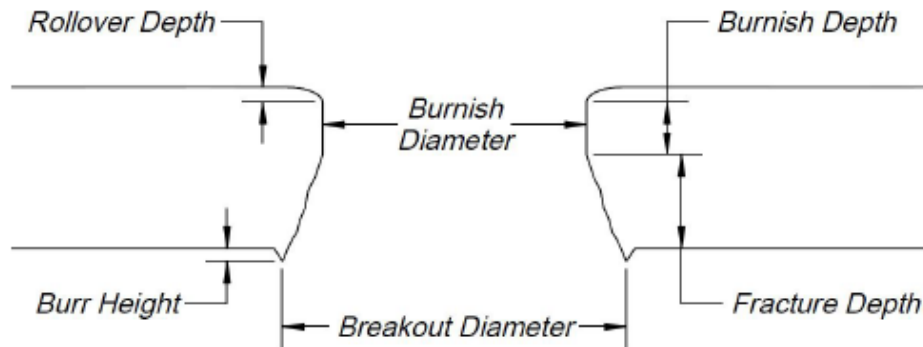


Figure 1.2 Typical punched hole profile. Figure courtesy: [4]

There are four visible attributes to the sheared sidewall in metal punching: (1) rollover depth, (2) sheared or burnish depth, (3) fracture depth, and (4) burr height. The distribution of these four zones across the thickness of the punched wall indicates the quality of the punching process i.e. burnish and breakout diameter. The effect of process parameters, such as die clearance, edge radius, and workpiece ductility on the relative distribution of these geometric zones have been studied extensively and are discussed in Chapter 2.

Chapter 2

Background – Survey of Literature

2.1. Tissue Engineering

Currently in the United States, the number of men, women, and children in need of life saving organ transplants is 115,000 [1], which is more than enough to fill a large football stadium. One name is added to the waiting list every 10 minutes and, unfortunately, the gap between the number of patients on the waiting list and the number of donors continues to widen, Figure 2.1.

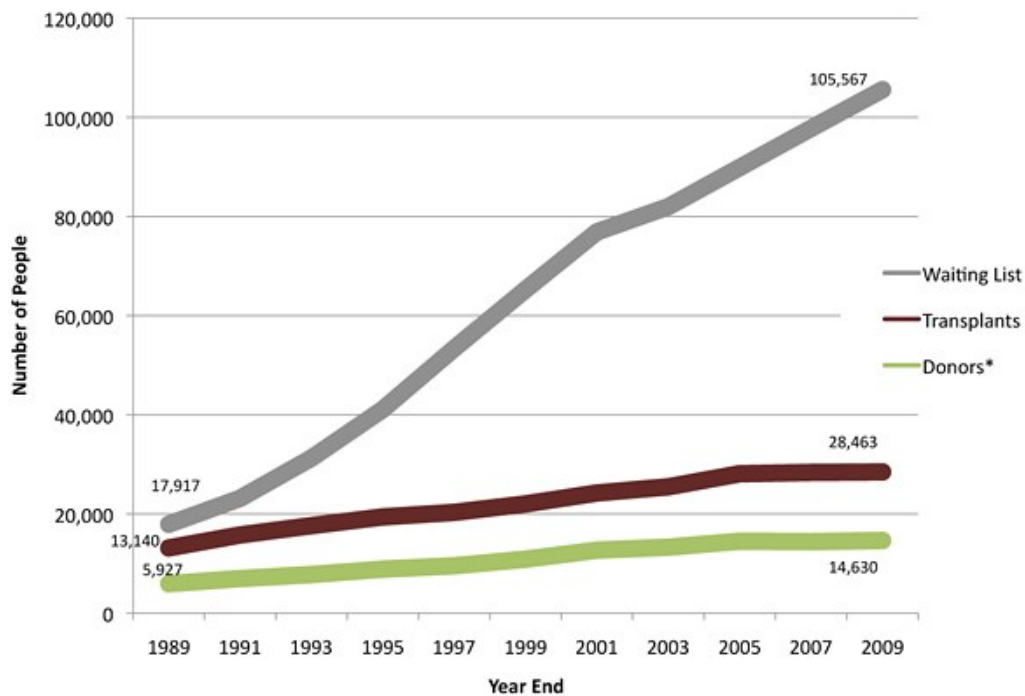


Figure 2.1 Continuous widening of the gap between number of patients in waiting list and number of transplants. Figure courtesy: [6].

To meet this growing demand for tissues and organs, the market for artificial tissue is growing exponentially. Tissue engineering and regenerative medicine in the United States was a \$6.9 billion market in the year 2009, but it is expected to grow to about \$32 billion by the year 2018 [7]. This market is growing in all regions of the world, but particularly in the United States, Figure 2.2. Therefore, research to develop different methods to create artificial tissues and organs is of paramount importance to improve the livelihood of patients and in some cases to save their lives. New manufacturing methods, particularly those with high production rates and economical cost, are of particular interest to the tissue engineering industry.

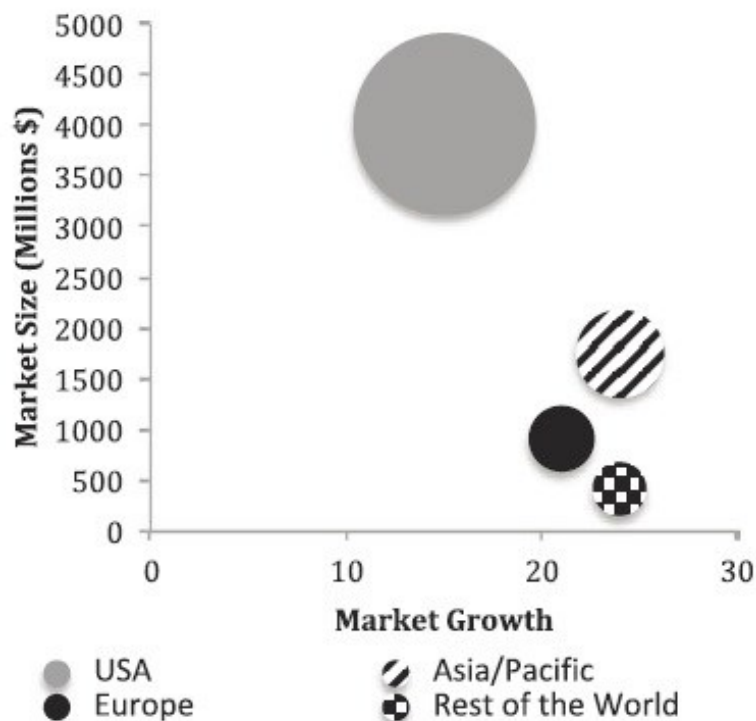


Figure 2.2 Worldwide tissue engineering, cell therapy and transplantation market. Size and growth by region, 2009. Figure courtesy: [7]

Multilayer stacking presents a significant manufacturing challenge. Clinically relevant treatments for hundreds of thousands to millions of patients annually requiring various tissue implants will require the fabrication of hundreds of billions to trillions of holes per year. Consider just the example of tissue implants for knee cartilage repair as a substitute for using total knee arthroplasty (TKA), in which metal implants are used to completely replace the mating ends of the tibia and femur. Cartilage tissue implants (CTIs) could provide a much less traumatic and much less expensive alternative to TKA. They also could be administered much earlier in the progression of cartilage degradation, with consequent improvements in mobility, reduction of lost wages, and/or need for care. With the aging of the US population, the number of candidates for this procedure is estimated to grow to 3.48 million in 2030 [8]. Table 2.1 shows that servicing just 10% of this population with CTIs instead would require fabricating on the order of 50 billion microscale holes.

Table 2.1 Example calculation of holes required to create a cartilage tissue implant by multilayer stacking

Category	Quantity
(A) 10% of estimated annual number of candidates for total knee arthroplasty in 2030	350 Thousand
(B) Number of cartilage tissue implants per patient (medial and lateral condyle)	2
(C) Area of single implants	1 cm ²
(D) Number of 50 μm thick membrane layers for a single 0.5 mm thick implant	10
(E) Number of holes per cm ² (60% porosity and 100 μm average hole diameter)	7600
Total number of holes required per year (product of A through E)	53 billion

Biologists currently use rapid prototyping methods to create holes in single polymer layers for laboratory testing. Unfortunately, these methods are likely not going to scale economically to meet the clinical need. Laser ablation uses raster scanning and thus is a sequential process. It is difficult to imagine that it could create the huge number of holes required. Micro molding is a parallel process, but suffers from the difficulty of separating the thin membranes from the mold. Tearing of the web between holes occurs if the webs are too thin, and thus it is unclear if the porosities required for tissue engineering applications can be achieved. However, as shown in Table 2.2, only ten micropunching machines developed in the current research, each operating 3000 hours per year, could produce all of the holes required for the cartilage repair example.

Table 2.2 Manufacturing capacity (holes per year) of one cryogenic micropunching machine

Category	Quantity
(A) Number of compound die sets in a progressive die	10
(B) Number of punches per compound die set	100
(C) Strokes per hour (30 per minute)	1800
(D) Hours of operation per year (2 shifts with 25% downtime for maintenance)	3000
Total number of holes per machine per year (product of A through D.)	5.4 billion

Most tissues are comprised of multiple types of cells that are well organized in the extra cellular matrix (ECM). The specific functions of a particular kind of tissue are determined by its microarchitecture i.e. extensive vascular networks. Artificially achieving such functionality requires extremely precise scaffold structures. Currently, available artificial tissues are limited to simple architecture and cellular organization. One such example is engineered cartilage tissue, which has limited need for vasculature as compared to cardiac tissue. Artificial tissues like the heart and liver, which need to be

metabolically active, are still in the development stage. Tissue engineers have been trying to develop more complex vascular networks *in vitro* (outside of the body under conditions that simulate the host environment). In order to enhance biomimicry, scaffolds with three dimensional features are essential where different types of cells can be seeded and also where ECM molecules can be spatially distributed [7].

Conventionally, several different techniques have been used by researchers to develop three dimensional engineered microarchitectures to be used as synthetic tissue scaffolds. One such method is photomask based direct polymerization. A photomask is a two dimensional pattern that will let light pass through it in some selected areas. The wavelength of light can be carefully chosen to initiate polymerization of a prepolymer compound layered below the mask. A sequence of such patterns can be used to make very complex features. A drawback of this method is that it can only create feature geometry along layer thickness i.e. it is a “line-of-sight” method in the direction of the projected light. Also, residues of the solvent for the prepolymer can be toxic in nature and can potentially hinder cell growth. This method is generally suitable for various hydrogels and polymers containing acrylate groups [7]. Figure 2.3 shows the schematic of the direct polymerization process for developing tissue scaffolds.

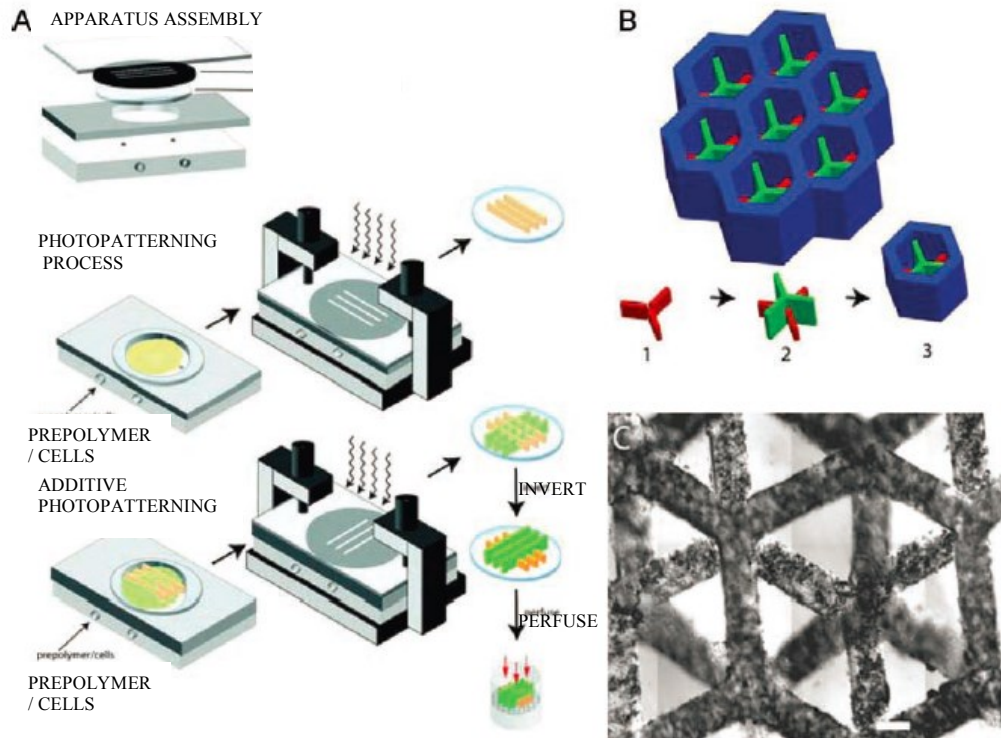


Figure 2.3 Demonstration of photomask technique to create micropatterned structures. A) Prepolymer is loaded into a container of specified dimensions with a transparent top surface containing the photomask. UV light passing through the photomask to the photosensitive prepolymer causes polymerization only in the regions where UV light is able to pass through. B) Subsequent UV light application enables layer-by-layer fabrication of 3D structures. C) Functional 3D hepatic tissue created using this technique. Figure courtesy: [9]

Another popular approach for making tissue scaffolds is micromolding. With this method, the substrate material is generally an elastomeric polymer which is molded with the help of ultraviolet light between a flat and a patterned die. This is one of the most widely used methods to produce features of many shapes and sizes ranging from 1 μm to 500 μm [11-13]. Drawbacks of this method include material hydrophobicity and swelling of the elastomeric molds. Figure 2.4 shows the schematic of the micromolding method.

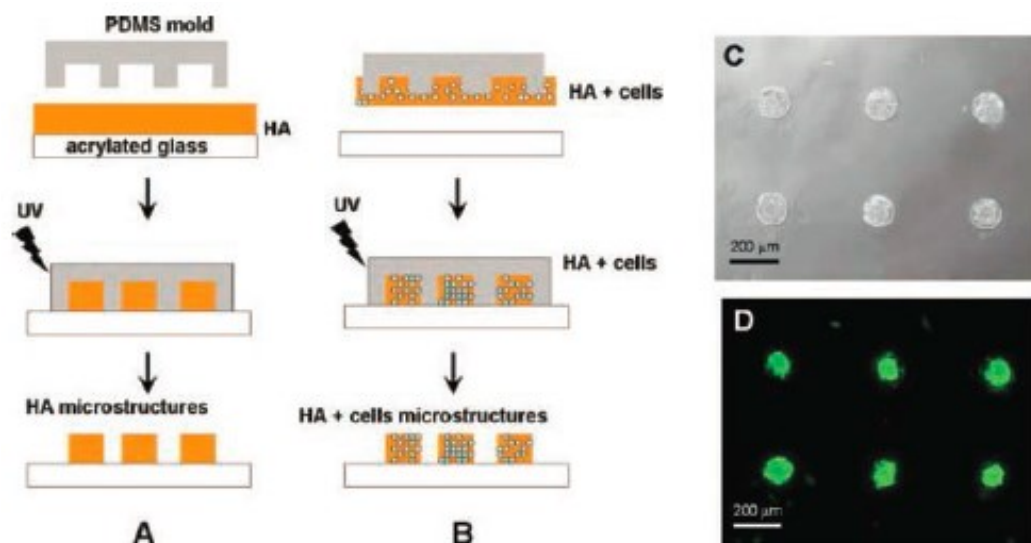


Figure 2.4 Hyaluronic acid (HA) micromolding process with Poly(dimethylsiloxane) (PDMS) structures as molds. A) without cells B) with cells. Figure courtesy: [10]

Tissue scaffolds can also be fabricated using several rapid prototyping techniques. Stereolithography (SLA) was first introduced by Charles W. Hull in 1986 (US Patent 4575330). In this method, the scaffolds are fabricated on a platform immersed in a tank of liquid polymer. The polymer is cured layer by layer with a laser. This method can have two different approaches: (1) “top-bottom” where all prepolymer is already in the tank and is cured layer by layer while lowering the platform after each layer is cured, and (2) “bottom-top” approach, where the prepolymer is pipetted into the container for each layer on top of the previous layer. An improved version of stereolithography to produce high resolution is called micro-stereolithography. Unlike conventional stereolithography where the complete layer is traced by the laser, in micro-stereolithography a dynamic mask is prepared for individual layers using an array of digitally controlled micro-mirrors. Features as small as 20 μm have been fabricated into a tissue scaffold by using this method [14-16]. The schematic of this method is shown in Figure 2.5.

Another rapid prototyping method is known as Melt Dissolution Deposition System. In this method, the prepolymer is either in powder form or in molten form. If it is in powder form, certain portions of a layer are heated carefully using a laser beam, which causes bonding of the heated particles. This method of melt dissolution is known as Selective Laser Sintering (SLS). This method has been used to create tissue scaffold from polycaprolactone (PCL) [17], a biodegradable material on which current research is focused. For bone tissue scaffolding, SLS has been used with several materials like ceramic [18, 19], polymers [20, 21] and composites [22-24].

In the case where the prepolymer is in a molten state, it is deposited from a very small extrusion tip layer by layer, solidifying quickly as it cools [25]. This melt dissolution method is called Fused Deposition Modeling (FDM). Complex three dimensional micro-features can be made using this technique. The disadvantage of FDM is its low resolution which limits the minimum size of features that can be incorporated into the scaffold.

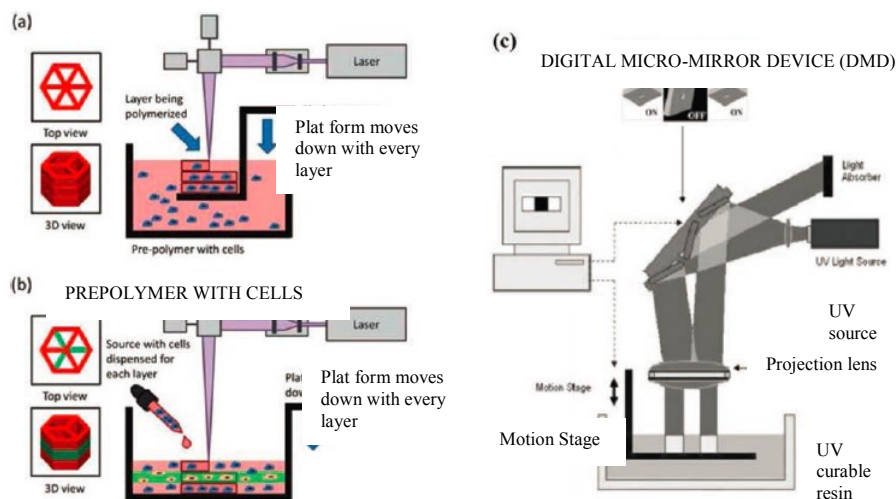


Figure 2.5 Schematic of stereolithography system for tissue engineering applications. A) Top-down approach where the platform is moved downwards after each layer of prepolymer is photopolymerized, B) Bottom-top approach where the prepolymer is pipetted one layer at a time, C) Digital micromirror arrangement for microstereolithography. Figure courtesy: [12]

As the name suggests, the methods discussed in the rapid prototyping approaches are suitable for prototyping, but are not intended for mass production. In general, laser rastering methods are likely too slow to be considered for mass manufacturing.

Gas foaming is another method to create tissue scaffolds from various polymeric materials. This method is used to fabricate controlled porous scaffolds of different pore sizes. In this method, an inert gas is mixed with molten prepolymer to create a two phase substance populated with bubbles of the inert gas. Once the polymer solidifies around the bubbles, the gas diffuses out gradually, leaving behind a highly porous structure to be used as a tissue scaffold. The typical inert gas used is CO₂, which is mixed with a continuous polymer phase under high pressure and the solution is saturated with CO₂ [26, 27]. The pore size is controlled by adjusting various process parameters like temperature, pressure, depressurizing rate, and relative concentration of various components. This method has been used successfully to make tissue scaffolds from different polymers like Polylactic Acid (PLA), Polylactic-*co*-glycolic Acid (PLGA) and Polycaprolactone (PCL) [26-29]. This method has also been used successfully to create composite scaffolds. Tropoelastin and elastin were mixed in pressurized CO₂ in an aqueous solution along with a cross linking agent. Highly cross linked and porous composite scaffolds were obtained, which were further shown to support human skin fibroblast growth and migration across the structure [30]. The SEM image of the resulting cross linked porous structure is shown in Figure 2.6. Unfortunately, this method does not support engineering a vascular network as the pores are random. Therefore, the cells tend to thrive on the surface of the scaffold, but perish within the center of thicker tissue constructs.

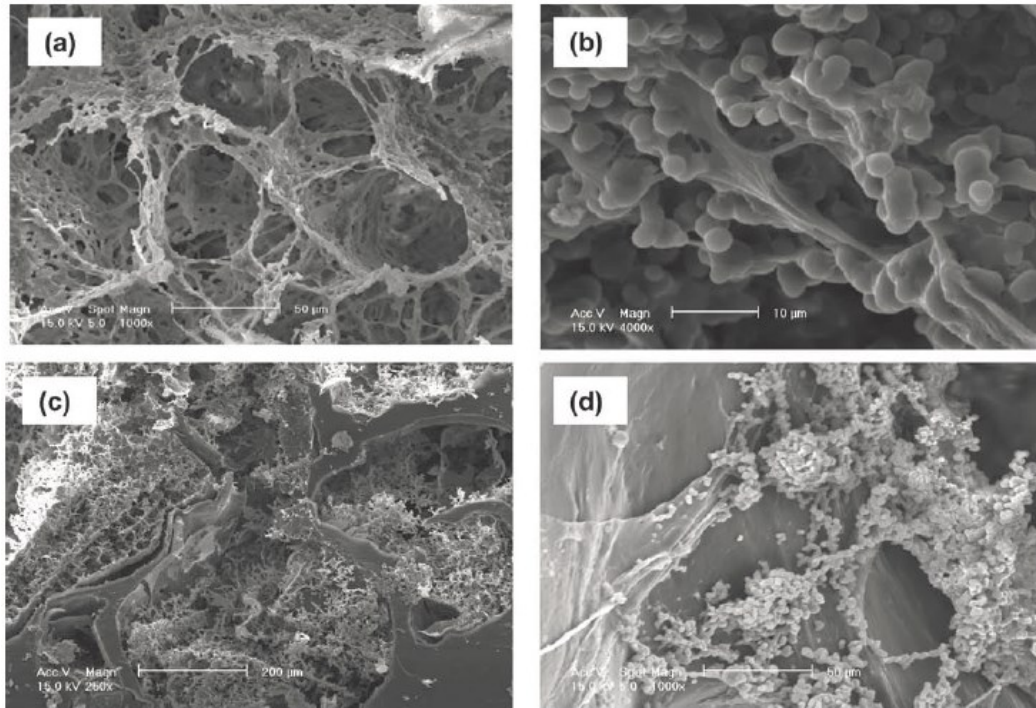


Figure 2.6 SEM images of scaffold with controlled microporosity. A) Tropoelastin/elastin composite fabricated by using dense gas CO₂, B) the composite supported human skin fibroblast growth and migration. C) PCL/elastin scaffold produced by gas foaming/salt leaching process, D) the fabricated scaffold promoted primary articular cartilage chondrocyte adhesion and proliferation. Figure courtesy: [31]

Another method to make scaffolds by controlling pore size is Porogen Leaching. In this method, various porogen particles are mixed with a molten polymer. Once the polymer solidifies, the porogen and polymer construct is immersed in a suitable solvent to dissolve and leach out the porogen particles. This leaves behind a highly porous polymeric scaffold [31]. Porogen materials like salt [29, 32-35], sugar [35], paraffin [36] and gelatin [37-39] have been proven successful in tissue engineering applications to develop various highly porous biomaterials. Different pore characteristics, such as pore size, porosity, and pore interconnectivity are controlled by the particle shape, size, and concentration [29, 35, 40, 41].

A combination of gas foaming and porogen leaching has been used to fabricate three dimensional porous structures from PCL by Salerno et al. [38]. The porogen material used was gelatin and the gas used for foaming was a mixture of CO₂ and N₂. After dissolving the porogens and diffusing the bubbles, the resulting microstructure had a pore size distribution in a bimodal fashion. It generated micro pores of average size 38 µm in diameter and macro pores of average size 312 µm in diameter. The resulting microstructure SEM images are shown in Figure 2.6.

It is only a matter of time before off-the-shelf artificial tissue will be available to be used by doctors for a wide spectrum of treatments. Patient specific artificial organs will no longer remain just an academic discussion. Ongoing trials and research will soon establish the feasibility of the extensive use of such artificial tissues and transplantable organs. Given the waitlist for transplantable organs and the growing demand of artificial tissue, the tissue engineering industry is most likely to fall short of adequate production to meet market demands unless it adopts more efficient ways to produce artificial tissues. The conventional methods such as direct polymerization, micro-molding, and rapid prototyping are not fast enough or economical enough to meet the market demand. Researchers need to focus their attention towards the production side of scaffold manufacturing. Presently, very little research has been done to address the issue of scaling-up rapid prototyping methods to meet a growing demand for engineered 3D scaffolds, where size, location, and interconnectivity of the porosity are controlled precisely by the designer.

2.2. Micropunching Machines and Dies

The first paper on micropunching was published by Joo et al. in 2001 [42]. In this early work, they demonstrated micro-punching by creating 100 µm diameter holes in 100

μm thick brass foil. Similar to a conventional punching process, they used a stripper plate to hold the workpiece, which was also used to align the male punch to the female die. The stripper plate and the female die were fabricated using a micro Electric Discharge Machining (micro EDM) process from tungsten carbide sheets of thickness 1 mm. The micropunch was fabricated from tungsten carbide by using a diamond grinding wheel. A schematic of this micropunching process is given in Figure 2.7, where t is the material thickness and c is the one sided die clearance.

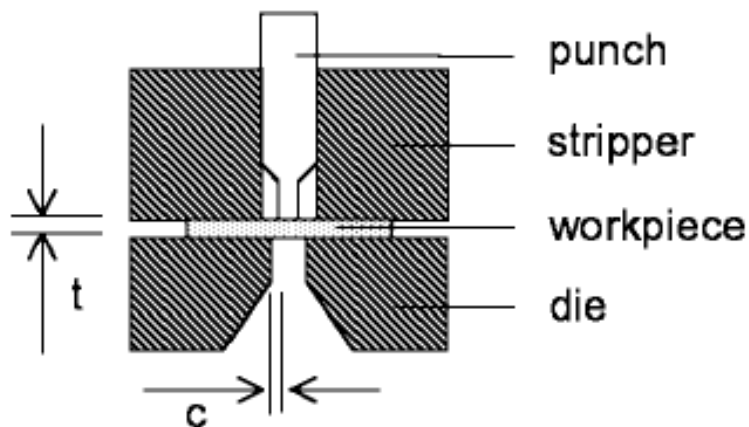


Figure 2.7 Schematic of micro punch process. Figure courtesy: [42]

In 2005, Joo et al. continued their research on micropunching, demonstrating the ability to punch holes of diameter $100\ \mu\text{m}$, $50\ \mu\text{m}$, and $25\ \mu\text{m}$ in thin brass and steel foils of thickness $100\ \mu\text{m}$, $50\ \mu\text{m}$, and $25\ \mu\text{m}$, respectively [43]. This time, however, a stripper plate was not used to guide the punch, but instead a linear guide system with high accuracy was used for alignment. In their publication, the difficulties of a micropunching setup were elucidated, particularly achieving the ultra high precision alignment between the male punch and the female die, where the die clearance is typically an order of

magnitude less than material thickness. To achieve precise alignment, they used an optical microscope and a beam splitter assembly to accurately align the punch with the center of the female die hole. A schematic of the vision system is shown in Figure 2.8.

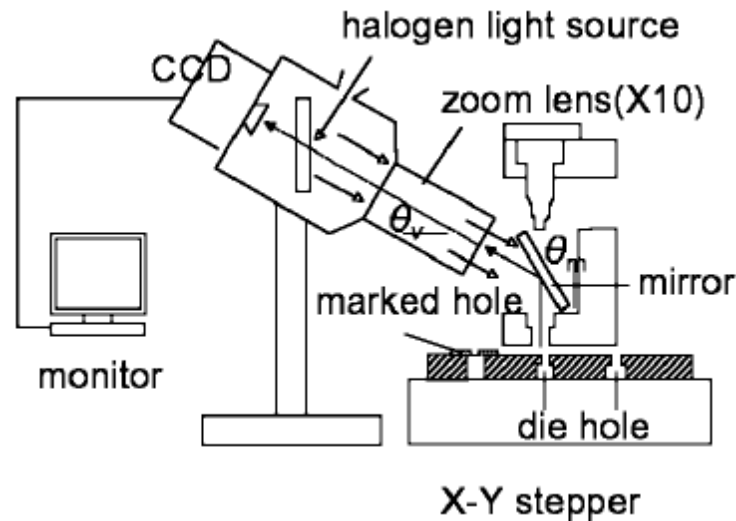


Figure 2.8 Vision system for die alignment during micropunching. Figure courtesy: [42]

In 2005, an innovative technique was demonstrated by Rhim et al. to overcome the alignment difficulties in micropunching [44]. They fabricated the female die using Deep Reactive Ion Etching (DRIE) from a single crystal (100) silicon wafer. There was no male die as such; instead, a flexible silicon polymer pad was used to punch an array of small holes simultaneously. Under high pressure of 1.1 - 1.8 GPa, the flexible pad deforms into the holes on the silicon wafer, punching holes in the mating workpiece, Figure 2.9. Holes with sizes varying from 2 μm to 10 μm in diameter were punched in copper sheets of thickness 3 μm and titanium sheets of thickness 1.5 μm . Unfortunately, there are two major drawbacks to their method. This method cannot be used for high production rates as the punch-out (the blank of material removed from the workpiece) must be etched away after each hole punching operation. Also, this method is only

suitable for very thin metal sheets as they require less shearing force for punching, which makes it less suitable for tissue engineering applications with polymers.

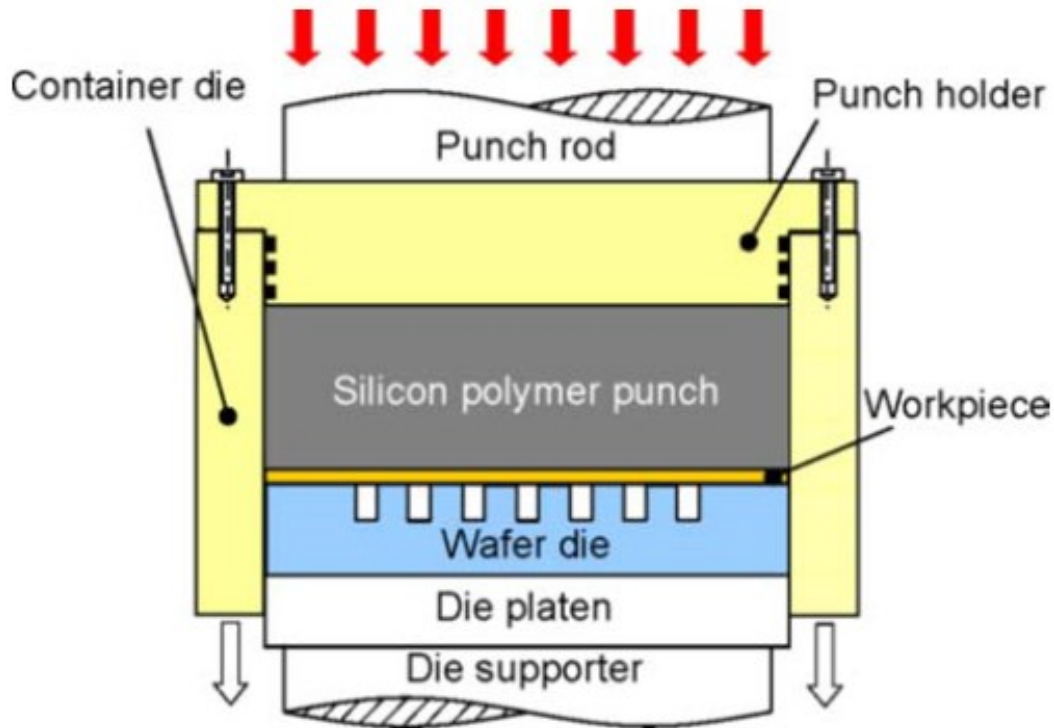


Figure 2.9 Schematic of flexible punching process. Figure courtesy: [44]

In 2006, Chern et al. published a paper on a new micropunching method based on Electric Discharge Machining (EDM) [45]. They fabricated the male punch from tungsten steel using a method called Wire Electro Discharge Grinding (WEDG). The male punch is then used as an electrode for making the female die through micro-EDM. Since both dies are fabricated on the same machine, they do not require further axial alignment, thus avoiding one of the major challenges of the micropunching process. In the same year, Chern and Chuang published another paper demonstrating the fabrication of noncircular punches using the WEDG method and also showed the feasibility of mass micro-punching by automating the micropunching setup [46]. In 2007, Chern et al.

demonstrated they could punch triangular and hexagonal holes in a 100 μm thick brass sheet [47]. The side length of the punched triangles and hexagons were 200 μm . The only drawback of Chern's method is that it would be difficult to accommodate both EDM micropunching of tissue scaffolds on the same machine as EDM will require a dielectric solution tank making the tissue material more exposed to potential contamination and toxicity.

In 2009, Xu et al. investigated the use of ion beam irradiation on the surface finish of micro punches [48]. In 2010, Kolleck et al. combined microforming and micropunching to fabricate micro holes with a raised edge in steel sheets [49]. Their method demonstrates the scope of work which can be accomplished by modifying process parameters, such as die geometry during micropunching. The schematic of the process is shown in Figure 2.10.

Di et al. validated a different approach for micropunching in thin metallic films, where in 2011 they used a laser driven flyer to induce spallation delamination [50]. This process uses the energy of a laser beam shock wave to induce micropunching of thin metallic foils. They could make fine microstructures in Gold films of thickness 50 nm, 100 nm, 200nm, and 500 nm coated on glass substrates and polyamide substrates. Their method is limited to very thin metallic foil which is not suitable for tissue engineering applications. A schematic of the process is shown in Figure 2.11.

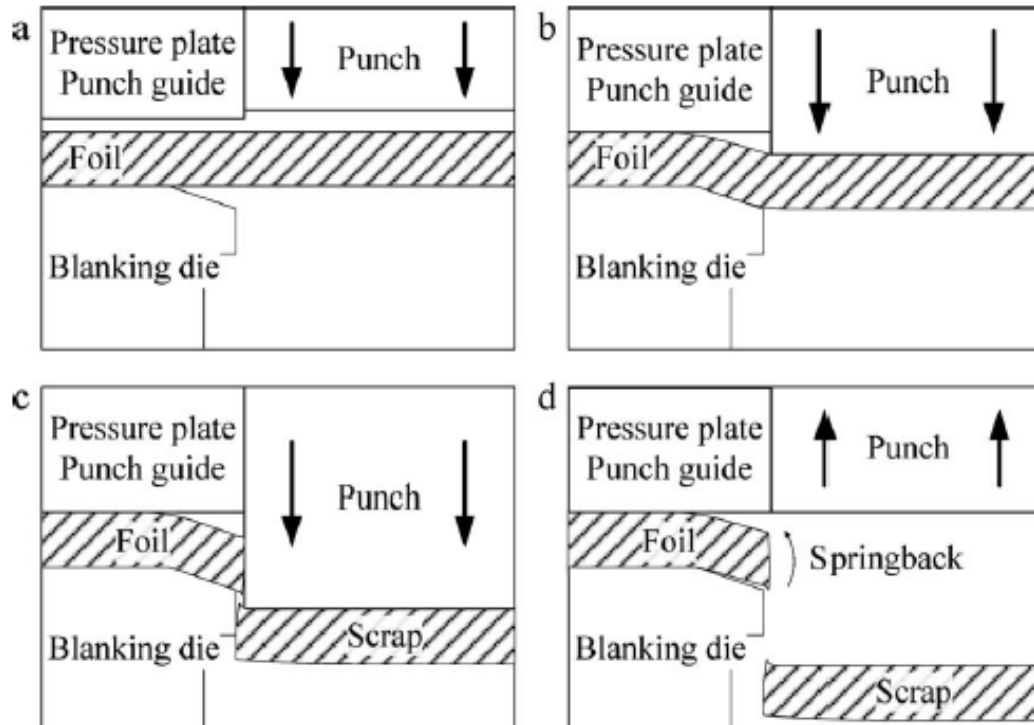


Figure 2.10 Forming and punching process with modified blanking die. (a) Initial state, (b) forming stage, (c) punching stage, (d) opening stage. Figure courtesy: [49]

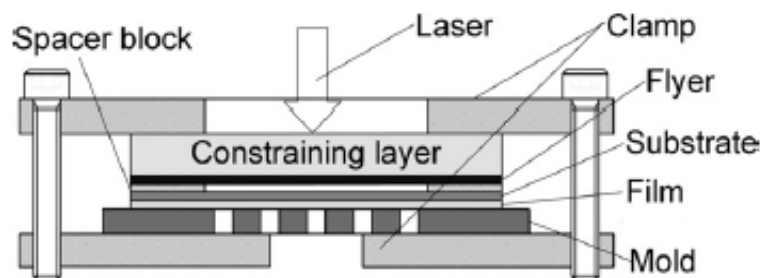


Figure 2.11 Schematic of setup for micro-punching process based on spallation delamination induced by laser driven flyer. Figure courtesy: [50]

In 2011, Xu et al. investigated the apparent variation in material strength during micropunching when length scales are reduced to the size of a single metallic grain, generating a so called “size effect” [51]. The size effect on the shear strength of brass

and steel foils was presented. Observations of an uneven distribution of the shear and fracture zone in the micropunched holes demonstrated material anisotropy. In addition, it was determined that shear strength of the brass and stainless steel foil increases as the length scale is decreased, Figure 2.12.

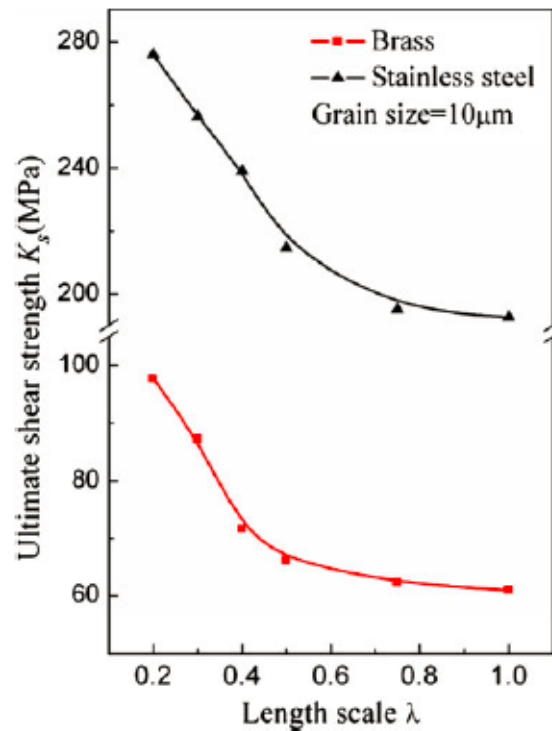


Figure 2.12 Ultimate Tensile Strength with respect to length scale. Figure courtesy: [51]

Xu et al. published an additional paper in April 2012 that demonstrated the size effect on the fracture mechanism during micropunching [52]. The combined effect of grain size, foil thickness, and blanking clearance was investigated. It was concluded that there exists a minima of the peak blanking force when the relative blanking clearance (ratio of single side die clearance to foil thickness) is changed, Figure 2.13.

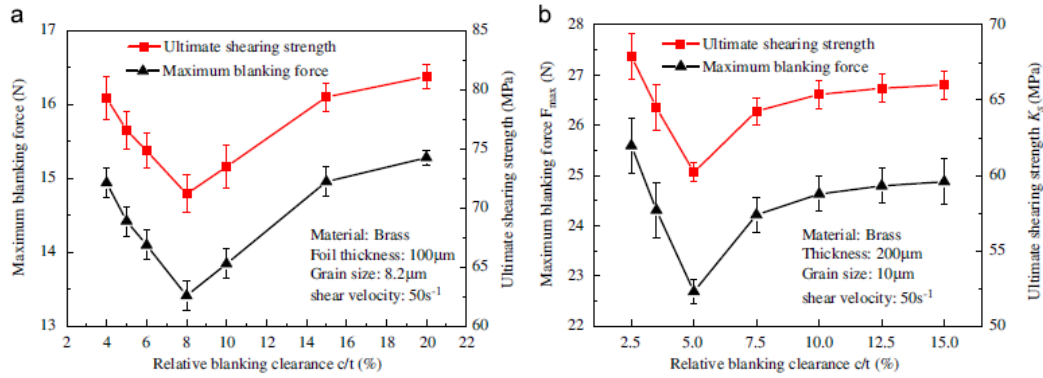


Figure 2.13 Effects of relative blanking clearance on maximum blanking force and ultimate shearing strength. (a) $t = 100 \mu\text{m}$ and (b) $t = 200 \mu\text{m}$. Figure courtesy: [52]

They also showed that the apparent ultimate shear strength is a minimum when the blanking clearance and grain size are equivalent, Figure 2.14. A schematic of the blanking process with different ratios of blanking clearance and grain size provides some insight into explain the size effect, Figure 2.15.

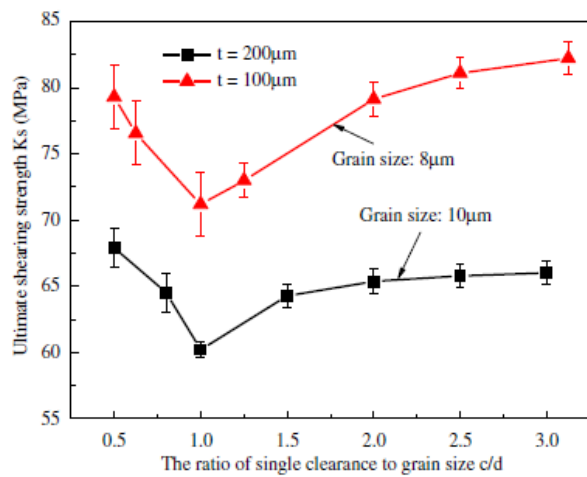


Figure 2.14 Effects of the ratio of blanking clearance to grain size on ultimate shearing strength. Figure courtesy: [52]

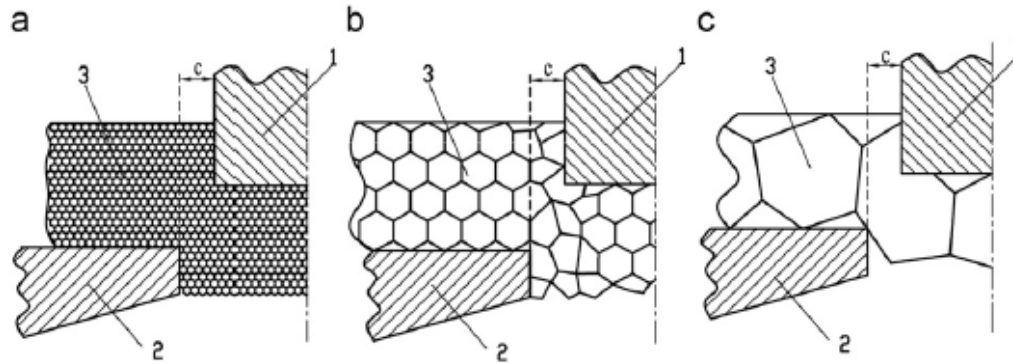


Figure 2.15 Size effect model of grain size in micro-punching 1-micropunch; 2-microdie; 3-metal foil. (a) $c/d > 1$; (b) $c/d = 1$ and (c) $c/d < 1$. Figure courtesy: [52]

Two months later, in June 2012, Xu et al. published a follow-on paper that focused on rapid production of a 200 hole micro array (50 x 4 holes, 600 μm diameter) [53]. This was accomplished by automating the brass foil feeding mechanism with servo motor control.

Although a tremendous amount of research has been directed towards understanding micropunching in metallic foil, there is no record of work done on micropunching polymeric films. Also, no research has been done to investigate the effect of different process parameters on maximum achievable porosity and web stress, which are very relevant topics in the development of synthetic scaffolds for tissue engineering applications.

2.3. Modeling Micropunching Using Finite Element Methods

All tissue scaffolds have features that range from submicron to sub-millimeter in size. As such, the underlying physics falls in the mesoscopic range. Production of components with features in the mesoscopic length scale has been of interest to researchers of not only the biomedical field, but also of electrical engineering.

Miniaturization of components through microfabrication techniques has been the driving force behind technology developments in the field of microelectromechanical systems for decades. However, the production rates through conventional micromanufacturing techniques such as micro machining and micro molding are often not high enough to meet the market economics of high volume and low cost. Therefore, researchers are focusing more towards microforming process for the last decade.

Microforming not only meets the efficient production rate requirements, the processes can increase component versatility and reliability due to the excellent mechanical properties of the applicable workpiece materials. Several microforming techniques such as micro-extrusion, micro bending, and micro blanking have been developed by different research groups over the last decade and have been modeled using the finite element method to understand the effect of material and processing requirements on finished part quality and equipment demands [74]. While most of the finite element modeling of microforming operations has considered metals as the workpiece material, it is worth mentioning different developments in the field as the same principles are likely to apply for the fabrication of tissue scaffolds from biodegradable polymers.

Blanking processes, where the nominal size of the blanks are at least an order of magnitude higher than the thickness of the sheet, can be assumed to be equivalent to simple plate shearing. Several other factors will contribute to the resultant product when the sheet thickness or the feature dimensions are of same size order as the grain size of the workpiece material. Plate shearing has been extensively studied both experimentally and through finite element simulations by different researchers. Since shearing and fracture during blanking or punching operations involve very high deformations and strain gradients, not all commercially available FE codes are suitable for simulating such

manufacturing processes. Codes such as DEFORM (an explicit Lagrangian solver used in this research) are developed specifically for simulating high deformations and have been used by industries for about two decades.

For shearing, or any other deformation-flow simulation, either a Lagrangian or Eulerian method can be used to solve the FE equation set. The Eulerian method has been proven to be less computationally expensive as it eliminates the need for frequent remeshing. It is best suitable for fluid flow simulation where a control volume approach can be used. However, it is not the preferred method when it comes to simulating fracture or shear where contact and large deformation are involved. In fracture or shear simulations new surfaces are formed and moved continuously, requiring a new control volume at each time step. In the Lagrangian method, this issue is resolved by frequent remeshing, with acknowledgement that it is more computationally demanding. Regardless, fracture behavior and surface generation can be easily incorporated in the Lagrangian method [54].

Solution methods to the FE equation are normally classified as *implicit* or *explicit*. With implicit computation, an iterative method is used to solve for the future state of the model after each increment of deformation i.e. to update the model from time t to $t + \Delta t$, the computation uses information at $t + \Delta t$. With the explicit method, the finite element equations are solved directly without the need for convergence criteria i.e. the model is updated from time t to $t + \Delta t$ by using information available at time t . There have been many studies comparing the two solution methods in metal forming simulations [55, 56]. In general, the explicit method is more suited for simulating the punching process because the implicit method can have difficulty converging to a solution when the elements experience large deformation and contact [55].

Shearing and fracture involve large deformations. Therefore, finite deformation formulations may seem appropriate. However, DEFORM is based upon incremental deformation or small deformation theory where processes involving large deformations and even rotations can be simulated as a combination of a large number of smaller steps [57]. If the step size is small enough no significant loss of accuracy occurs.

Details of the FE code DEFORM were first published in 1991 by Oh et al. [58]. DEFORM is capable of handling a wide variety of material models including viscoplasticity, thermoelasticity and powder materials under nonisothermal conditions. The most significant feature of DEFORM is automatic mesh generation based on a multiple number of criteria set by the user, such as boundary curvature, temperature distribution, strain distribution, strain rate distribution, and a user defined element size window [59]. Similarly, as the simulation progresses, the deformed geometry will be remeshed based on several other user defined criteria such as interference depth, stroke increment, time increment, and step increment. Besides these criteria, the geometry will be remeshed if the elements get distorted enough to generate a negative Jacobian, which will make the simulation unstable [59].

Out of several available solver types, 'Lagrangian Incremental' is best suitable for operations like punching, blanking, transient machining, forging, rolling, extrusion and other heat transfer and heat treat applications. DEFORM can solve highly nonlinear time dependent problems by creating a series of FE solutions at discrete time steps. At each step the values of some key variables such as velocities and temperatures are calculated based on the boundary conditions. All other derivable variables such as stress and strain are determined from these key variables. The solution increment step can be defined in terms of time, stroke length of the primary die or both, depending on the demands for resolution. The selection of time step or the stroke increment is based on a

few rules-of-thumb to avoid inaccuracies and instability in solutions. For example, for better accuracy the displacement of any node should not exceed 1/3 of the element side length in one simulation step and for simulations where the deformations are highly localized, it is advised to keep the time step as small as 1/10 of the element side length [59].

One of the major aspects of micropunching simulations is the ability of the code to accurately predict the shear failure i.e. initiation and growth of a fractured crack. There are many damage models that exist in the literature to predict fracture, with most based on plastic work done per unit volume. The threshold for damage formation is given by Equation 2.1

$$C = \int_0^{\bar{\epsilon}_f} f(\sigma_i) d\bar{\epsilon} \quad (2.1)$$

where $\bar{\epsilon}$ is the effective plastic strain, $\bar{\epsilon}_f$ is the effective plastic strain at fracture, and σ_i is the principle stress.

Several such damage criteria are described, and a new one is introduced, by Zhu et al. in 1992 [60]. One of the most widely used damage models was given by Cockcroft and Lantham about half a century ago in 1968, also intended to be used in this study [61]. The critical damage threshold for the Cockcroft and Lantham model is given by Equation 2.2

$$D = \int_0^{\bar{\epsilon}_f} \left(\frac{\sigma^*}{\bar{\sigma}} \right) d\bar{\epsilon} \quad (2.2)$$

where, D is the critical damage threshold, σ^* is the maximum principal stress, $\bar{\sigma}$ is the effective stress, $\bar{\epsilon}$ is the effective total strain, and $\bar{\epsilon}_f$ is the effective total strain at fracture.

The Cockroft and Lantham damage criteria has been successfully used by several researchers to predict shear fracture. In 2002, Domblesky and Zhao published a paper validating the use of this criterion in simulating plate shearing [62]. They demonstrated the effect of a critical damage value on the distribution of rollover, burnish, and fracture of a surface during plate shearing. Another paper published in the same year by Domblesky and Zhao further evaluated the damage criteria in predicting the microhardness of AISI 1020 steel plate numerically and comparing it with published experimental data [54].

In each of the aforementioned simulations, element deletion was used to initiate a fracture and to further propagate a crack. In DEFORM, all elements with an accumulated damage value more than the critical damage value are deleted, creating a crack or a void if the number of such elements exceeds a preset value, which is typically around 4 [59]. The element deletion method to propagate a crack may cause some loss of total volume, but it has been shown that if the elements are dense enough at the locations with high strains, the total volume loss after element deletion is negligible [54]. The application of DEFORM has been to study metals, but the transition to plastics is not considered to be problematic, as long as the proper material model is utilized.

The applicability of DEFORM to micropunching of metal foil is affected by the size effect. In macroscopic components, the material property is the aggregated average of the properties of all grains in the component and can be assumed to be homogeneous in nature. However, this is not the case with mesoscopic components, where the anticipated features are on the size scale as the grains in the workpiece. The material properties are highly anisotropic within a single grain. As the atomic lattice orientations vary from grain to grain, so are the material properties in a particular direction of the global coordinate system. This causes inhomogeneity in material properties across a

component. This not only makes the variance in the produced components high, but also makes the FE simulation of such production processes more challenging.

For macroscopic component fabrication, commercial FE software packages normally use continuum homogeneous material properties. However, for microforming processes, several modified finite element methods have been used. The most widely used method is Crystal Plasticity Finite Element (CPFE). Huang first wrote a user defined material model subroutine for CPFE to be used with Abaqus in 1991 [63]. In 1994, Shirkoohi, provided the finite element model for the grain induced anisotropy of steel [64]. A multiscale model, combining CPFE and atomistic simulations, was presented by Glaessgen and Saether for predicting the fracture along the grain boundaries of polycrystalline Aluminum [65]. In 2011, Hu et al. gave the constitutive relationship of an Aluminum alloy (AA 5754) based on CPFE [66]. At this time, it is unclear if CPFE is required to model micropunching in metallic foils, where thickness is on the same order as grain size, or if conventional FE methods can be employed to determine the maximum punching force.

In 2006, Geibdorfer et al. developed a mesoscopic numerical model for FE simulation of microforming processes [67]. They demonstrated the occurrence of size effect when the length scales are reduced from macroscopic scale to mesoscopic scale. The model was validated by comparing the forces measured from experiment to the forces obtained from numerical simulation. Several other authors have investigated and published demonstrating the size effect when length scales are changed and the feature dimensions are comparable to the grain sizes [67-73].

One difficulty of employing the CPFE method is that individual grains are required for meshing. Fortunately, in 2010 Cao et al. developed new software

(VGRAIN) for automatically generating virtual grains [74]. The workpiece with virtual grains can be imported into Abaqus, a commercially popular FE software. Within Abaqus, a user defined subroutine (UMAT) was written to incorporate the constitutive relations of crystal plasticity. The researchers were able to demonstrate, both experimentally and through CPFE simulations, the geometrical uncertainties of the final product (extruded micropin) when the feature dimensions are of the same order as the grain size. Figure 2.16(a) shows two extruded micropins with different grain sizes. One pin appears straight, while the other is bent. Using a CPFE model, Figure 2.16(b), simulations accurately predicted the experimental results, Figure 2.16(c).

The general CPFE constitutive equations and research completed so far were summarized in 2013 by Yang [75]. Due to the size effect and related material anisotropy, it would be very optimistic to expect the prediction of final hole geometry when simulating the micropunching process. However, one can expect to obtain useful information, such as maximum punching force, when simulated without using CPFE analysis. The focus of this research is to determine the accuracy of conventional FE methods when comparing predicted and measured forces during micropunching copper foil.

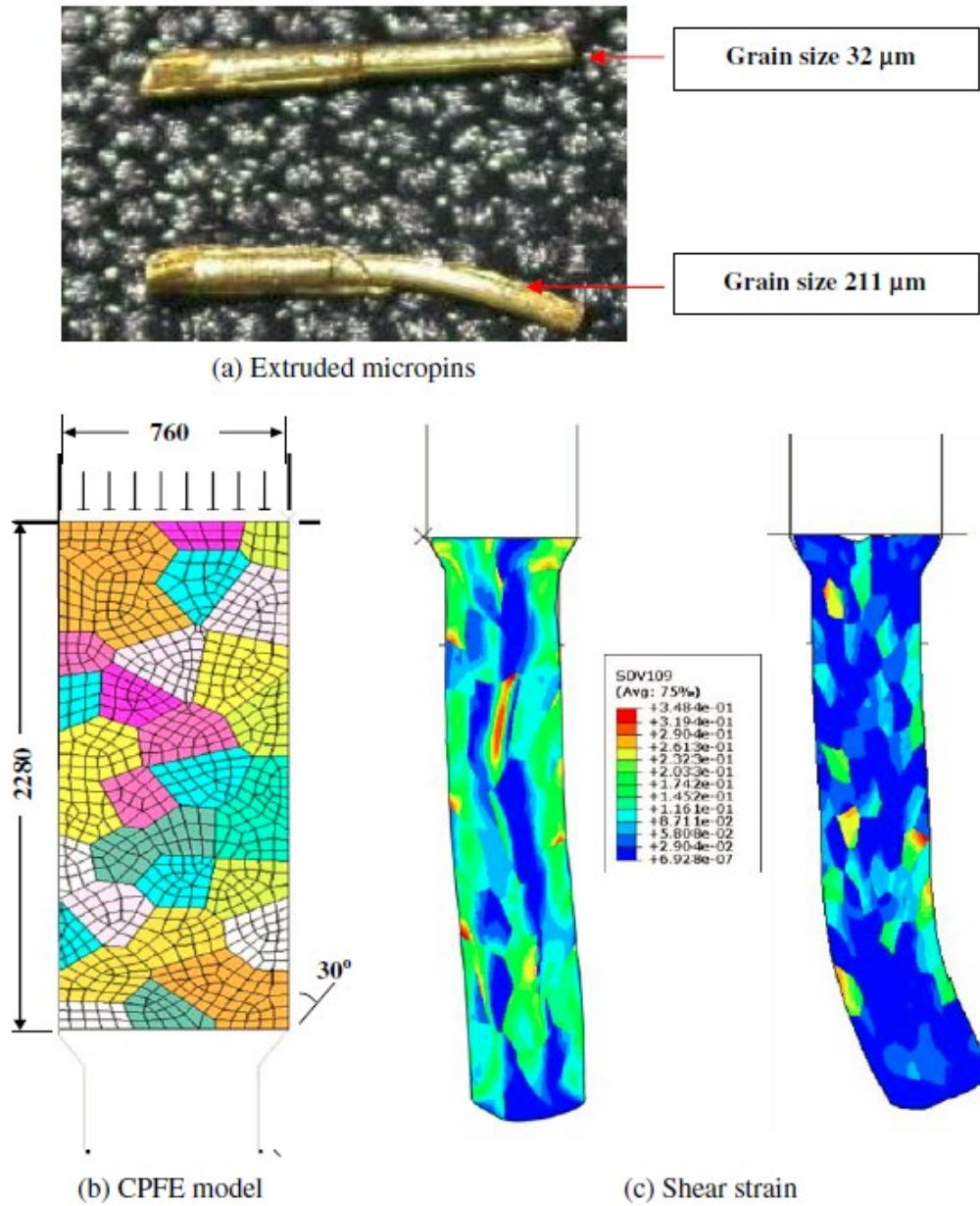


Figure 2.16 Comparison between experimental and simulated extruded micropins. Figure courtesy: [74]

2.4. Material Model for Polycaprolactone

An accurate material model for polycaprolactone is vital in performing the finite element analysis of the micropunching process. The most accurate method of defining a

material model within most finite element solvers is to create a look-up table of the measured true stress-true strain data, as opposed to estimating material behavior with a constitutive relationship. This data is more reliable if it can be obtained experimentally under conditions that represent the deformation process being modeled. PCL is one of the most important biodegradable materials and has heritage in the field of tissue engineering. Therefore, researchers have invested some attention in characterizing its stress-strain behavior. In 2010, Eshraghi et al. [21] provided comprehensive experimental results from uniaxial tensile testing of PCL for different types of microstructures, including a solid specimen as well as 1D, 2D and 3D microstructured scaffolds. Figure 2.17 shows the geometrical details of the different specimens used in the tensile tests.

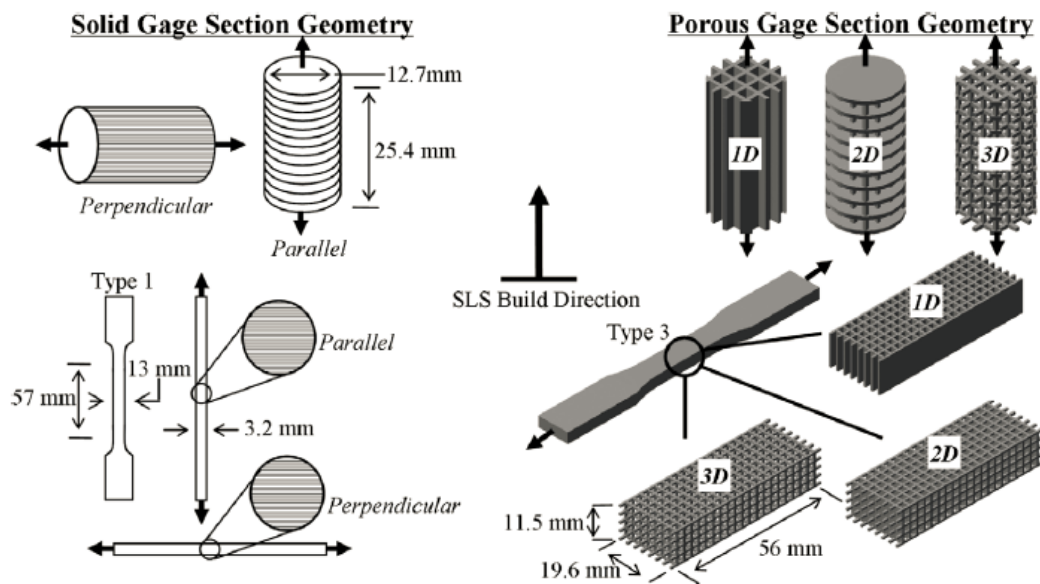


Figure 2.17 Different specimen geometries and their relative orientations with respect to load direction. Figure courtesy: [21]

Results of the various PCL tensile tests at room temperature are given in Figure 2.18. Eshraghi et al. also completed a detailed finite element analysis to numerically validate the stress strain behavior of the porous scaffolds. The results for the same are given in Figure 2.19. Besides their own findings, they have extensively reviewed the literature and reported material properties of PCL from other researchers. Findings from other researchers are listed in Table 2.3.

Property		Unit	SLS				
			Solid gage section		Porous gage section ¹		
			//	⊥	1D	2D	3D
Tension	Elastic modulus, e	MPa	363.4 ± 71.6	343.9 ± 33.2	140.5 ± 19.6	42.0 ± 6.9	35.5 ± 5.8
	0.2% Offset yield strength, σ_Y	MPa	8.2 ± 1.0	10.1 ± 1.5	3.2 ± 0.6	0.67 ± 0.08	0.67 ± 0.06
	Strain at yield, ϵ_Y	-	0.024 ± 0.006	0.031 ± 0.002	0.024 ± 0.001	0.017 ± 0.002	0.020 ± 0.002
	Ultimate tensile strength, σ_{UT}	MPa	10.5 ± 0.3	16.1 ± 0.3	4.5 ± 0.4	1.2 ± 0.2	1.1 ± 0.1
	Strain at break, ϵ_B	-	0.043 ± 0.007	8.0 ± 0.3	0.095 ± 0.022	0.092 ± 0.022	0.096 ± 0.025
Compression	Elastic modulus, E	MPa	297.8 ± 7.1	317.1 ± 3.9	133.4 ± 2.6	12.1 ± 0.5	14.9 ± 0.6
	0.2% Offset yield strength, σ_Y	MPa	12.5 ± 0.3	10.3 ± 0.2	4.25 ± 0.05	0.45 ± 0.01	0.42 ± 0.03
	Strain at yield, ϵ_Y	-	0.052 ± 0.003	0.037 ± 0.002	0.0370 ± 0.000	0.0376 ± 0.001	0.0268 ± 0.003
	Ultimate compressive strength	MPa	38.7 ± 0.3	38.80 ± 0.66	10.0 ± 0.62	0.60 ± 0.00	0.60 ± 0.00

Note: $\mu \pm \sigma$ where μ denotes the mean and σ denotes the standard deviation ($n = 6$).

¹ Porous compressive specimens tested parallel to SLS build direction, porous tensile specimens tested perpendicular to SLS build direction.

**Figure 2.18 Experimental results from tensile test of different PCL scaffold specimens.
Figure courtesy: [21]**

Table 2.3 Tensile properties of PCL reported by different researchers [21]

Reference	Method	Tensile	Tensile
		Modulus (MPa)	Strength (MPa)
Per Storpo [76]	Injection molding	430	
Pitt et al. [77]	Melt extrusion	264.8	
Wehrenberg [78]	Compression molding	340	19.3
Feng et al. [79]	Compression molding		21.6
Engelberg [80]	Compression molding	400	16
Vandamme and Legras [81]	Compression molding	251.9	
Rosa et al. [82]	Compression molding	429.1	16.9
Corello [83]	Injection molding	378	27.3
Granado [84]	Injection molding	300	14

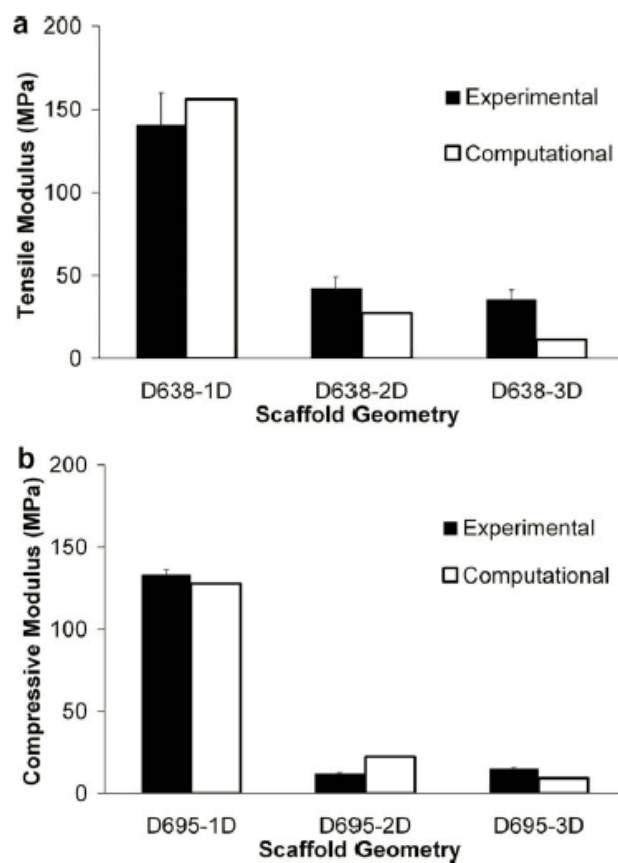


Figure 2.19 FEA simulation results for material properties of PCL scaffold specimens.
Figure courtesy: [21]

Similarly, Kurniawan et al. in 2011 experimentally determined the stress-strain behavior of PCL at low strains [85]. The objective of their study was to determine the elastic properties of PCL at both room temperature and simulated *in vivo* (body) temperatures for various strain rates. The results of their study are given in Figure 2.20 and Figure 2.21.

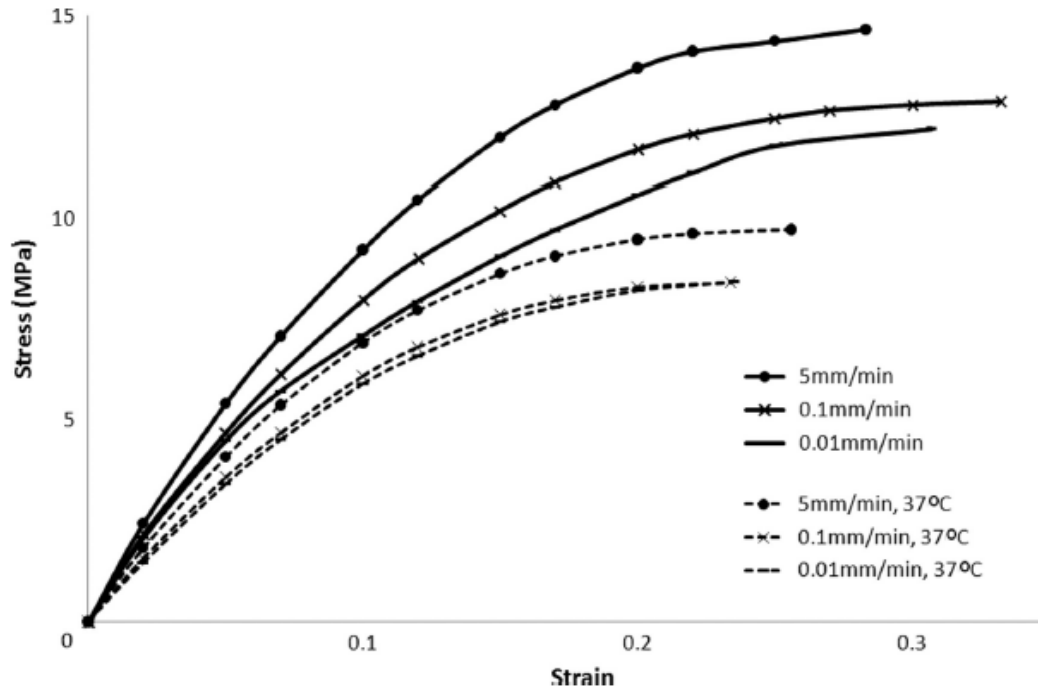


Figure 2.20 Stress-strain curve of PCL at various strain rates and temperatures. Figure courtesy: [85]

Strain rate (mm/min)	Temperature (°C)	Yield strength (MPa)	Tensile modulus (MPa)	Strain at yield (%)
5	23	14.66 ± 1.26	107.02 ± 3.99	28.3 ± 4.11
0.1	23	12.86 ± 0.82	90.14 ± 4.56	33.21 ± 0.92
0.01	23	12.19 ± 0.78	87.7 ± 5.05	30.73 ± 0.81
5	37	9.73 ± 0.53	80.8 ± 3.74	25.61 ± 1.02
0.1	37	8.42 ± 0.09	71.42 ± 0.54	23.42 ± 0.91
0.01	37	8.37 ± 0.18	68.45 ± 0.39	22.28 ± 0.53

Figure 2.21 Experimental stress-strain data of PCL at various strain rates and temperatures. Figure courtesy: [85]

Published data for stress-strain curves of PCL are sufficient for FEA simulations of conventional punching processes at room temperature. However, initial trials of PCL micropunching revealed that the material exhibited extreme plasticity, such that it was impossible to punch a clean hole without a small tentacle of material restricting separation of the punch-out. This problem was solved, as will be expounded upon in

upcoming sections, by reducing the temperature of the PCL membrane to below the glass transition, $-60\text{ }^{\circ}\text{C}$, thereby invoking a brittle material behavior during punching [86]. At this time, the existing literature does not include the stress-strain behavior of PLC at such low temperatures so it was determined as part of this research.

Chapter 3

Micropunching Copper Foils

3.1. Introduction

Miniaturization of components through microfabrication techniques is the driving force behind technology developments in the field of microelectromechanical systems. However, production rates of conventional micromanufacturing techniques such as micro-mechanical cutting, micro-molding, micro-extrusion, especially non-silicon and non-MEMS based methods, often conflict with market economics of high volume and low cost [87]. Therefore, over the last decade researchers have begun to focus on high throughput microforming processes.

Microforming not only meets efficient production rate requirements, the processes can increase component versatility and reliability due to superior mechanical properties of applicable workpiece materials [88]. Several microforming techniques, such as micro-extrusion, micro-bending, and micro-blanking, have been developed by various research groups and modeled using the finite element (FE) method to understand the effect of material and processing requirements on finished part quality and equipment demands [89].

Unlike macroscopic components, material properties of microscale features are neither homogeneous nor isotropic. As feature size of the component is reduced to the order of few grains or less, material inhomogeneity from the random orientation of

crystallographic planes becomes more prominent [74]. Even within a single grain, the mechanical properties may vary significantly depending on grain orientation relative to the strain field and preferred slip plane. Therefore, research has been directed towards understanding the effect of grain size on processing parameters, as well as on the quality of the final product for a variety of microforming processes [51, 52, 63-72, 74].

Given prior research on the size effect in microforming processes, it is unclear if conventional FE methods can be used to accurately predict the maximum force during micropunching or if the CPFE method must be employed when sample thickness and radial clearance is less than grain size. In this research, DEFORM v10.2.1 is used to predict the peak punching force while micropunching 200 μm diameter holes in 25 μm thick annealed copper foil for various die clearances.

3.2. Materials and Methods

3.2.1. Micropunching Machine

A micropunching machine designed by Schmitt [4] utilizes a microscope to align the male and female die halves by peering through the hole in the female die as the male punch is raised into position, Figure 3.1. The female die is fixed in place, while the male die is positioned by precision X-Y-Z- θ micrometer controlled staging, Figure 3.1(g).

The machine is capable of utilizing a variety of die sets. The dies can be fabricated from silicon lithographic processes, micromachining, laser cutting, or more conventionally as pins in die blocks, depending on the desired scale and feature shape. The die sets are secured in place by using vacuum, Figure 3.1(c). Parallelism between the male and female dies is obtained through a spherical bearing. The bearing is locked in place by vacuum after mating contact is made between the die halves, Figure 3.1(e). Once the dies are aligned in the X-Y plane, the male die is lowered in the Z direction,

leaving enough space for placing the workpiece material between the dies. After positioning the workpiece, punching is accomplished by hand rotating the micrometer on the Z-axis staging.

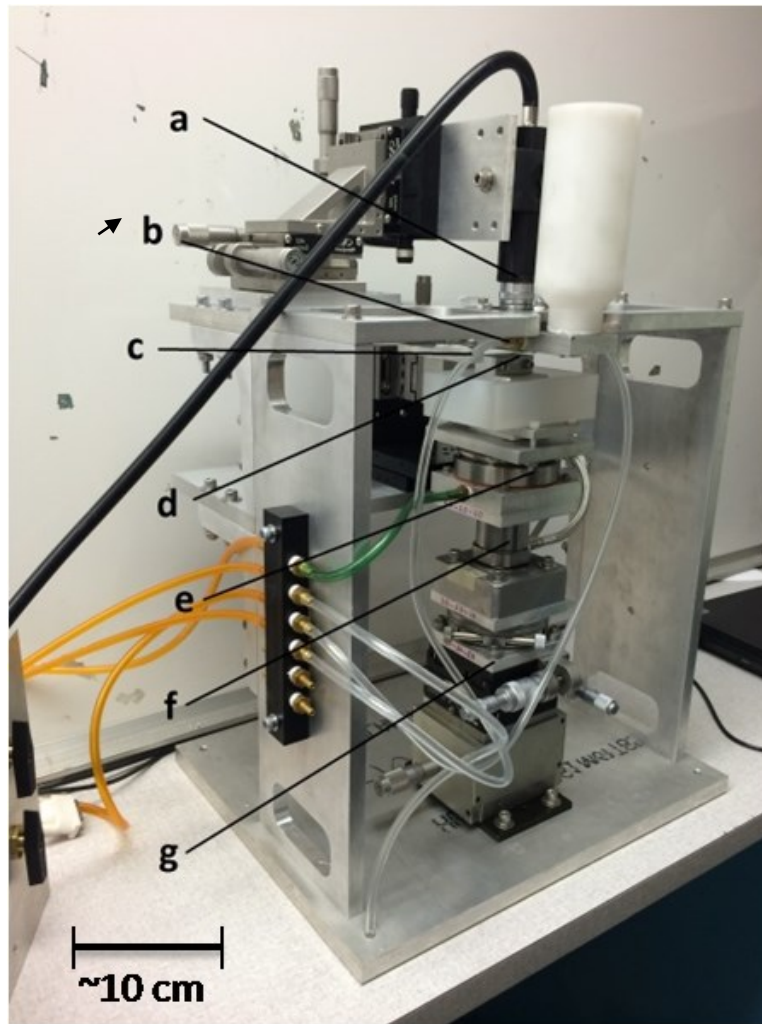


Figure 3.1 Micropunching setup (a) microscope, (b) female die holder (c) vacuum pad, (d) male die holder, (e) spherical bearing, (f) dynamometer, (g) X, Y, Z and θ stage.

Unlike conventional sheet metal punching processes, it is to be noted that no stripper plate is used in the present arrangement to hold the material while punching. Rather, the material is held in place by applying tension to the workpiece. Details of the design can be found in [4]. Elimination of the stripper plate reduces punch height. High

aspect ratio micropunches (tall punches with a small diameter) are susceptible to failure through side loads from die misalignment or buckling from high punching forces.

3.2.2. Workpiece Characterization

Annealed copper foil, 25 micron thick (Basic Copper, Carbondale, IL), is used as the workpiece material. A microstructure study of the copper foil using standard ASTM methods revealed that the average grain size is 47 μm . Grains within the plane of the foil do not exhibit distortion in a preferred direction, but rather equiaxed grains appear to have formed as a result of the recrystallization process.

3.2.3. Die Sets

Stainless steel gage pins, 200 μm in diameter (Model 21135A71, McMaster-Carr, Princeton, NJ, USA), are used for all micropunching experiments. The female die is manufactured by laser cutting holes in 150 μm thick, ground stainless steel plate (Photo Etch Technology, Lowell, MA, USA). Attenuation of the laser results in a tapered hole, where the entrance side of the laser creates a larger hole diameter than the exit side. The female dies are oriented within the micropunching machine so that the smaller hole is facing the male punch. The female die was produced with a pattern of holes to represent four different die clearances, Table 3.1.

Table 3.1 Description of dies sets used for micropunching copper foil (25 μm thick).

Punch Diameter (μm)	Hole Diameter ¹	% Die Clearance ²
200	203.8	7.6%
200	209.2	18.4%
200	212.0	24.0%
200	224.0	48.0%

¹Exit side of the laser cut hole

²Die clearance = (radial clearance / material thickness)

Typical die clearance in a macro-scale stamping operation is approximately 4% to 10%. In this research, however, a broader range of die clearance is investigated to explore the effect of increasing die clearance on peak punching force, while making sure radial clearance is always less than grain size.

3.2.4. Force Measurement

Punching force is measured in real-time with an inline 3-component quartz dynamometer (9047C, Kistler Instruments, Switzerland), Figure 3.1(f). The dynamometer has a dynamic range of 30kN in the punching direction with a measurement sensitivity of 3.7 pC/N. Data from the dynamometer is transmitted to a charge amplifier (ICAM 5073, Kistler Instrument Corp., Amherst, NY), which has a sensitivity of 1+/- 0.5% pC/mV. High speed data acquisition is achieved with a multifunction data acquisition board (PCI 6132, National Instruments, Austin, TX), which has a simultaneous sampling rate of 2.5×10^6 samples per second. A LabVIEW (National Instruments, Austin, TX) virtual instrument code was written to stream the sampled data to a series of CSV files, at which point they were imported into MATLAB (MathWorks, Natick, MA) for analysis.

The noise in the force data is approximately +/- 0.1 N. The raw data is filtered using the “LOWESS” (locally weighted scatter plot smooth) function in MATLAB. It is a local linear regression filter with a tricube weight function given by Equation 3.1

$$w_i = \left(1 - \left|\frac{x - x_i}{d(x)}\right|^3\right)^3 \quad (3.1)$$

where x is the predictor value, x_i are the neighboring points with i increasing from the smallest to the largest value of the span, and $d(x)$ is the distance between x and the farthest point in the span along the abscissa.

3.2.5. Finite Element Method

DEFORM v10.2.1 (Scientific Forming Technology Corporation, Columbus, OH, USA) is used to simulate micropunching for each case considered in the experiments. DEFORM is an explicit finite element code widely used in metal forming industries and is optimized to simulate high deformation and contact. Unlike most punching simulations in the literature where a 2D axisymmetric model is used, a 3D finite element model is considered in this study to retain the ability to assign non-axisymmetric boundary conditions. Also, this ensures a valid comparison with multiple hole punching simulations to be considered in future research.

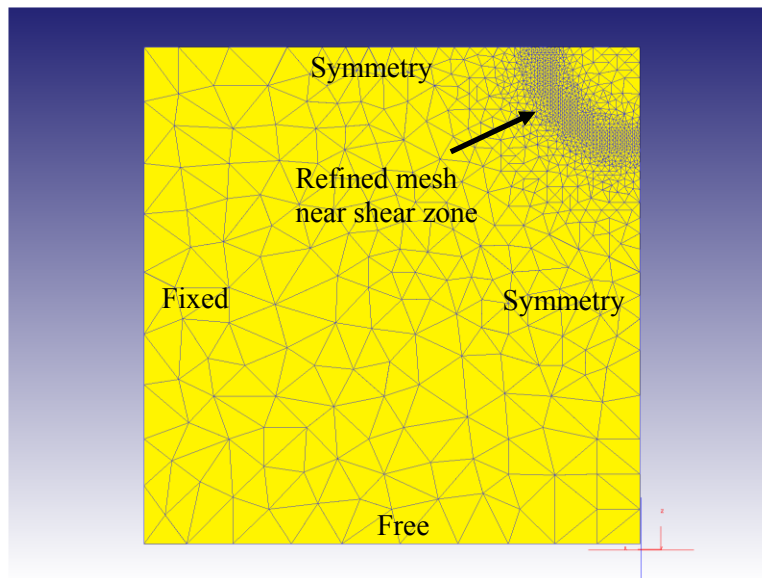


Figure 3.2 Boundary conditions for a quarter model considered for all simulations to predict peak punching force

As in the experiment, there are three parts of the model: female die, male die, and workpiece. In the experiment, the female die base is approximately 25 mm by 25 mm square and the strip of copper foil is approximately 12 mm wide by 125 mm long. However, in the FE model, a 1 mm by 1 mm section of the die and workpiece is considered to avoid an unnecessarily high number of elements after meshing. Within this

modeling space, the boundary conditions have a negligible influence because: (1) the workpiece dimension is approximately five times the anticipated hole diameter, and (2) the deformation and stress is localized in the radial clearance, which is 12 μm for the maximum clearance case.

To keep the model representative of the actual experimental setup, one direction of the workpiece is fixed while the other direction is free to move. As one can imagine, although the boundary conditions are not axisymmetric, the arrangement affords planar symmetry about both axes on the workpiece plane. Therefore, only one quarter of the model is simulated to reduce the computational time.

There are two contact interfaces in the current finite element model: (1) between the workpiece and the male die, and (2) between the workpiece and the female die. Both interfaces are assigned friction boundary conditions with the material pair as copper and stainless steel. Therefore, the coefficient of friction used for both cases is 0.22, which was obtained from literature [90]. This friction coefficient value also matches closely with static and sliding friction coefficients as 0.23 and 0.21, respectively, obtained using Flat-On-Flat (FOF) test method as given in [91].

3.2.6. Workpiece Material Model

Two different material models were simulated for annealed copper, one with strain hardening and one with strain rate hardening. DEFORM allows to use of Ludwik's equations, as given by Equations 3.2 and 3.3, for a material model if the strength index and the hardening exponents are available:

$$\sigma = Y + K \varepsilon_p^n \quad (3.2)$$

$$\sigma = Y + C \dot{\varepsilon}_p^m \quad (3.3)$$

where σ is the flow stress, ϵ_p is the effective plastic strain, $\dot{\epsilon}_p$ is the effective plastic strain rate, Y is the yield strength, K and C are strength indices, and n and m are the hardening exponents. The values of all parameters in the material models for annealed copper are available in the literature as summarized in Table 3.2 [89].

Considering the two material models presented here, the strain only model is to be used when the strain rates are expected to be low i.e. for a quasi-static case or for a material which is known for strain rate independent behavior. On the other hand, if the strain rates ($10^2 s^{-1}$ to $10^5 s^{-1}$) are very high to significantly increase the flow stress, the strain rate dependent constitutive model is to be used.

In the current study, the punch speed is set to be 50 microns per second with a workpiece thickness of 25 microns. These processing conditions result in a moderate initial average strain rate of $2 s^{-1}$. Therefore, results from both material models are presented.

For the best simulation results, the constitutive model should be experimentally determined to have an accurate estimate of the parameters and their values given in Table 3.2. However, in the current research, the parameters obtained from literature are used to demonstrate the robustness and error levels of such finite element simulations to predict peak punching force.

Table 3.2 Material parameters for annealed copper [89]

Parameter	Value
Y	76 MPa
K	315 MPa
C	240 MPa
n	0.54
m	0.06

DEFORM allows initiation and propagation of fracture based on a damage criteria method. The damage criterion used in this research is the Normalized Cockroft and Lantham model [62, 59, 61]. The critical damage threshold for this model is given by Equation 3.4

$$D = \int_0^{\bar{\epsilon}_f} \left(\frac{\sigma^*}{\bar{\sigma}} \right) d\bar{\epsilon} \quad (3.4)$$

where D is the damage value, σ^* is the maximum principal stress, $\bar{\sigma}$ is the effective stress, $\bar{\epsilon}$ is the effective total strain, and $\bar{\epsilon}_f$ is the effective total strain at fracture. The typical value of critical damage threshold for engineering materials lies between 0.35 and 0.43, with higher values indicating higher ductility [62]. Since annealed copper is a relatively ductile material, a critical damage threshold of 0.5 is used for all simulations.

DEFORM gives the option of representing fracture by two methods, either element deletion or element softening. In the current research on copper foil, element softening is used for all simulations as it is computationally less demanding.

Both the male and female dies are modeled as rigid, while workpiece meshing is done automatically depending on the local strain and strain rate distribution. A convergence study revealed that an element size of 2 μm in the high deformation zone at the beginning of the simulation yielded accurate results. The smallest element size measured in the high deformation zone was between 1 μm to 2 μm and the largest element size in the low deformation zone was approximately 20 μm during the simulation. The total number of elements in the quarter symmetry model was approximately 100,000 and took slightly more than one hour to run on a computing cluster with four parallel processors.

Figure 3.3 shows a FE model at the beginning of a simulation. In order to keep the total computational time low without losing accuracy, a solution increment step size of $0.2 \mu\text{m}$ was used. The increment step was obtained through a convergence study.

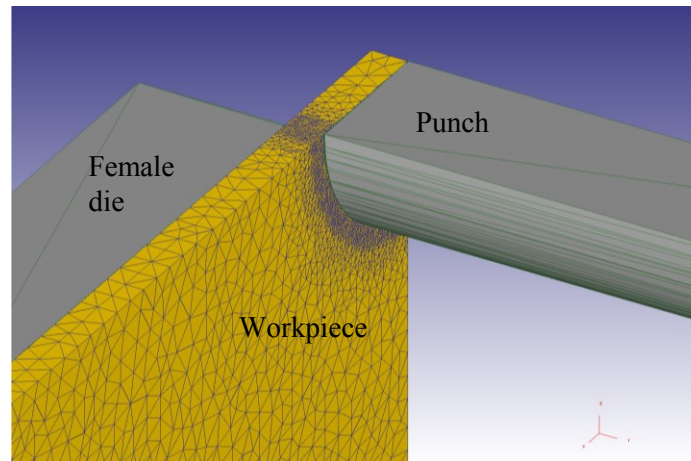


Figure 3.3 FE model of the micropunching process

3.2.7. Statistical Methods

A pilot study at 7.6% die clearance resulted in a mean peak punching force of 3 N with a standard deviation of 0.22 N ($n = 20$). An effect level of 10 % of the mean value (0.3 N) was set to calculate the sample size for a power of 90 % and α of 0.05. The calculated sample size was 12.

3.3. Results

3.3.1. Copper Micropunching Experiments

Mean maximum punching force is measured for each of the four dies. At least 25 holes are punched for each case, which exceeds the sample size requirements for a detection of a 10 % change from the mean maximum punching force at 90% power.

Figure 3.4 shows a comparison of mean peak punching force obtained for all four cases of die clearance. From the experiments, it is evident that die clearance does not have a significant influence on mean maximum punching force (t-test, $p > 0.05$ for all comparisons).

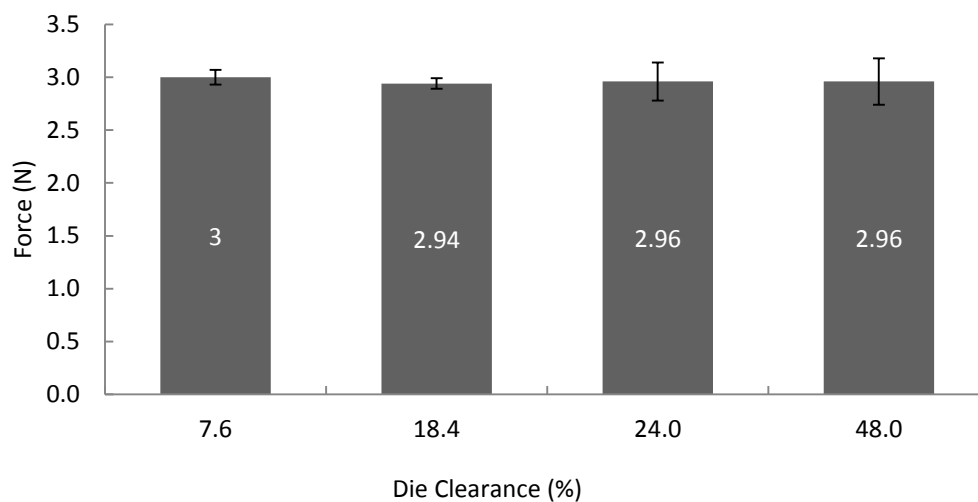


Figure 3.4 Comparison of maximum punching force for each die clearance (mean +/- SD).

The quality of holes fabricated using different die clearances is investigated by analyzing SEM images. The hole geometry for all four cases of clearance is given in Figure 3.5. The measured hole sizes and outside diameter of an apparent burr ring (refer to the arrow in Figure 3.5(d)) is summarized in Table 3.3.

Table 3.3 Comparison of measured hole sizes (mean +/- SD)

Die Clearance	Hole Diameter (um)	Burr Ring, Outside
7.6%	200.0 +/- 0.5	223.0 +/- 1.2
18.6%	199.9 +/- 0.7	227.9 +/- 0.7
24.0%	200.2 +/- 0.7	231.0 +/- 1.0
48.0%	199.9 +/- 0.8	241.0 +/- 1.5

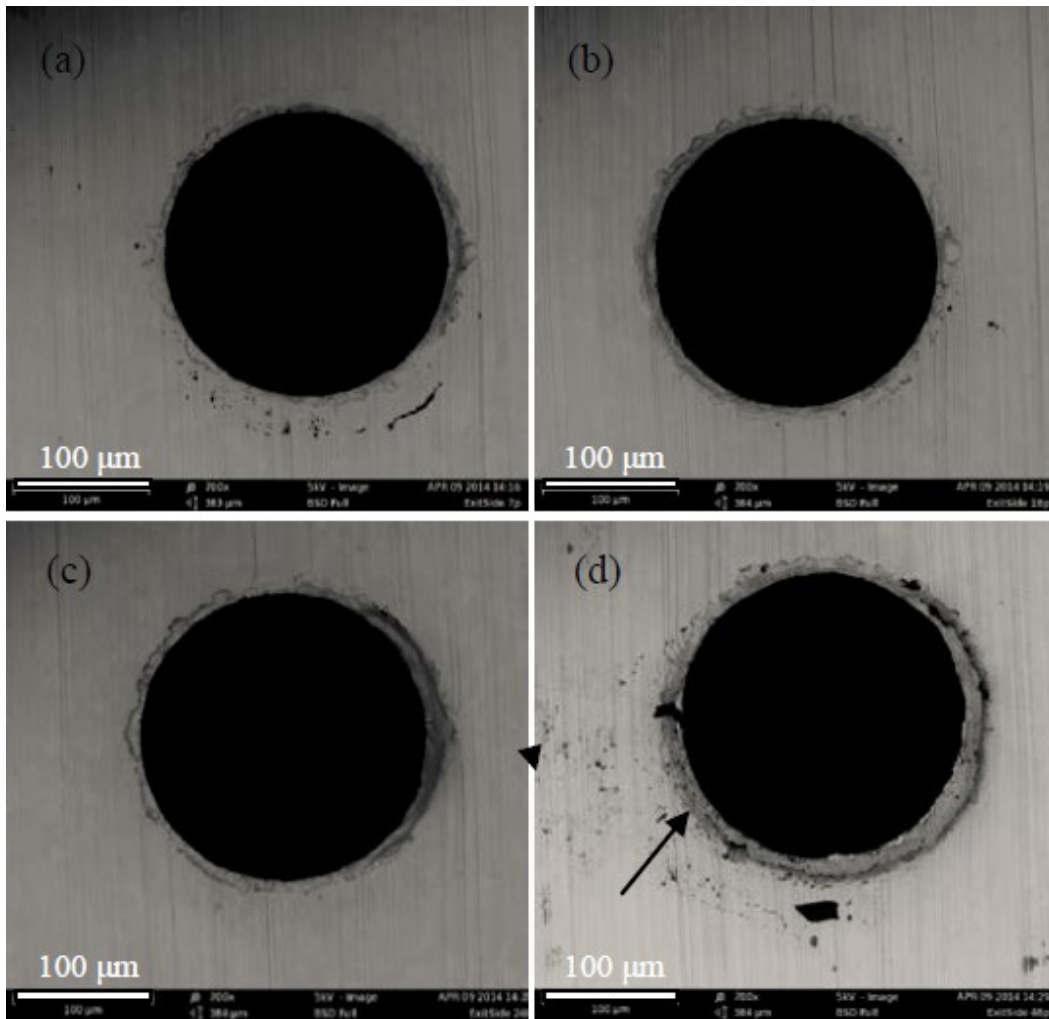


Figure 3.5 SEM images of a burr ring (arrow) surrounding the exit side of the micro-punched holes. Die clearance: (a) 7.6 %, (b) 18.6 %, (c) 24.0 % and (d) 48.0 %

3.3.2. Finite Element Simulation Results

Simulation results are analyzed using the DEFORM post processor. Stress and strain distribution plots are obtained for a punch stroke of $8\ \mu\text{m}$ (32% of material thickness) as shown in Figure 3.6 and 3.7.

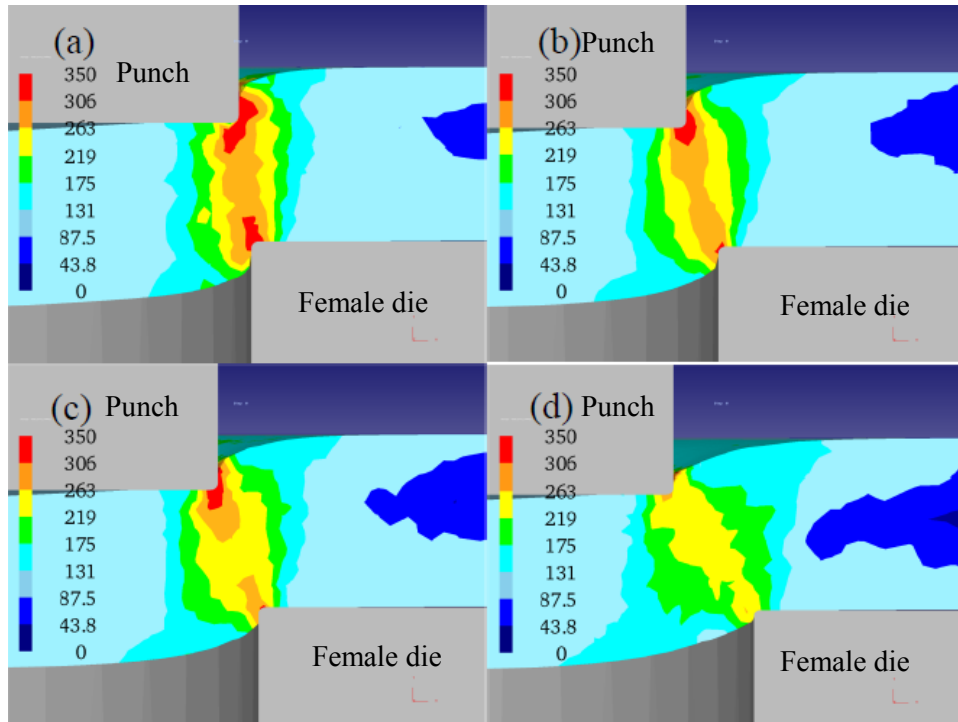


Figure 3.6 Comparison stress distribution contours for clearances (a) 7.6 %, (b) 18.6 %, (c) 24.0 % and (d) 48.0 %

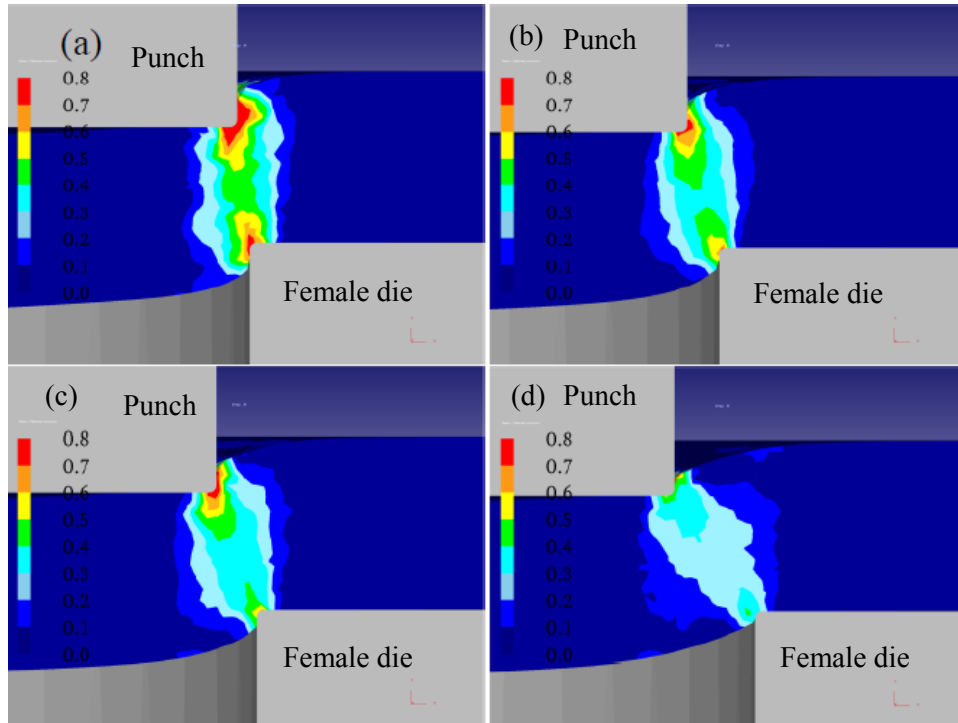


Figure 3.7 Comparison of strain distribution contours for clearances (a) 7.6 %, (b) 18.6 %, (c) 24.0 % and (d) 48.0 %

3.3.3. Comparison of Modeling and Experiment

The peak punching force is obtained through simulation using both the strain hardening and strain rate hardening material models. Figure 3.8 shows a comparison of simulation results for both material models as compared to the experimental results.

Assuming a homogeneous workpiece, the peak punching force can also be estimated using the conventional formula for hole punching [92].

$$F = 2\pi r S_f S_u \quad (3.5)$$

where F is the punching force, r is the nominal hole radius (100 μm), S_f is a shearing factor equal to 1 for micro-punching arrangements, and S_u is the ultimate tensile strength of the workpiece, 210 MPa for annealed copper [90].

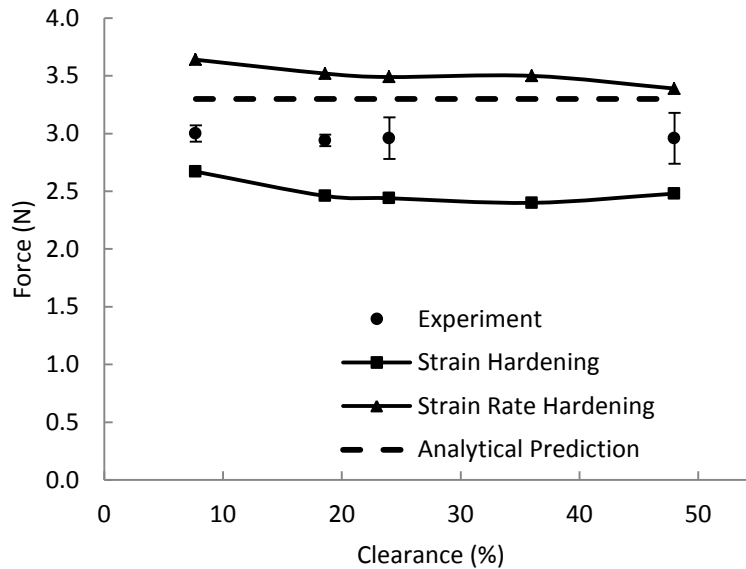


Figure 3.8 Comparison of simulation and experimental results (mean +/- SD) for maximum punching force

3.4. Discussion

In the case of a conventional macro-punching or blanking process, it is known that the peak punching force varies and has a minima as the radial die clearance is increased from low to high values [93]. Therefore, the clearance is always set to the optimum value to reduce tool stresses and wear. One would expect similar phenomena in the case of micropunching, if only it can be assumed as a scaled down model of the conventional macro-punching process and the material still remains homogeneous. However, as shown in Figure 3.4, when grain size is larger than radial clearance there is little change in the peak punching force for cases with different die clearance. The peak punching force is almost saturated at approximately 3N. This is in contradiction to the standard macro-punching results.

With knowledge of average grain size in the workpiece material and the die geometries, it is clear that micropunching occurred in a zone with high material inhomogeneity. As punching was predominantly through a single grain across the foil thickness, and less than a grain in the direction of radial die clearance, one would expect to encounter size effect due to reduced length scale and thus may consider simulating using CPFEM tools. However, the conventional FE tool, DEFORM, was able to predict the peak punching force within reasonable accuracy. The maximum error is approximately 21.3% for the case of 7.6% die clearance when using the strain rate hardening material model. For the strain hardening material model, the maximum error is reduced to 17.6%. These error levels are not unusual when simulating high deformation nonlinear contact and fracture problems, even when the material properties are determined experimentally.

The reason for this ability of conventional FEA to predict peak punching force could be that, since copper has FCC (Face Centered Cubic) crystal structure, it has many

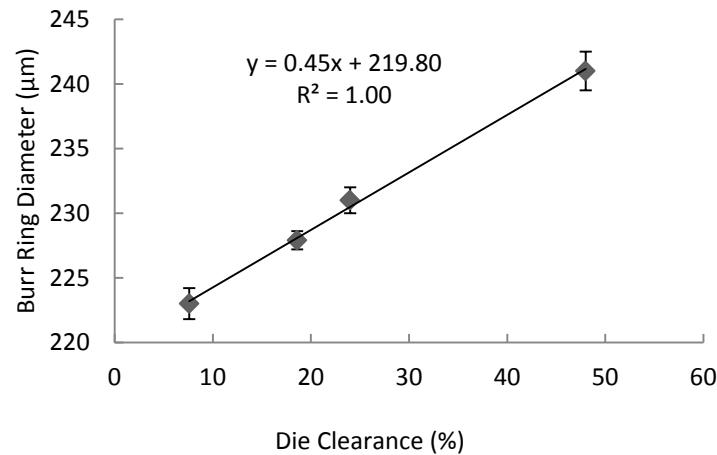
slip planes along which grains can deform. As punching of circular holes are considered in this research, an arc of the perimeter across a grain is likely to encounter many slip planes in different directions averaging out the inhomogeneity in material properties. Therefore, it may be possible that for a material with relatively less number of slip planes, and for punching non-circular holes, for example a square hole, the material inhomogeneity will not average out, and the conventional FEA may not be able predict the punching force with high accuracy.

From the SEM images shown in Figure 3.5, it is apparent that hole quality degrades as the clearance increases, similar to what one would expect in a macro-punching scenario. Also, Figure 3.5(d) shows eccentricity between the hole and the burr ring, which is likely due to die misalignment. With higher clearance, such die misalignment is found for most of the 48 % clearance punched microholes, particularly because the punch has more space in the radial direction to shift due to a non-axial bending load as a result of material inhomogeneity.

Table 3.3 summarizes hole size for all four cases of die clearance. The through hole diameters for each case match closely with the punch diameter (200 μm). There is no statistically significant evidence that hole diameters are any different than punch diameter ($p > 0.05$ for all comparisons). However, the size of the deformed zone on the exit side (ring formed due to burr) varies with clearance. Table 3.4 summarizes the comparison of measured burr ring sizes. The calculated p values indicate that the differences between their means are statistically significant. Also, a strong correlation is observed between die clearance and the burr ring size as shown in Figure 3.9.

Table 3.4 Measure of statistical significance (p values) for burr ring outside diameter

Clearance	18.6 %	24.0 %	48.0 %
7.6 %	0.0004	0.0001	0.0001
18.6 %		0.0006	0.0001
24.0 %			0.0001

**Figure 3.9 Correlation between die clearance and the outside diameter of the burr ring formed on the exit side of the micropunched holes.**

The strain distribution plot, given in Figure 3.7, shows that most of the deformation occurs in the radial clearance zone, supporting the validity of the modeled workpiece size and insensitivity to boundary conditions. An element softening fracture representation does not provide clear visualization of hole geometry. However, the stress concentrations hint at crack initiation at the tool tips, which was not observed in experiment.

3.5. Conclusion

Micro holes with a nominal diameter of 200 μm are punched in 25 μm thick annealed copper foil (47 μm grain size) for four different die clearances (7.6% to 48%). The peak punching force was approximately 3N for all four cases indicating no significant variation with respect to die clearance when radial clearance is less than grain size. The micropunching process was simulated using conventional finite element software, DEFORM. The predicted punching force was close to the experimental values with the worst case error of 21.3%. Thus, it can be concluded that the Crystal Plasticity Finite Element method may not be necessary to predict peak punching force for the category of micropunching process considered in this study.

Chapter 4

Modification of Punch Geometry

4.1. Introduction

It is well known in industry that the flat face of a circular punch can be modified to reduce the maximum punching force. For example, the face of the punch can be ground to create a single slanted surface, Figure 4.1. During punching, the slanted face creates a “can opener” effect, where the perimeter of the intended hole in the workpiece is incrementally sheared, rather than using a flat face where the full perimeter is engaged simultaneously.

A single slanted punch face greatly reduces the maximum punching force, but the off-axis punching load creates an unwelcome bending moment. This can lead to punch interference with the female die if bending deflection of the punch is greater than die clearance. To eliminate a bending moment, a symmetrical double slanted face can be used, although the punching force is higher than experienced with a single slanted punch.

In this research, analytical models are presented for both a single sided and a symmetrical double sided slanted punch to predict the maximum punching force profile as a function of slant angle. Analytical results are then compared to the force-stroke profile obtained from a finite element simulation when micropunching 25 μm thick copper foil.

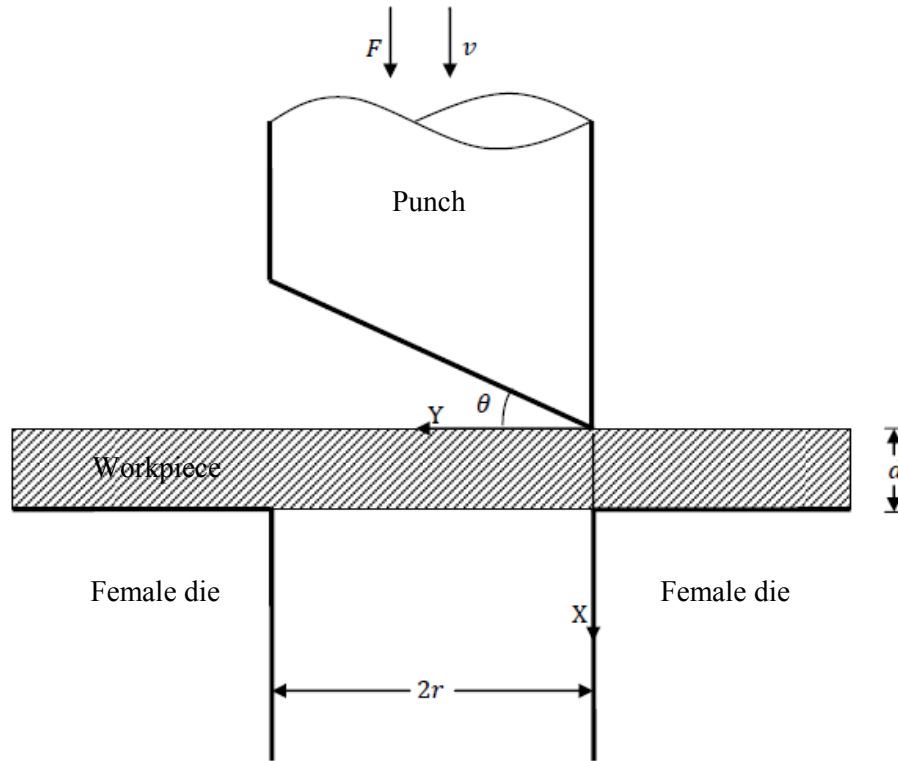


Figure 4.1 Schematic of a punching process using a single slanted punch

For the analytical developments of both a single and double slanted punch, it is hypothesized that punching force at any instant is a function of rate of change of the shear area at that instant and increases as the rate of shear area increases. For simplicity, as a first order approximation, the function can be assumed to be linear and therefore, we can write

$$F = K \frac{dA}{dt} \quad (4.1)$$

where K can be a function of model geometry and material properties, and may be determined analytically or through experiments for different materials. In the current study, F is obtained through finite element simulations and $\frac{dA}{dt}$ is obtained analytically.

Both of these quantities are normalized and compared to see if there is any association between them.

The deformation zone in the die clearance is complex and may not be simple shear across the whole workpiece thickness. However, in order to calculate the rate of change of shear area during slanted punching, it is assumed that simple shearing is occurring across the workpiece thickness with zero die clearance and, the shear area is equivalent to the contact area between the cylindrical surface of the punch and the workpiece. The coordinate system used has the X direction in the vertically downward direction along the punch velocity and the origin at the tip of the slanted punch.

4.2. Single Slanted Punch

Three stages can be defined to calculate rate of change of shear area, Figure 4.2:

- I. When the punch tip is within the thickness of the workpiece;

$$0 \leq X < d \quad (4.2)$$

- II. When the punch tip has crossed the workpiece material thickness, but the trailing end of the slanted punch surface has not yet reached the workpiece; and

$$d \leq X < 2r \tan \theta \quad (4.3)$$

- III. When the trailing end of the slanted punch surface is within the workpiece material thickness.

$$2r \tan \theta \leq X \leq (2r \tan \theta + d) \quad (4.4)$$

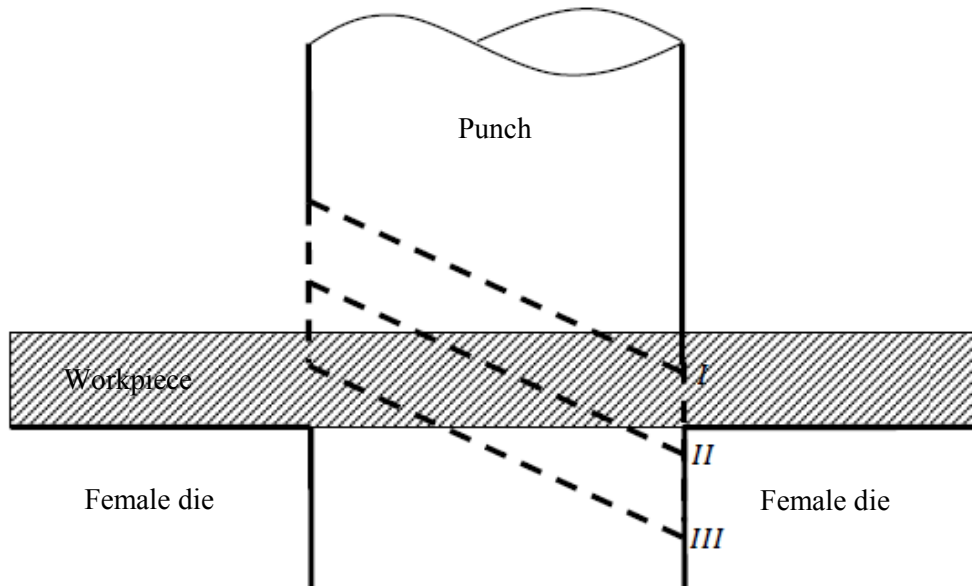


Figure 4.2 Schematic of three different stages of punch stroke

4.2.1. Stage I

When determining the total shear area as a function of stroke length, X , an elemental area of thickness dx at a distance of x is prescribed from the top surface of the workpiece, Figure 4.3. Considering triangle ABC,

$$\frac{x}{y} = \tan \theta \quad (4.5)$$

and upon simplification Equation 4.5 becomes

$$y = x \cot \theta \quad (4.6)$$

Similarly, considering triangle DEC,

$$\frac{X}{Y} = \tan \theta \quad (4.7)$$

and upon simplification

$$Y = X \cot \theta$$

(4.8)

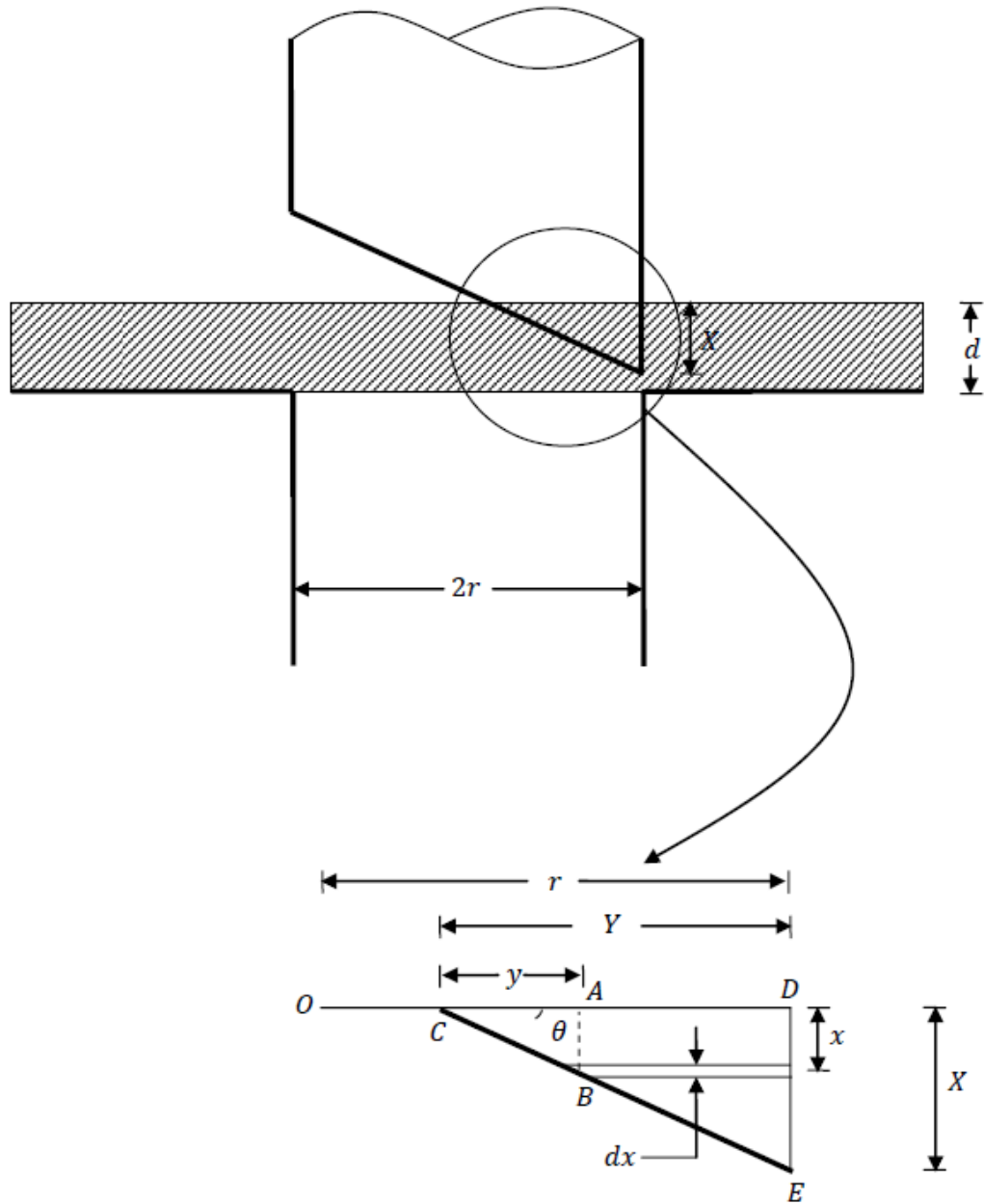


Figure 4.3 Schematic of shear area for Stage I stroke length

Now, the perimeter length of the elemental area constituting Stage I (subscript notation “1”), can be written as

$$L_1 = 2\alpha r \quad (4.13)$$

Substituting the value of α from Equation 4.13 into Equation 4.12,

$$L_1 = 2r \cos^{-1} \left(\frac{r - X \cot \theta + x \cot \theta}{r} \right) \quad (4.14)$$

Therefore, the shear area of the element from Stage I can be written as

$$dA_1 = L_1 \cdot dx \quad (4.15)$$

and upon integrating Equation 4.15,

$$A_1 = \int_0^x L_1 \cdot dx \quad (4.16)$$

Substituting the expression for L_1 from Equation 4.14 into Equation 4.16,

$$A_1 = \int_0^x 2r \cos^{-1} \left(\frac{r - X \cot \theta + x \cot \theta}{r} \right) \cdot dx \quad (4.17)$$

Upon simplification, Equation 4.17 can be rewritten as

$$A_1 = \int_0^x 2r \cos^{-1} \left[\left(\frac{r - X \cot \theta}{r} \right) + \left(\frac{\cot \theta}{r} \right) x \right] \cdot dx \quad (4.18)$$

To facilitate integration of Equation 4.18, consider a variable substitution, where

$$a = \frac{r - X \cot \theta}{r} \quad (4.19)$$

and

$$b = \frac{\cot \theta}{r} \quad (4.20)$$

Substituting the values of a and b in Equation 4.18,

$$A_1 = 2r \int_0^X \cos^{-1}(a + bx) \cdot dx \quad (4.21)$$

Equation 4.21 can be integrated analytically according to the following,

$$A_1 = \left(\frac{2r}{b}\right) \left[(a + bx) \cos^{-1}(a + bx) - \sqrt{1 - (a + bx)^2} \right]_0^X \quad (4.22)$$

and upon simplification,

$$A_1 = \left(\frac{2r}{b}\right) \left[\left\{ (a + bX) \cos^{-1}(a + bX) - \sqrt{1 - (a + bX)^2} \right\} - \left\{ a \cos^{-1}(a) - \sqrt{1 - a^2} \right\} \right] \quad (4.23)$$

and further refinement of Equation 4.23,

$$A_1 = \left(\frac{2r}{b}\right) \left[-a \cos^{-1}(a) + \sqrt{1 - a^2} \right] \quad (4.24)$$

Now, upon variable substitution of a and b from Equations 4.19 and 4.20, respectively,

$$A_1 = \left(\frac{2r^2}{\cot \theta}\right) \left[-\left(\frac{r - X \cot \theta}{r}\right) \cos^{-1}\left(\frac{r - X \cot \theta}{r}\right) + \sqrt{1 - \left(\frac{r - X \cot \theta}{r}\right)^2} \right] \quad (4.25)$$

Rearrangement of Equation 4.25 in terms of b becomes,

$$A_1 = \left(\frac{2r^2}{\cot \theta}\right) \left[-(1 - bX) \cos^{-1}(1 - bX) + \sqrt{1 - (1 - bX)^2} \right] \quad (4.26)$$

noting that

$$a = (1 - Xb) \quad (4.27)$$

In order to obtain the rate at which the shear area changes during punching, the time derivative of Equation 4.26 is calculated as follows

$$\frac{dA_1}{dt} = \left(\frac{2r^2}{\cot \theta}\right) \left[\frac{d}{dt} \left\{ \sqrt{1 - (1 - bX)^2} \right\} - \frac{d}{dt} \left\{ (1 - bX) \cos^{-1}(1 - bX) \right\} \right] \quad (4.28)$$

where the derivative of the second term on the right hand side of Equation 4.28 is

$$\frac{d}{dt}\{(1-bX)\cos^{-1}(1-bX)\} = \left[-b\cos^{-1}(1-bX) + \frac{b(1-bX)}{\sqrt{1-(1-bX)^2}} \right] \frac{dX}{dt} \quad (4.29)$$

and the derivative of the first term on the right hand side of Equation 4.28 is

$$\frac{d}{dt}\{\sqrt{1-(1-bX)^2}\} = \left[\frac{b(1-bX)}{\sqrt{1-(1-bX)^2}} \right] \frac{dX}{dt} \quad (4.30)$$

Combining Equations 4.29 and 4.30,

$$\begin{aligned} \frac{dA_1}{dt} = \left(\frac{2r^2}{\cot\theta} \right) & \left[-b\cos^{-1}(1-bX) + \frac{b(1-bX)}{\sqrt{1-(1-bX)^2}} \right. \\ & \left. - \frac{b(1-bX)}{\sqrt{1-(1-bX)^2}} \right] \frac{dX}{dt} \end{aligned} \quad (4.31)$$

and upon simplification of Equation 4.31,

$$\frac{dA_1}{dt} = \left[2r\cos^{-1}\left(1 - \frac{X\cot\theta}{r}\right) \right] \frac{dX}{dt} \quad (4.32)$$

Considering a constant punch velocity, dX/dt can be replaced with v and Equation 4.32

can be rewritten as

$$\frac{dA_1}{dt} = \left[2r\cos^{-1}\left(1 - \frac{X\cot\theta}{r}\right) \right] v \quad (4.33)$$

Equation 4.33 expresses the rate of change of shear area for Stage I in terms of punch geometry, radius r and slant angle θ , and in terms of punch speed v . A similar derivation is pursued to obtain shear area expressions for Stages II and III.

4.2.2. Stage II

During Stage I, the shear area was represented by a triangle, but as the punch enters Stage II the area becomes a parallelogram that is transposed on a cylindrical surface. A front projection view is sufficient to define the boundaries of parallelogram $PQRS$, Figure

4.5, as accompanied by the isometric view, Figure 4.6, which shows the propagation of the shear area at three different times according to the depth of punch penetration.

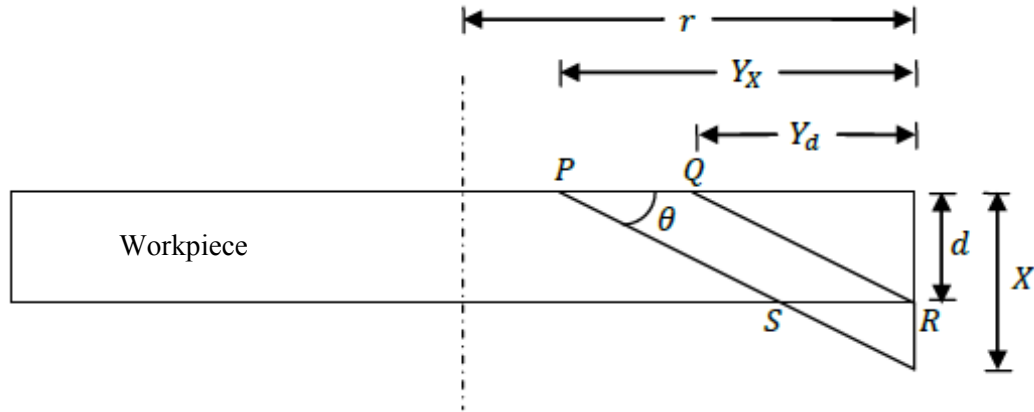


Figure 4.5 Front projection view of Stage II shear area

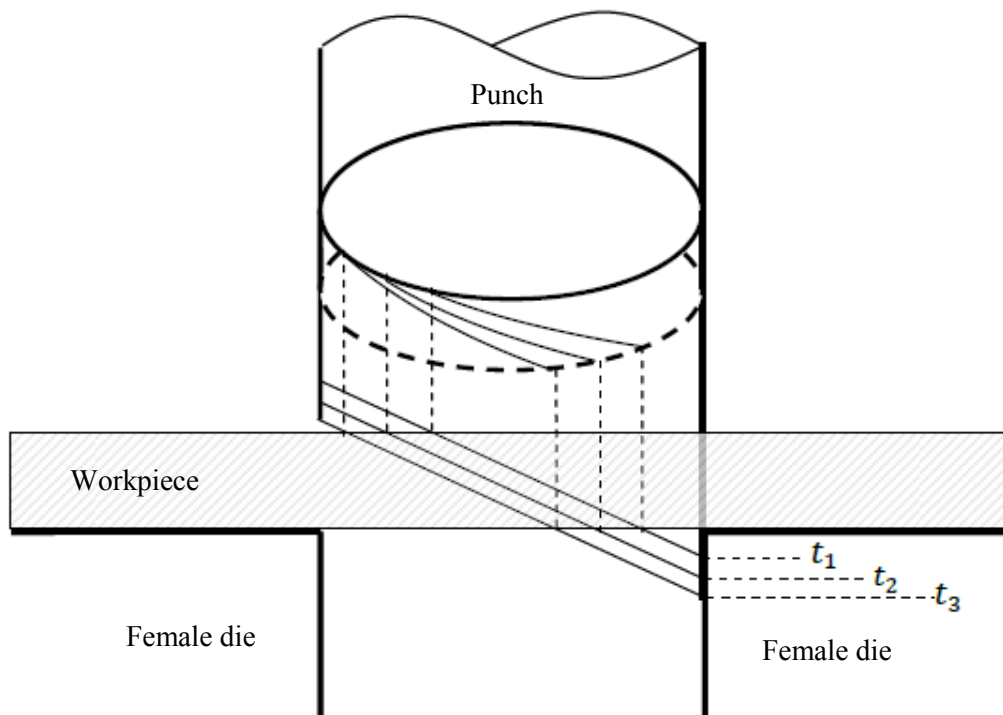


Figure 4.6 Isometric projection of Stage II shear area at three different time steps

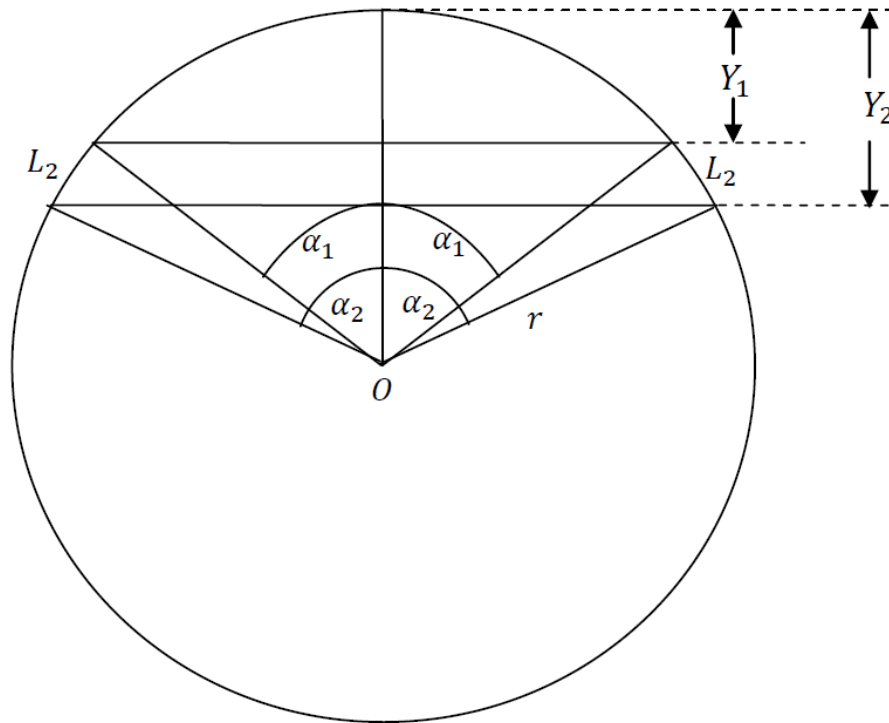


Figure 4.8 Top projection view of Stage II shear area

Considering that shear is occurring on both sides of the punch axis simultaneously during Stage II punching, an elemental perimeter length of $\frac{1}{2} \Delta l$ is defined, Figure 4.8. To determine the combined perimeter length, expressions for the distances Y_1 and Y_2 , as well as the angles α_1 and α_2 must be determined. According to the geometry in Figures 4.5, 4.6, and 4.8,

$$Y_1 = (d - h) \cot \theta \quad (4.34)$$

Similarly,

$$Y_2 = (X - h) \cot \theta \quad (4.35)$$

Now, the corresponding angles can be obtained as

$$\alpha_1 = \cos^{-1} \left[\frac{r - (d - h) \cot \theta}{r} \right] \quad (4.36)$$

$$\alpha_2 = \cos^{-1} \left[\frac{r - (X - h) \cot \theta}{r} \right] \quad (4.37)$$

Therefore, the elemental perimeter length during Stage II punching, L_2 (subscript “2” denotes Stage II shearing) can be written as

$$L_2 = r(\alpha_2 - \alpha_1) \quad (4.38)$$

Therefore, the elemental shear area corresponding to the sheared perimeter length can be written as

$$dA_2 = 2r(\alpha_2 - \alpha_1)(dh) \quad (4.39)$$

A factor of 2 is introduced to take into account both parallelograms on the front and the back side. Given Equation 4.39, the total area of the parallelogram shaped shear area can be obtained by integrating Equation 4.39 as follows

$$A_2 = \int_0^d 2r(\alpha_2 - \alpha_1)dh \quad (4.40)$$

and upon substitution of the values for α_1 and α_2 ,

$$A_2 = \int_0^d 2r \left[\cos^{-1} \left(\frac{r - (X - h) \cot \theta}{r} \right) - \cos^{-1} \left(\frac{r - (d - h) \cot \theta}{r} \right) \right] dh \quad (4.41)$$

After substitution of Equations 4.19 and 4.20 into Equation 4.41,

$$A_2 = \int_0^d 2r [\cos^{-1}(a + bh) - \cos^{-1}(1 - db + hb)] dh \quad (4.42)$$

Separating both terms on the right hand side of Equation 4.42

$$A_2 = \int_0^d 2r \cos^{-1}(a + bh) dh - \int_0^d 2r \cos^{-1}(1 - db + hb) dh \quad (4.43)$$

Since the second term has no X dependency, it is not integrated. Upon integrating the first term, A_2 can be obtained as

$$A_2 = \frac{2r}{b} \left[(a + bd) \cos^{-1}(a + bd) - \sqrt{1 - (a + bd)^2} - a \cos^{-1} a + \sqrt{1 - a^2} \right] \quad (4.44)$$

Upon variable substitution of $a = 1 - Xb$, Equation 4.44 can be rewritten as

$$\begin{aligned} A_2 = \frac{2r}{b} & \left[(1 + bd - Xb) \cos^{-1}(1 + bd - Xb) - \sqrt{1 - (1 + bd - Xb)^2} \right. \\ & \left. - (1 - Xb) \cos^{-1}(1 - Xb) + \sqrt{1 - (1 - Xb)^2} \right] \\ & - 2r \int_0^d \cos^{-1}(1 - db + hb) dh \end{aligned} \quad (4.45)$$

The time derivative of the last term of Equation 4.45 is zero as it is independent of X .

After taking the time derivative and simplifying the remaining term, the rate of shearing in Stage II can be written as

$$\frac{dA_2}{dt} = 2r [\cos^{-1}(1 - Xb) - \cos^{-1}(1 + bd - Xb)]v \quad (4.46)$$

4.2.3. Stage III

Due to symmetry, the time derivative of the shear area for Stage III is not calculated. Rather, Equation 4.33 for Stage I is transformed as follows to obtain the shear area rate in Stage III.

$$\frac{dA_3}{dt} = \left[2r \cos^{-1} \left(1 - \frac{X' \cot \theta}{r} \right) \right] v \quad (4.47)$$

Where

$$X' = 2r \tan \theta + d - X \quad (4.48)$$

4.3. Double Slanted Punch

Apart from the single slanted punch design, a symmetrical double slanted punch is of interest as it balances the shearing forces and thereby eliminates the bending moment on the punch. Figure 4.9 is a schematic used in the derivation of the punching force profile as a function of the rate of change of shear area..

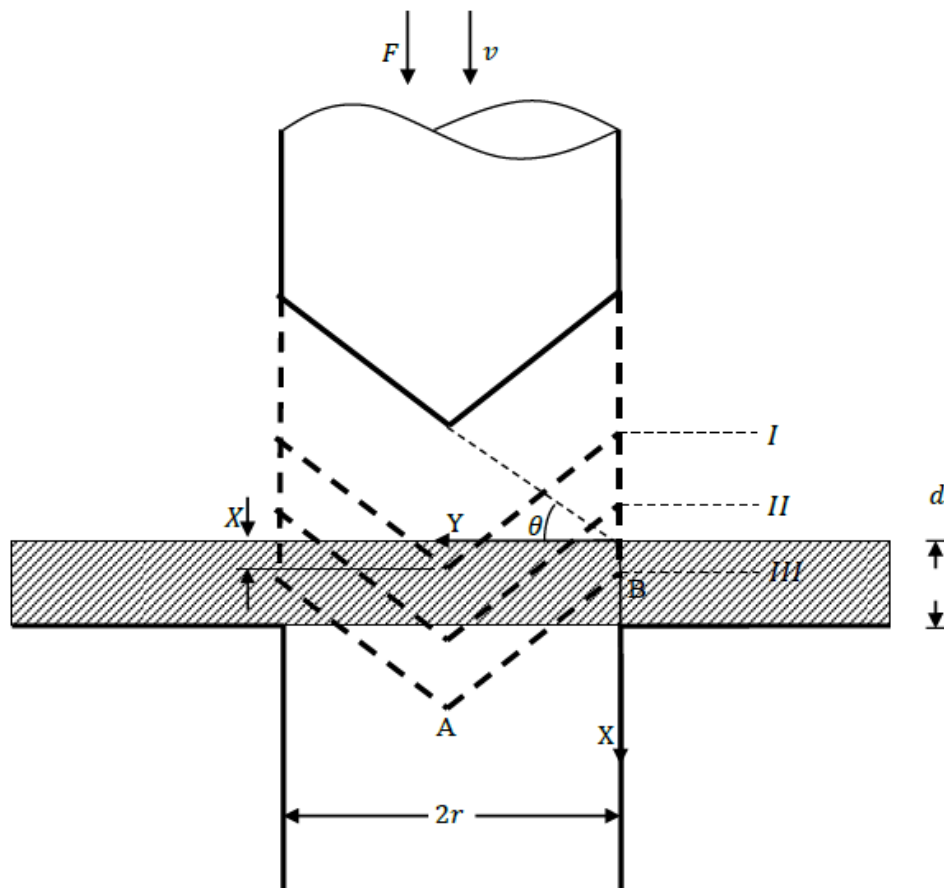


Figure 4.9 Three stages of punching with a wedge shaped punch

Similar to the derivation for a single slanted punch, there are three distinct stages of punch stroke length for the double slanted punch geometry..

- I. When the punch tip, Point A in Figure 4.9, has entered the material but has not yet protruded through the opposite side;

$$0 \leq X < d \quad (4.49)$$

- II. When the punch tip has exited the backside of the material but the trailing edge of the slanted face, Point B in Figure 4.9, has not yet entered the workpiece; and

$$d \leq X < r \tan \theta \quad (4.50)$$

- III. When point B has entered the workpiece, but has not yet protruded through the opposite side.

$$r \tan \theta \leq X \leq r \tan \theta + d \quad (4.51)$$

4.3.1. Stage I

The shearing area for Stage I is calculated by considering the integration of an elemental area, the details of which are given in Section 4.2.1.

$$A_1 = \int_0^x 4r \sin^{-1} \left(\frac{X-x}{r} \right) dx \quad (4.52)$$

Upon integrating and simplifying,

$$A_1 = 4r^2 \left[\left(\frac{X}{r} \right) \sin^{-1} \left(\frac{X}{r} \right) + \sqrt{1 + \left(\frac{X}{r} \right)^2} - 1 \right] \quad (4.53)$$

Therefore, the time derivative of the shearing area can now be calculated as

$$\frac{dA_1}{dt} = 4r \left[\sin^{-1} \left(\frac{X}{r} \right) + \left(\frac{X}{r} \right) \frac{1}{\sqrt{1 - \left(\frac{X}{r} \right)^2}} + \left(\frac{X}{r} \right) \frac{1}{\sqrt{1 + \left(\frac{X}{r} \right)^2}} \right] v \quad (4.54)$$

Putting $\frac{X}{r}$ as a nondimensional parameter ρ , Equation 4.54 can be simplified and rewritten as

$$\frac{dA_1}{dt} = 4r \left[\sin^{-1} \rho + \frac{\rho}{\sqrt{1-\rho^2}} + \frac{\rho}{\sqrt{1+\rho^2}} \right] v \quad (4.55)$$

4.3.2. Stage II

The development of the shear area for Stage II is similar to what is demonstrated in Section 4.2.2. Therefore, only the result of time derivative of shearing area is presented here.

$$\begin{aligned} \frac{dA_2}{dt} = 4r & [\cos^{-1}\{1 - (r \tan \theta + X)b\} \\ & - \cos^{-1}\{1 + bd - (r \tan \theta + X)b\} - (r \tan \theta + X)b]v \end{aligned} \quad (4.56)$$

where

$$b = \frac{\cot \theta}{r} \quad (4.57)$$

4.3.3. Stage III

Analogous to the expression of the shear area rate explained in Section 4.2.3, the time derivative for Stage III can be written as

$$\frac{dA_3}{dt} = 4r [\cos^{-1}\{1 - (r \tan \theta + d - X)b\}]v \quad (4.58)$$

4.4. Results

Simulations were performed using DEFORM 3D for micropunching with a single slanted punch face. The workpiece material is copper as chosen from DEFORM material library. This particular material is chosen to capture both strain and strain rate dependency of the flow stress with a Johnson and Cook material model. The actual

parameter values of the material model are irrelevant here as the purpose is not to determine the absolute punching force, but rather to determine the shape of the force profile with respect to punch stroke.

Five different slant angles are simulated: 0, 10, 20, 30, and 45 degrees. The resultant force profiles are non-dimensionalized by dividing all results by the maximum force for the simulation of a flat punch i.e. the slant angle equals 0 degree. Similarly, the rate of change of shear area is analytically determined for all five slant angles. In a similar manner to the simulated cases, the shear area rate profiles are also non-dimensionalized by dividing all results by the maximum rate of change of shear area for the simulation of a flat punch.

The non-dimensional force profiles obtained from simulation, and the non-dimensional shear area rates obtained from the analytical model for all five slant angles are plotted for comparison, Figure 4.10 to 4.14. In the figures, the dashed line represents the analytical model, with the solid line represents the FE simulation.

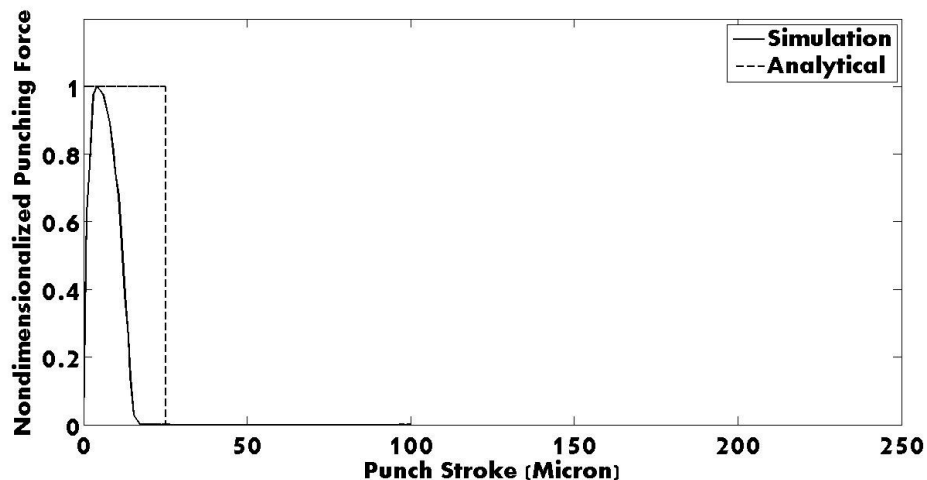


Figure 4.10 Comparison of the analytical (dashed line) and simulated (solid line) nondimensionalized punching force profile for a 0 degree single slant angle

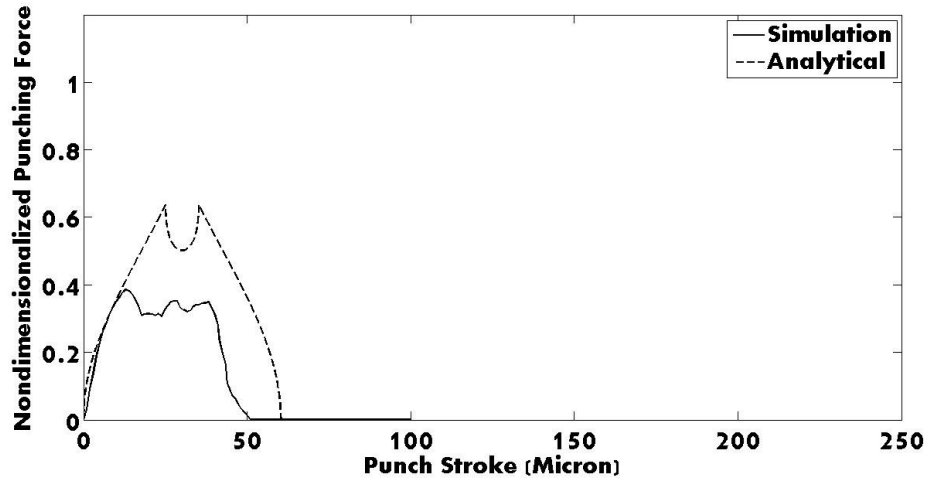


Figure 4.11 Comparison of the analytical (dashed line) and simulated (solid line) nondimensionalized punching force profile for a 10 degree single slant angle

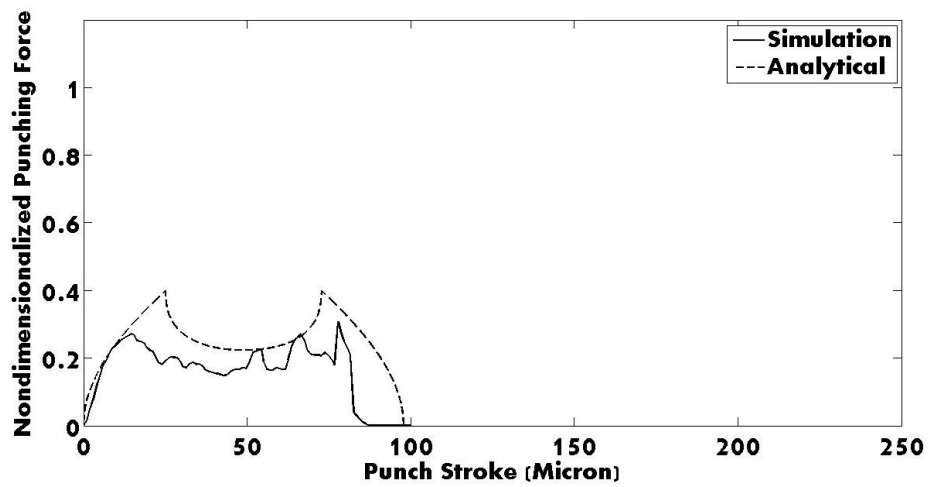


Figure 4.12 Comparison of the analytical (dashed line) and simulated (solid line) nondimensionalized punching force profile for a 20 degree single slant angle

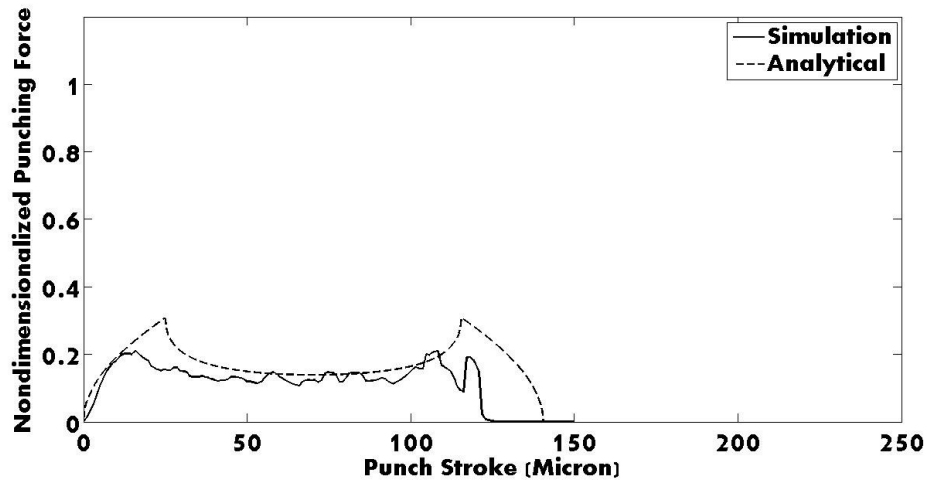


Figure 4.13 Comparison of the analytical (dashed line) and simulated (solid line) nondimensionalized punching force profile for a single 30 degree slant angle

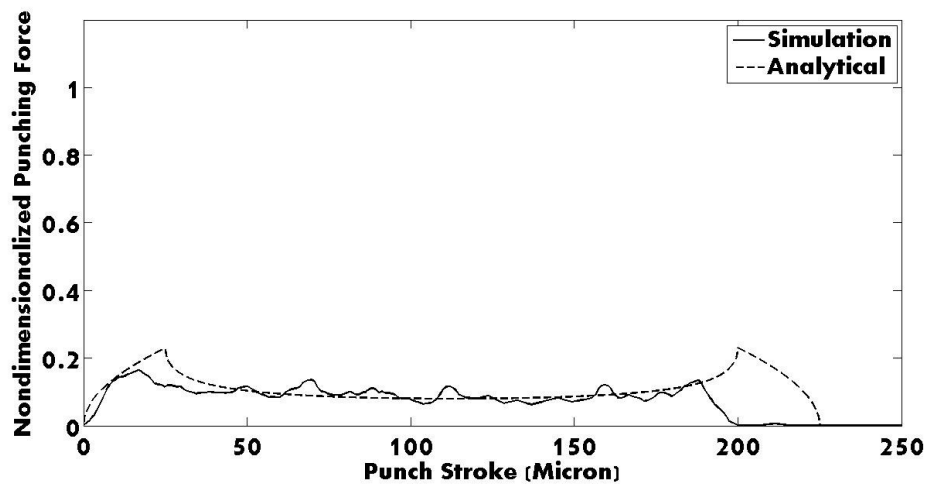


Figure 4.14 Comparison of the analytical (dashed line) and simulated (solid line) nondimensionalized punching force profile for a single 45 degree slant angle

To further investigate the association between the punching force profile and the rate of change of shear area, non-dimensional peak punching forces, as well as the non-dimensional peak shear area rates, are plotted for all five cases, Figure 4.15.

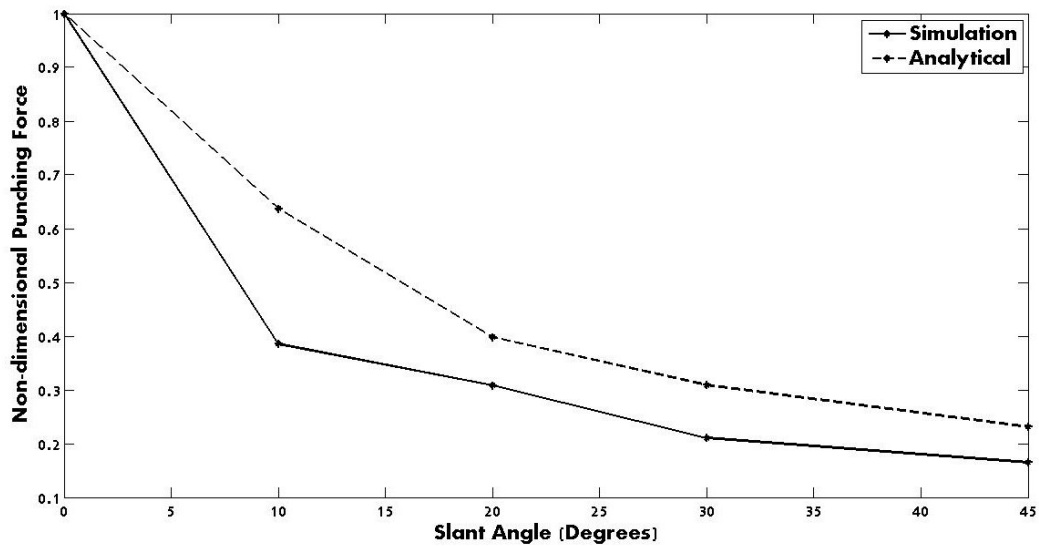


Figure 4.15 Comparison between nondimensional peak punching force (FE simulation – solid line) and nondimensional peak shear area rate (analytical model – dashed line) for each of the five single slant angles (0, 10, 20, 30, and 45 degrees)

4.5. Conclusion

- i. An analytical model was developed to calculate the rate of change of workpiece shear area for single and symmetrical slanted punch faces.
- ii. In the case of a single slanted punch face, evidence was presented for the dependency of instantaneous punching force on instantaneous shear area rate of the work piece material.
- iii. The reduction in peak punching force, with an increase in slant angle for a single slanted punch face, correlated well with the analytically predicted reduction of shear area rate.

Chapter 5

Material Modeling of Polycaprolactone

5.1. Introduction

Polycaprolactone (PCL) is a semi-crystalline, thermoplastic polymer widely used in the biomedical industry due to a desirable combination of biocompatibility and biodegradability. PCL belongs to the polyester family of organic compounds. ϵ -caprolactone is the parent compound, which undergoes ring opening polymerization, leading to PCL in the presence of heat and a catalyst, Figure 5.1.

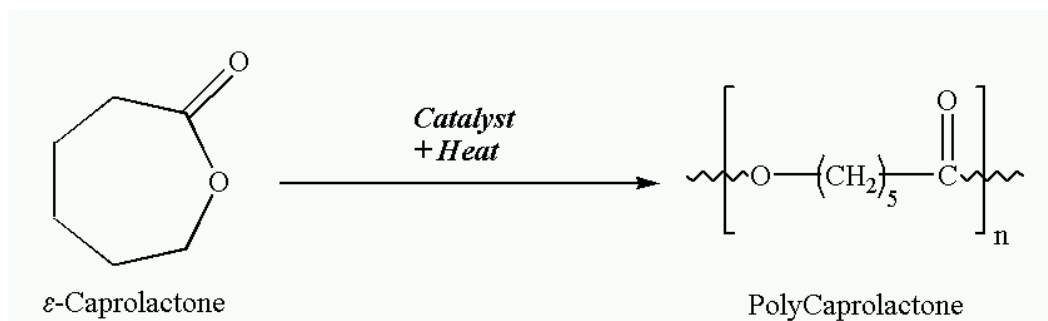


Figure 5.1 Ring opening polymerization for Polycaprolactone. Figure courtesy: [94]

The ester linkages in PCL can be degraded through hydrolysis, which is initiated by physiological conditions within the human body. Therefore, this material has gained in popularity for implants, particularly for longer term implantable devices due to a lower

degradation rate as compared to polylactides [94]. The Food and Drug Administration has approved PCL for specific uses in the human body, mostly as a drug delivery device.

In the last decade, PCL has gained popularity in the tissue engineering community as a suitable material for scaffolds [94]. Therefore, researchers have invested time in characterizing the stress-strain behavior. Historical results were previously summarized in Table 2.3 as part of the literature survey.

The research here focuses on producing porous membranes from PCL films, which are to be further stacked to make multilayer tissue scaffolds. A micro-punching process is proposed to fabricate individual 2D porous membranes. The guiding theme is to produce a scaffold that has two types of porosity: (i) holes of sufficient size and shape to act as home sites for cell seeding and growth, and (ii) holes and channels that form a microvasculature when the 2D layers are stacked into a 3D construct. The vasculature is required to provide nutrients and to discard waste as the cells develop into a functional tissue.

Both circular and non-circular holes can be punched with silicon dies, which can be fabricated using conventional micro-fabrication methods, such as deep reactive ion etching [4]. Since silicon is relatively brittle, an estimate of the punching force is vital for the punch and die design. The punching forces can be predicted using conventional finite element simulations; however, an accurate material model of the workpiece material is necessary as the constitutive relationship for PCL is not found in the material library of commercial FE codes.

A pilot study has shown that micro-scale holes cannot be punched in PCL at room temperature. The fracture strain of PCL at room temperature is too high to facilitate shearing within the die set clearance zone. Rather, PCL exhibits hyper plastic behavior,

stretching excessively to form a bag like structure around the punch, Figure 5.2, or if shearing does occur it is only a partial tear, resulting in a tentacle of PCL that prevents full separation of the punched out material.

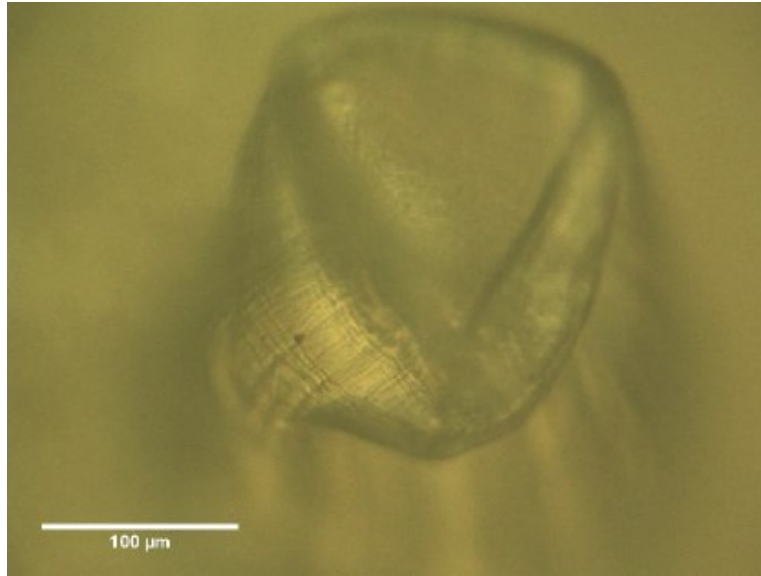


Figure 5.2 PCL punching at room temperature resulting in a bag like structure

To improve the punching (shearing) characteristics of PCL, liquid nitrogen is used to cool the material below its glass transition temperature, which is $-60\text{ }^{\circ}\text{C}$ [94]. Cooling invokes a brittle material response as the polymer chains are prevented from stretching and gliding past one another during the high deformation punching process [95].

Although material properties of PCL are available in the literature at room temperature, there is no information at temperatures below the glass transition, particularly in boiling liquid nitrogen at $-196\text{ }^{\circ}\text{C}$, which is the operating temperature in the current research. This chapter focuses on the experimental techniques used to determine the constitutive relationship for PCL at both room temperature and

when cooled with liquid nitrogen. The material model is then used in the finite element package DEFORM 3D to estimate micropunching forces.

5.2. Materials and Methods

Uniaxial compression testing is performed to obtain the true stress-strain behavior of PCL. The detailed procedure for uniaxial compression testing of polymers is given by Jerabek et al. for Polypropylene [96], which closely follows the procedure given by ASTM for compression testing of plastics [97].

5.2.1. Sample Preparation

Polycaprolactone pellets, with an average length and diameter of 3 mm, were purchased from Sigma Aldrich (Part No. 440744, Saint Louis, MO). According to the manufacturer, the molecular weight of the polymer varies from 70,000 to 90,000, with a polydispersity index of 2. The average pellet density is noted as 1.145 g/mL at room temperature, with less than 1 % water impurity.

Following ASTM Standard D695-10 (Compressive properties of rigid plastics) sample specimens are prepared by injection molding. For this research, a custom injection mold is designed to fabricate the PCL specimens. Since PCL is a thermoplastic, it regains its bulk material properties after the molded component is cooled.

A CAD model of the injection mold is shown in Figure 5.3. The injection mold assembly consists of five components: (A) bottom plate, (B) specimen die, (C) top plate, (D) T-bolt, and (E) 1 inch hex head screw. A thermocouple is connected to the top plate to monitor temperature, which is assumed to be close to the temperature of the molten PCL as they are in direct contact.

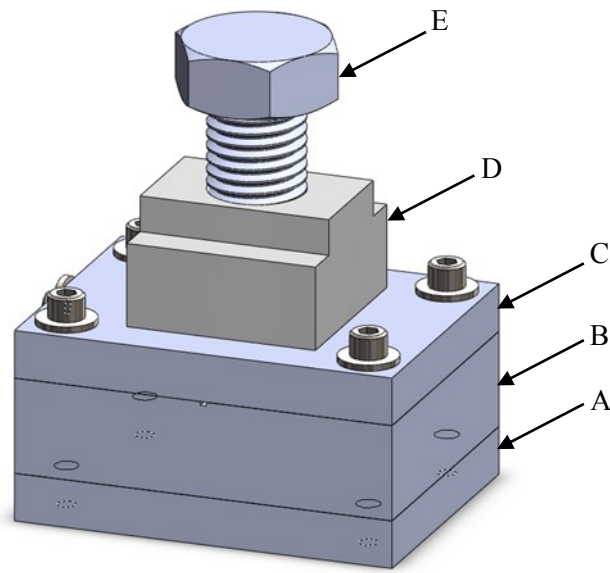


Figure 5.3 CAD model of the injection mold used to fabricate a PCL test specimen for compression testing

To create an injection molded PCL specimen, the bottom plate, specimen die, top plate, and the T-bolt are first rigidly fixed together. Then, the T bolt is partially filled with PCL pellets. The bolt is closed from the top by hand tightening the 1 inch hex head screw. Afterward, the completed assembly is placed on a hot plate, Figure 5.4.

Once the thermocouple temperature indicates the assembly has reached 160 degrees Celsius, it is quickly moved from the hot plate to a vice, where the bottom plate is fixed to the assembly. Finally, the 1 inch hex head screw is tightened using a spanner wrench until molten PCL is observed in the relief grooves, indicating successful filling of the specimen die cavity.

After molding the specimen, the assembly is left to cool to room temperature, after which the unfinished specimen is removed from the die. The specimen is then

trimmed and cut into smaller lengths, which are close to the final desired length required for compression testing.

The finished length is obtained by fixing the rough cut specimen into a holder and then hand sanding and polishing while maintaining the specimen ends perpendicular to the cylindrical axis. By this method, samples with two different aspect ratios were fabricated. Throughout this chapter, aspect ratio refers to the ratio of sample length to sample diameter.

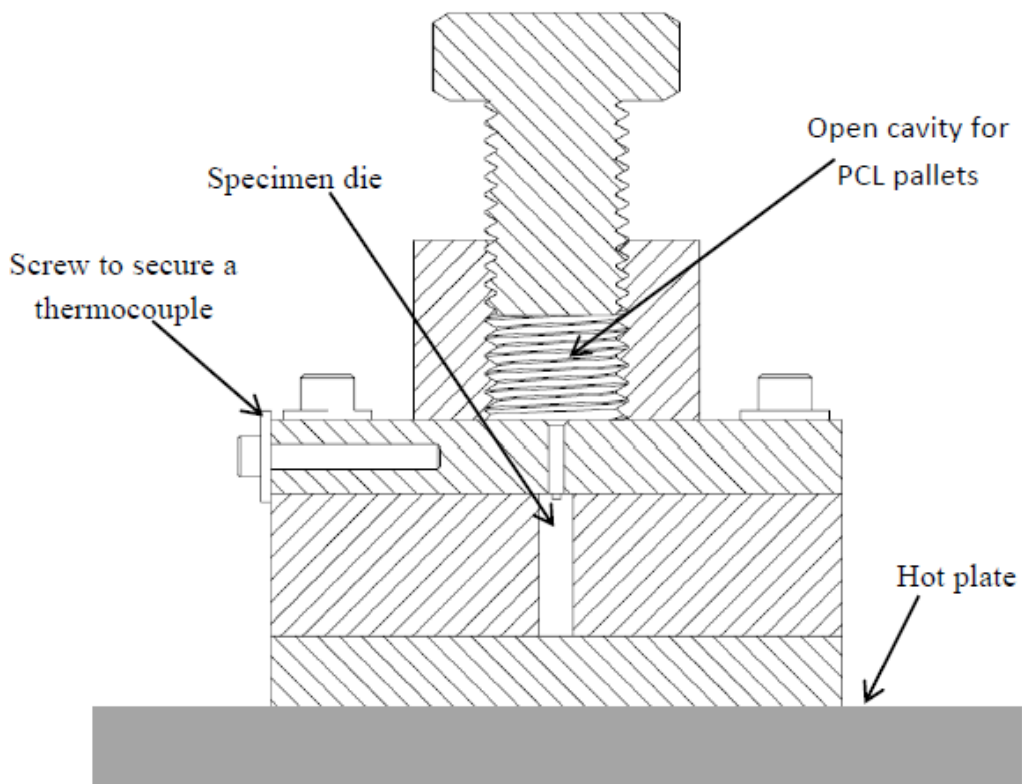


Figure 5.4 Midsection view of the injection mold used to fabricate PCL specimens for compression testing

Compression testing of PCL was conducted at two temperatures: (1) room temperature, and (2) below the glass transition temperature with the specimen fully

immersed in a bath of liquid nitrogen. The room temperature tests are carried out on specimens of a fixed aspect ratio. The goal of the room temperature tests is to validate the setup and procedure by comparing the results to information available in the literature. The compression tests of PCL in liquid nitrogen are carried out for two different aspect ratios.

5.2.2. Experimental Setup

A Universal Tensile Test machine (Instron - Series 3360, Norwood, MA) is used for the compression test of PCL. A custom designed fixture is fabricated to accommodate liquid nitrogen for tests where the sample is below the glass transition temperature. The same fixture is used for tests at room temperature with the liquid nitrogen reservoir left empty. A force sensor of 10 kN capacity is used for all tests. Figure 5.5 and Figure 5.6 show the isometric CAD design and cross-sectional view of the fixture, respectively.

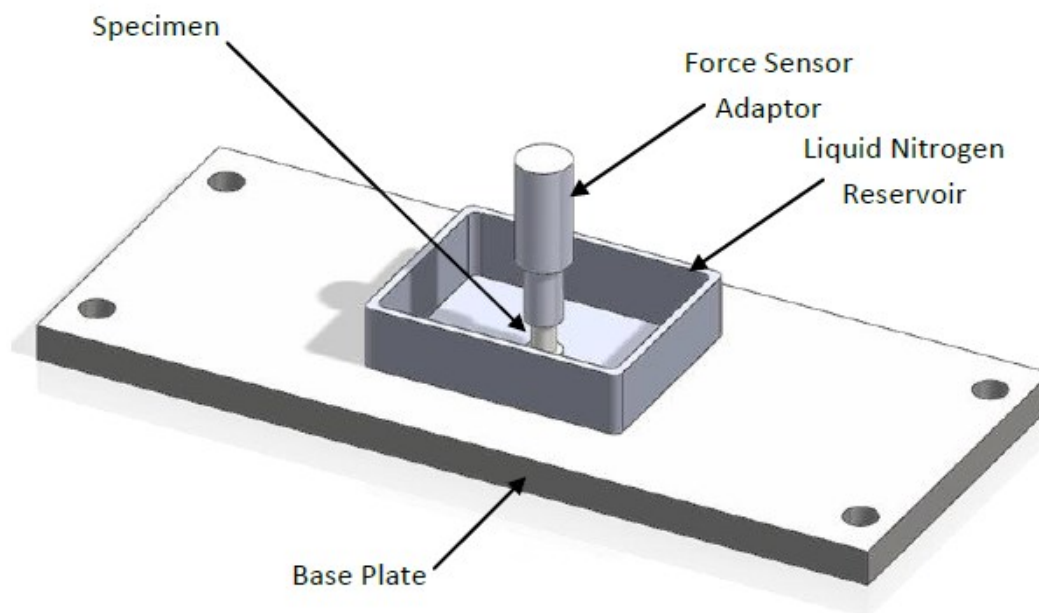


Figure 5.5 CAD model of the compression test fixture showing the liquid nitrogen reservoir

The ASTM standard for compression testing of rigid plastics recommends using a ball-aligned compression tool for most plastics [97]. However, this may not be necessary for plastics with a low modulus (below 3500 MPa). The elastic modulus of PCL at room temperature is expected to be very low i.e. on the order of a few hundred MPa, but below the glass transition temperature, the modulus is expected to increase tenfold, which is close to the upper limit for using a compression tool. Therefore, to keep the tests consistent with respect to ASTM recommendations, a custom ball-aligned compression tool is fabricated and used for all tests, including the tests at room temperature, Figure 5.6.

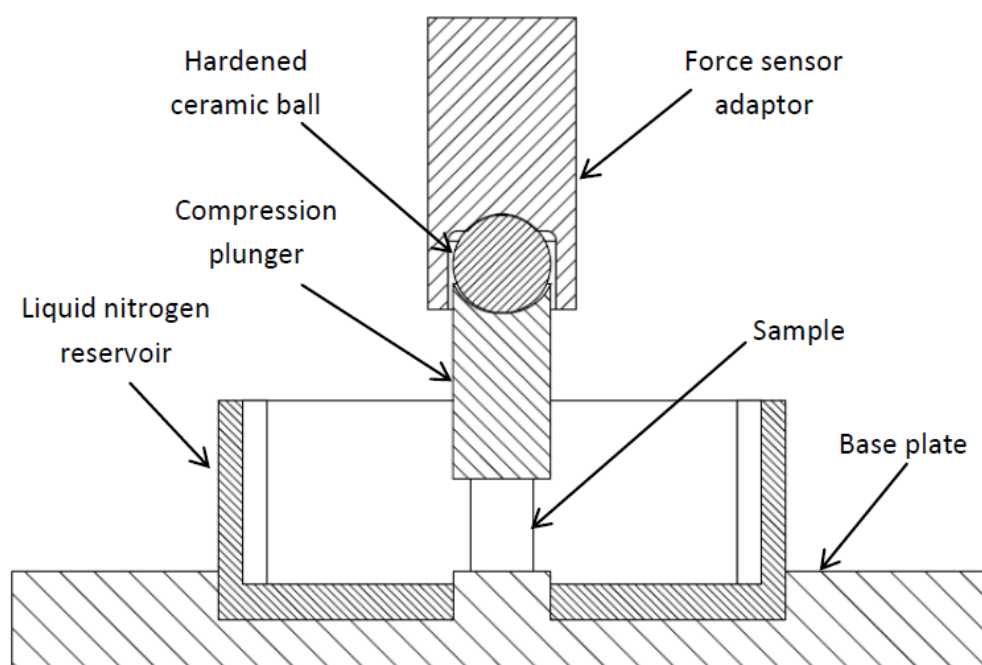


Figure 5.6 Cross sectional view of the compression test setup

The base plate, compression plunger, and force sensor adaptor are constructed from steel. As the modulus and strength of steel are orders of magnitude greater than those of PCL, the compliance of the fixture is assumed to have a negligible effect on the

results. The liquid nitrogen reservoir is made from polypropylene, which acts like a thermal insulator and reduces direct contact area between the base plate and the liquid nitrogen. The hardened ceramic ball serves two purposes: (1) it helps to align the compression tool, and (2) it thermally insulates the force sensor adaptor from the compression plunger, which is in direct contact with liquid nitrogen. The base plate is rigidly fixed to the base of the tensile test machine. The liquid nitrogen reservoir is press fit with the base plate. Vacuum grease is applied between the base plate and the reservoir to avoid any liquid nitrogen leakage. The compression plunger, ceramic ball and force sensor adaptor are put together with some vacuum grease on the ceramic ball. The vacuum grease helps to keep all three parts together without using a rigid fastener. The force sensor adaptor is rigidly fixed with the force sensor, which in turn is fixed to the moving head of the tensile test machine.

5.2.3. Procedure

The polished PCL specimens are numbered and their diameters and lengths are measured using a micrometer. The dimensions are measured at three locations on each specimen and the average value of length and diameter is used for calculation of the aspect ratio. The variation in measurement of diameter and length of the specimens was determined to be negligible. The specimen dimensions are summarized in Table 5.1.

Table 5.1 Specimen dimensions for different aspect ratios

Length (mm)	Diameter (mm)	Aspect ratio (l/d)
12	8	1.5
8	8	1.0

After taking measurements, the specimen is placed at the center of the base plate on a circular post. The head of the tensile test machine, along with the compression tool,

is then moved manually to bring the surface of the compression plunger close to the top surface of the specimen without making contact. The load indicator and the displacement indicator on the software graphical user interface are balanced at this point so that both sensors read zero. The test program now runs and completes the compression test automatically with very little user engagement. The compression program has three phases:

- I. Constant speed with displacement control
- II. Constant preload of 10 N with force control
- III. Constant speed with displacement control

During Phase I of the test, the compression head moves freely with constant speed (1.0 mm/min) before touching the specimen's top surface. At the end of Phase I, after touching the top surface of the specimen, the program senses the compressive load and when it becomes 10 N, switches to Phase II where the load is maintained at 10 N for 300 seconds. The 300 second dwell time is included in the program to accommodate adding liquid nitrogen to the reservoir and to allow time for the temperature of the specimen and surrounding materials to be saturated. During this time, some boiling of liquid nitrogen occurs, but the reservoir is replenished by hand pouring until an equilibrium temperature is reached. Upon contact with liquid nitrogen, the PCL specimen immediately cools and shrinks in both the radial and axial (length) directions. The force sensor detects the reduction in sample length due to a decrease in the compressive load. This causes the program to reengage movement of the crosshead to maintain 10 N of preload. This keeps the specimen situated in place during boiling of the liquid nitrogen and also the recorded value of head movement during Phase II helps correct for any error occurring from the change in specimen length due to cooling.

For the compression tests at room temperature, the dwell time in Phase II is not utilized. At the end of the 300 seconds, the program automatically switches to Phase III. Phase III is the actual compression phase where the machine's crosshead moves with a constant speed until it reaches an end criterion. There are two end criteria set for all specimens. Either the displacement reached is 4.0 mm or the compressive load reaches 10 kN, which is the maximum capacity of the load sensor.

ASTM D695-10 recommends a crosshead speed between 1.0 mm/min to 1.6 mm/min during compression tests for recommended specimen lengths of 50 mm. This results in a strain rate of approximately 0.02 min^{-1} . However, since specimens with different aspect ratios (different lengths) are used in this study, the crosshead speed is adjusted to maintain the ASTM recommended strain rate of 0.02 min^{-1} . After meeting one of the end test criteria, the compression test is automatically stopped and the data is recorded in a MS Excel file, which in turn is processed using Matlab.

5.2.4. Calculation of Compressive True Stress and True Strain

Let the length of the polished PCL specimens be L , which is assumed to be unaltered after a preload of 10 N. Let L_{LN} be the length of the specimen at the end of Phase II after the specimen reaches thermal equilibrium with boiling liquid nitrogen. Assuming a linear coefficient of thermal expansion, one can write

$$L_{LN} = L(1 - \alpha\Delta T) \quad (5.1)$$

where α is the coefficient of thermal expansion and ΔT is the decrease in temperature. Now, the final length of the specimen can be written as the initial length multiplied by some scaling factor. The scaling factor can be written as

$$k = (1 - \alpha\Delta T) = \frac{L_{LN}}{L} \quad (5.2)$$

Similarly, the final diameter of the sample D_{LN} can be written as

$$D_{LN} = kD \quad (5.3)$$

Substituting k from Equation 5.2 into Equation 5.3,

$$D_{LN} = D(1 - \alpha\Delta T) = D \left(\frac{L_{LN}}{L} \right) \quad (5.4)$$

where D is the diameter of the polished specimen at room temperature. For compression tests at room temperature,

$$L_{LN} = L \quad (5.5)$$

$$D_{LN} = D \quad (5.6)$$

Let F be the load shown by the force sensor at any instant during the compression test and ΔL (< 0 for compression in this case) is the displacement of the compression head from the beginning of Phase III.

The engineering stress can be written as the applied compressive force divided by the original cross sectional area,

$$\sigma_e = \frac{4F}{\pi D_{LN}^2} \quad (5.7)$$

and the engineering strain can be written as the change in length divided by the original length,

$$\varepsilon_e = \frac{\Delta L}{L_{LN}} \quad (5.8)$$

Engineering stress-strain is plotted and analyzed for calculating Young's modulus, Yield Strength, and Strain at Yield. Figure 5.7 shows a typical stress strain curve for a rigid plastic.

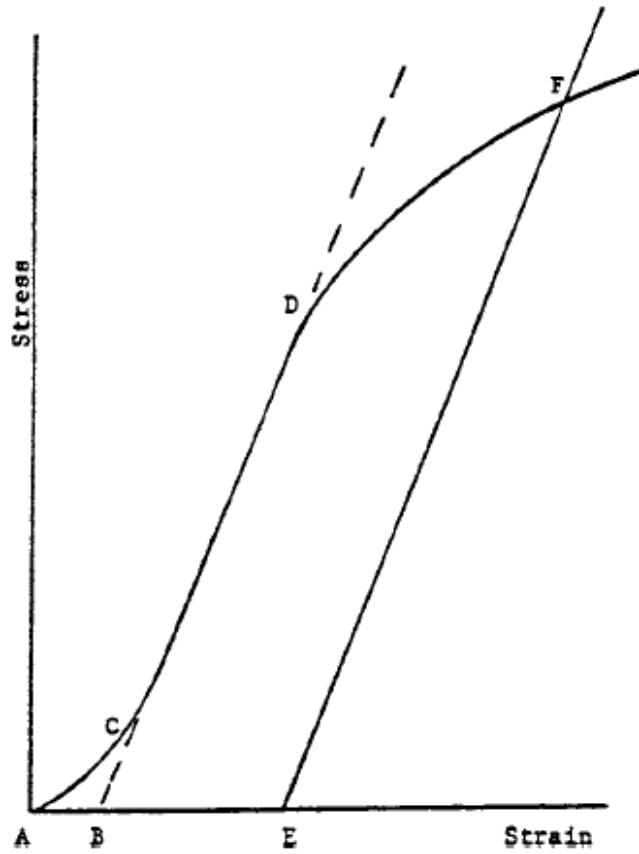


Figure 5.7 Typical stress-strain curve for a rigid plastic. Figure courtesy: [97]

The toe region, indicated by line segment AC in Figure 5.7, does not provide useful material property information, rather it is an artifact caused by slack, misalignment, or seating of the specimen. Therefore, Young's modulus is obtained by calculating the slope of the linear zone, line segment CD . The error due to the toe region is corrected by creating a hypothetical zero at point B , which is obtained by extending the linear region CD and intersecting it with the strain axis. All strain and yield offset values are measured from the new corrected zero at point B . Figure 5.7 also shows an offset strain at point E for obtaining the Yield Strength. A 0.2 % offset strain is used to calculate the Yield Strength in the current study. Any deformation beyond the Yield point is considered a combination of elastic and plastic deformation.

In order to perform finite element simulations with large deformation and fracture, a true stress and true strain curve is necessary, particularly for the plastic deformation zone. In the current study, the plastic deformation zone is explicitly determined by isolating it from the total stress-strain curve. First, the true stress and true strain values are obtained from the engineering stress and strain values. Unlike a uniaxial tensile test, the calculations for true stress and true strain from a uniaxial compression test are not trivial when it comes to sign conventions. The following two equations are used to calculate true stress and true strain (subscript “t”) from engineering stress and engineering strain (subscript “e”).

$$\sigma_t = \sigma_e(1 - \varepsilon_e) \quad (5.9)$$

$$\varepsilon_t = -\ln(1 - \varepsilon_e) \quad (5.10)$$

Equations 5.9 and 5.10 are similar to the equations given in ASTM E646-07. However, they are slightly altered in order to keep the engineering strain and true strain values in a positive sense. The true yield stress $\sigma_{t,Y}$ and true yield strain $\varepsilon_{t,Y}$ values corresponding to the engineering yield strength and engineering strain to yield for each specimen is obtained. All data points beyond the yield point are then translated to the origin by subtracting $\sigma_{t,Y}$ from the true stress values and $\varepsilon_{t,Y}$ from the true strain values. The translated values of true stress and true strain values are then processed to fit a strain hardening model.

For compression tests at room temperature, only the engineering stress-engineering strain curve is plotted as these data are only used for validation of the fixture and not for finite element modeling of the micropunching process. For tests below the glass transition temperature of PCL, the true stress – true strain curves are obtained for two different aspect ratios (1.0 and 1.5) and then, extrapolated for a reciprocal of aspect

ratio i.e. d/l ratio of zero to obtain the effective theoretical true stress – true strain curve to be used in finite element modeling [96].

5.3. Results

Engineering stress and engineering strain, resulting from compression tests of five PCL samples of aspect ratio 1.5. at room temperature, is plotted in Figure 5.8.

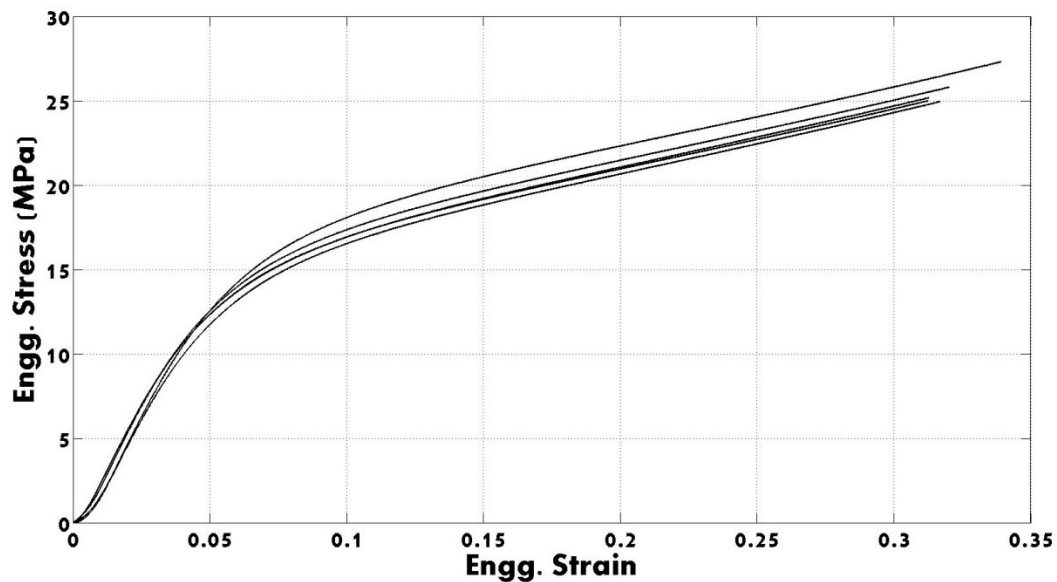


Figure 5.8 Engineering stress-strain curve for PCL compression testing at room temperature

Note that the toe region of the stress-strain curve is not corrected as raw data is shown in Figure 5.8. However, the zero of the strain axis needs to be corrected for calculation of the Yield Strength as recommended by ASTM D695-10. Figure 5.9 to Figure 5.12 show the raw engineering stress-strain data for a typical specimen, finding the linear region, correcting for the zero point, and finding a 0.2 % yield offset point, respectively.

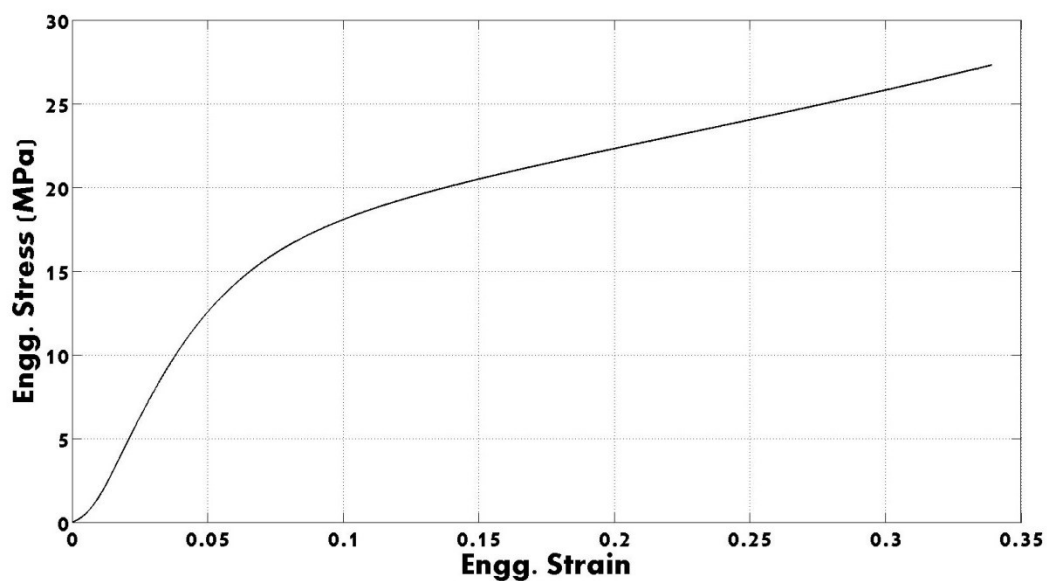


Figure 5.9 Raw engineering stress-strain curve for a typical PCL specimen tested in compression at room temperature

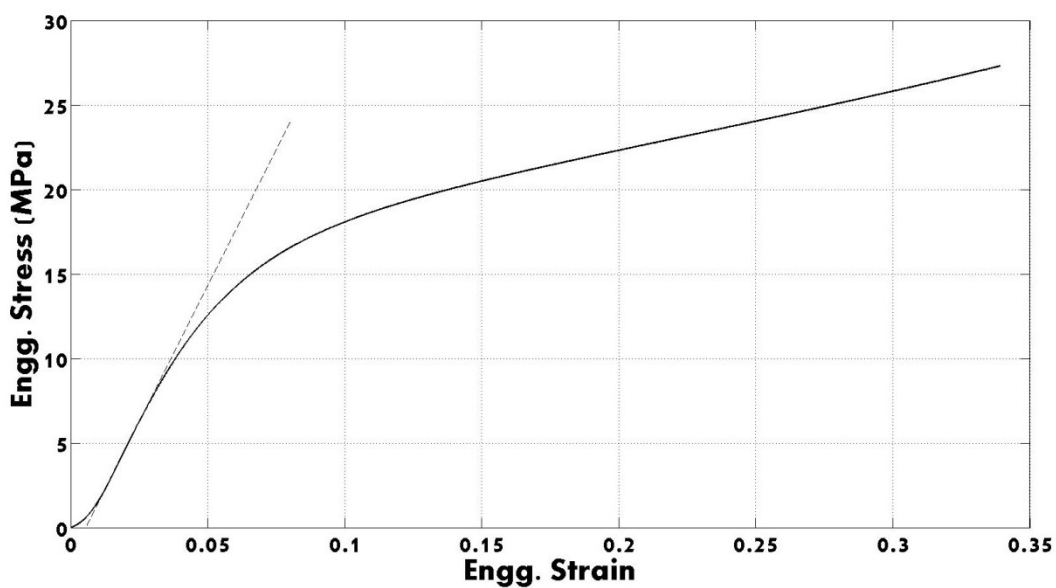


Figure 5.10 Linear region of the raw engineering stress-strain curve for a typical PCL specimen tested in compression at room temperature

Similar steps are followed for all specimens to calculate Young's modulus, Yield Strength and Yield Strain. The results for material properties of PCL determined at room temperature are summarized in Table 5.2.

Table 5.2 Properties of PCL at room temperature based on compressive testing

Property	Mean	St. Dev.	C.V.
Young's Modulus	323 MPa	5.06 MPa	1.6 %
Yield Strength	9.2 MPa	0.67 MPa	7.3 %
Yield Strain	0.031	0.002	6.8 %

For compressive testing of specimens below the glass transition temperature i.e. in boiling liquid nitrogen, an additional step of correction is added to take into account shrinkage of specimens due to cooling.

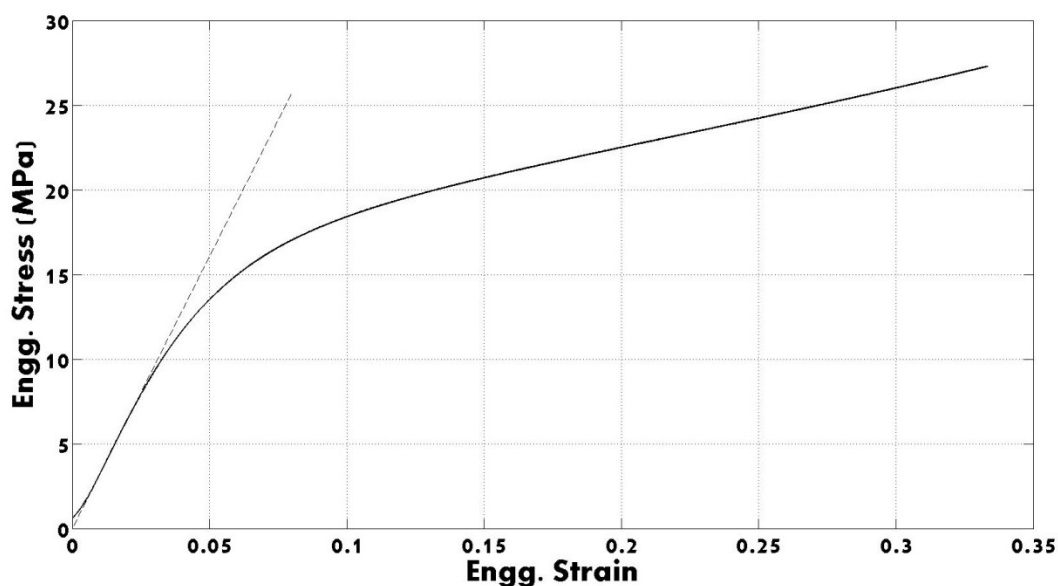


Figure 5.11 Zero corrected engineering stress-strain curve for a typical PCL specimen tested in compression at room temperature

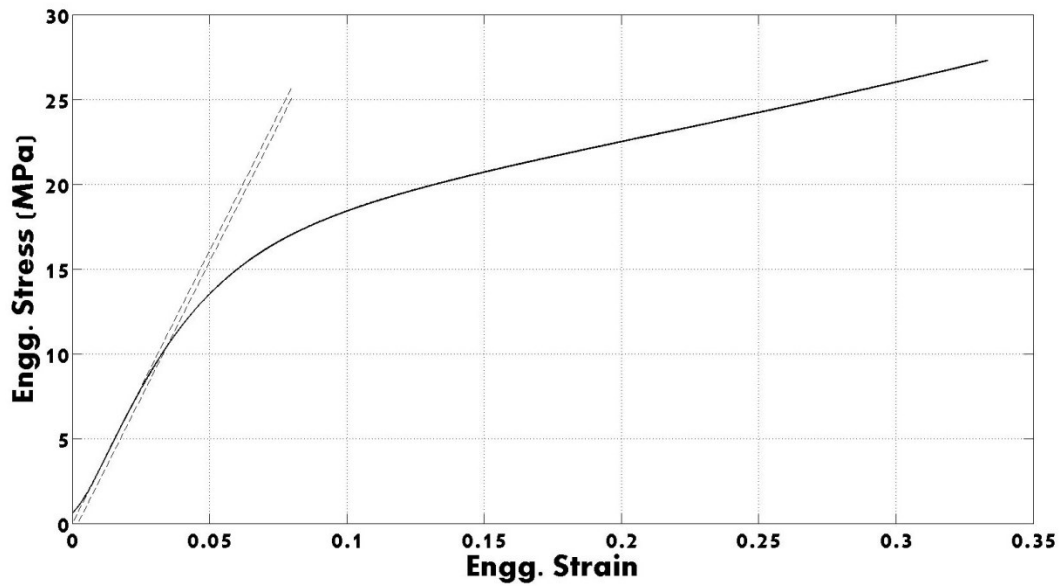


Figure 5.12 0.2 % offset Yield strength from the zero corrected engineering stress - strain data of a typical PCL specimen tested in compression at room temperature

The engineering stress – strain curve of PCL in liquid nitrogen is given in Figure 5.13 for a specimen aspect ratio (l/d) equal to 1.5.

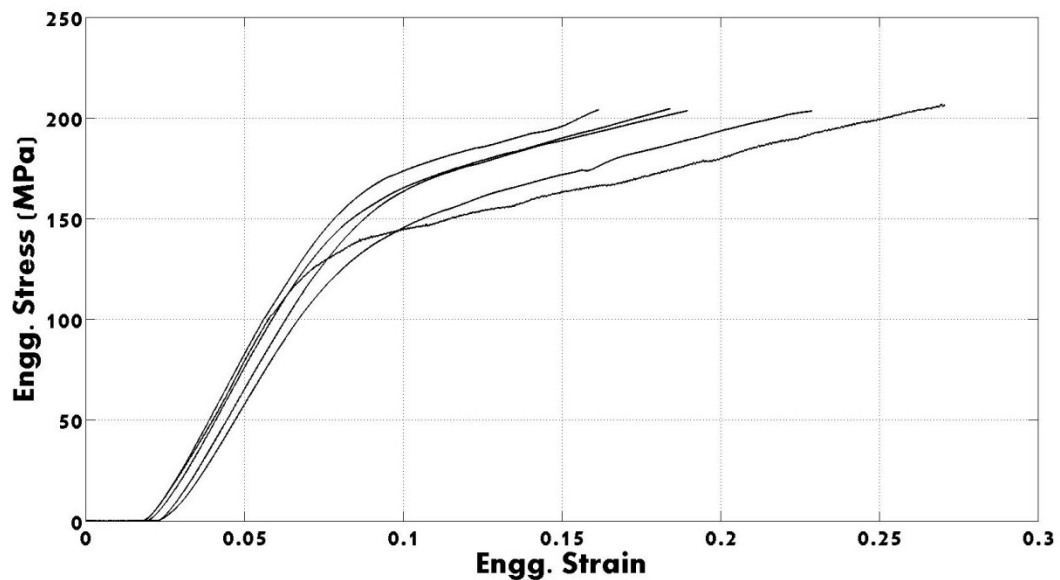


Figure 5.13 Engineering stress – strain curve of PCL samples submerged in liquid nitrogen during compression testing (aspect ratio = 1.5)

The material properties of PCL in liquid nitrogen are to be used in DEFORM for micro-punching simulation. DEFORM 3D v10.2.1 allows tabulated data for flow stress, which can be obtained through experiments like in the current study. However, an analytical form of the constitutive model will help other researchers use the properties of PCL in liquid nitrogen for finite element simulations. The most common constitutive equation used in DEFORM is Ludwik's equation which can be written as

$$\sigma_f = Y + K \varepsilon_p^n \quad (5.11)$$

where, σ_f is the flow stress, Y is the yield strength, K is the strength coefficient, and n is the strain hardening exponent.

The yield strength is obtained by following the steps recommended by ASTM D695-10, also explained for the room temperature tests. The procedure for calculating the strength coefficient and the strain hardening exponent given in ASTM E646-07 are cumbersome. Therefore, a computer program (Matlab curve fitting tool) is used to determine these values. First, the plastic deformation region beyond the yield point is isolated for each specimen. Then, the data is processed through the curve fitting tool to obtain the applicable power law. Finally, the parameters are obtained for each specimen and their average values are calculated. The flow stress with respect to true plastic strain is plotted in Figure 5.14 for an aspect ratio equal to 1.5.

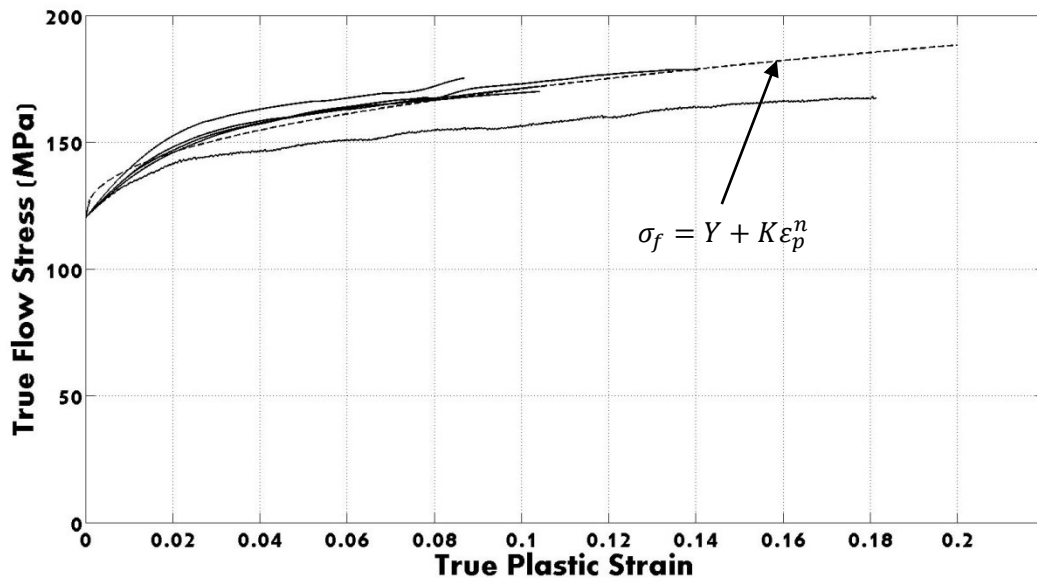


Figure 5.14 Experimental results and related Ludwik's equation for PCL flow stress. Data from compression testing while the specimen is submerged in liquid nitrogen (aspect ratio = 1.5).

Similarly, results for engineering stress – strain and flow stress for PCL in liquid nitrogen for aspect ratio of l/d equal to 1.0 are given in Figure 5.15 and Figure 5.16 respectively.

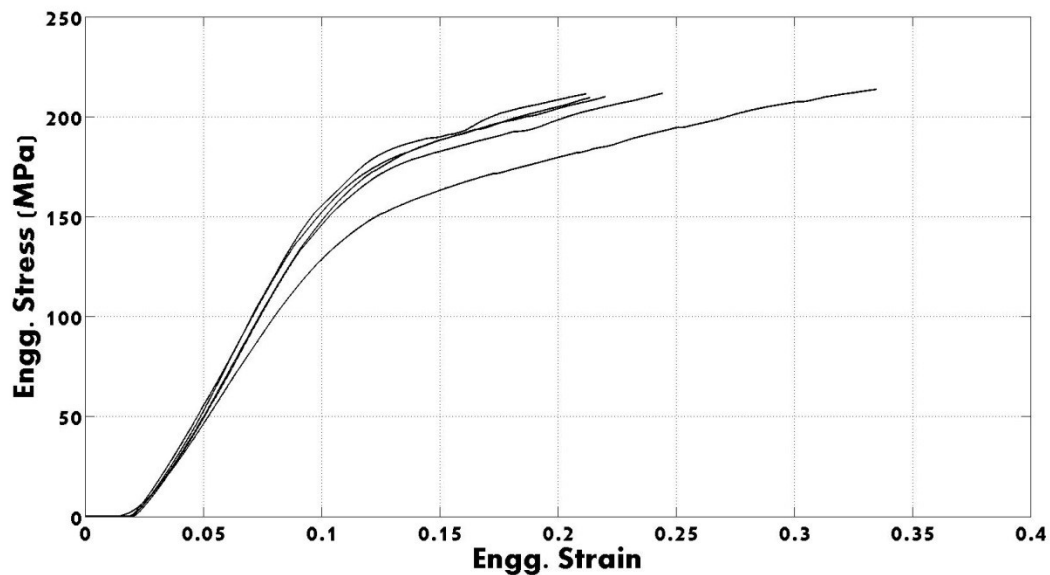


Figure 5.15 Engineering stress – strain curve of PCL in liquid nitrogen is given in Fig. 12 for specimen aspect ratio l/d equal to 1

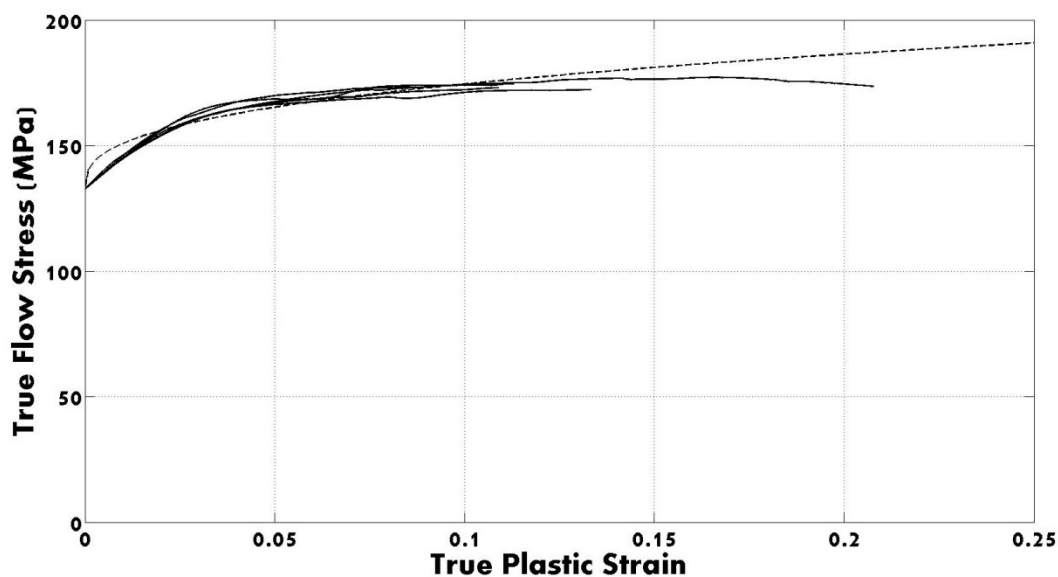


Figure 5.16 Flow stress of PCL in liquid nitrogen from Ludwik's equation for specimens of aspect ratio of l/d equal to 1

Results for material properties of PCL below its glass transition temperature i.e. in liquid nitrogen for an aspect ratio equal to 1.5 are summarized in Table 5.3.

Table 5.3 Properties of PCL from compression tests in liquid nitrogen ($l/d = 1.5$)

Property	Mean	St. Dev.	C.V.
Young's Modulus	2794 MPa	366 MPa	13.1 %
Yield Strength	120 MPa	8.6 MPa	7.1 %
Yield Strain	0.045	0.006	13.9 %
Strength Coefficient	134 MPa	23.1 MPa	17.2 %
Strain Hardening Exponent	0.4205	0.0152	3.6 %

Similarly, results for material properties of PCL below its glass transition temperature i.e. in liquid nitrogen for an aspect ratio equal to 1.0 are summarized in Table 5.4.

Table 5.4 Properties of PCL from compression tests in liquid nitrogen ($l/d = 1.0$)

Property	Mean	St. Dev.	C.V.
Young's Modulus	2112 MPa	152 MPa	7.2 %
Yield Strength	133 MPa	14.2 MPa	10.7 %
Yield Strain	0.065	0.005	7.8 %
Strength Coefficient	96.0 MPa	14.7 MPa	15.3 %
Strain Hardening Exponent	0.3605	0.0471	13.1 %

For large deformation finite element simulation in DEFORM 3D, only three parameters are needed for the material model while using Ludwik's equation for flow stress: (1) Yield Strength, (2) Strength Coefficient, and (3) Strain Hardening Exponent. As shown herein, these parameters are obtained experimentally for two aspect ratios. However, to use these parameters in a simulation, the effective theoretical values must be obtained by extrapolating the reciprocal of aspect ratio (d/l) equal to zero i.e. a sample of infinite length and a finite diameter.

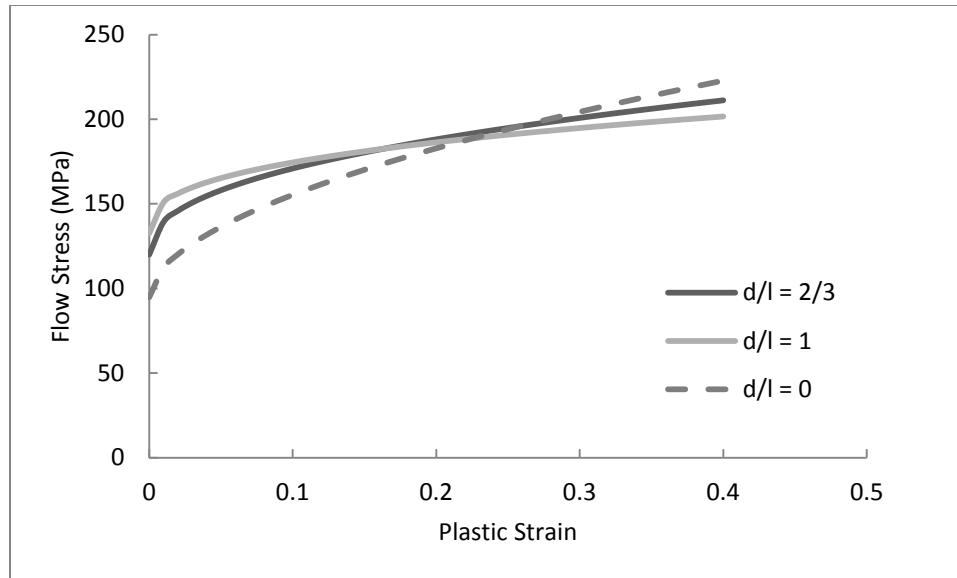


Figure 5.17 Experimentally determined flow stress curves for PCL (reciprocal aspect ratios equal to 1.0 and 2/3). The experimental data was extrapolated to generate a flow stress curve for PCL in compression (dashed line) for $d/l = 0$.

The extrapolated values of Yield Strength, Strength coefficient, and the Strain Hardening Exponent, for use in the FE simulation, are approximately 94.8 MPa, 210 MPa, and 0.5405, respectively. Similarly, the extrapolated value of Young's modulus is 4160 MPa. The experimentally determined flow stress for reciprocal aspect ratios (d/l) of 1 and 2/3, and the extrapolated value for d/l equal to zero, are plotted in Figure 5.17.

5.4. Discussion

The material properties of PCL at room temperature are obtained in order to validate the fixture and the test procedure. Young's modulus obtained experimentally is 323.3 +/- 9.2 MPa, which compares well with what was obtained by Eshragi et al. [21] i.e. 317.1 +/- 3.9 MPa. Also, the experimentally obtained Young's modulus matches well with what is reported by other researchers, which ranges from 251.9 MPa to 430 MPa as provided previously in Table 2.3. Similarly, the compressive Yield Strength reported by

Eshragi et al. is 10.3 +/- 0.2 MPa, which is close to the experimentally obtained Yield Strength of 9.2 +/- 0.7 MPa. The Yield Strain obtained by Eshragi et al. is 0.037 +/- 0.002, which also matches closely with the experimentally obtained Yield Strain of 0.031 +/- 0.002. These comparisons validate the fixture and the procedure used to obtain compressive material properties at room temperature.

Jerabek et al. have used the extrapolation method to obtain different parameters for the material model [96]. However, caution should be observed when extrapolating parameters with significant variance. In the current research, out of the three parameters needed for large deformation simulations in DEFORM 3D, experimentally obtained Yield Strength and Strength Coefficient have some significant variance, with the coefficient of variation changing with aspect ratio.

Although there is no direct association of variance and aspect ratio, it is a conservative approach to extrapolate variances in these parameters for a reciprocal aspect ratio d/l equal to zero. Effectively, this method creates an upper bound and a lower bound for the effective theoretical flow stress curve.

The FE simulation on DEFORM can be run with mean, upper bound, and lower bound values of the flow stress and results can be compared to see which one best represents the actual material properties. It can be seen from Table 5.3 and Table 5.4 that the variance of Yield Strength and the Strain Hardening Exponent are decreasing as d/l is reduced from 1 to 2/3. Therefore, upon extrapolation of the upper bound and the lower bound values of these parameters, they will converge before reaching d/l equal to zero, which may result in negative variances and therefore can be neglected. However, the variance of the Strength Coefficient diverges as the reciprocal aspect ratio is reduced.

Therefore, this parameter will have a proper upper bound and a lower bound when extrapolated to d/l equal to zero as shown in Figure 5.18.

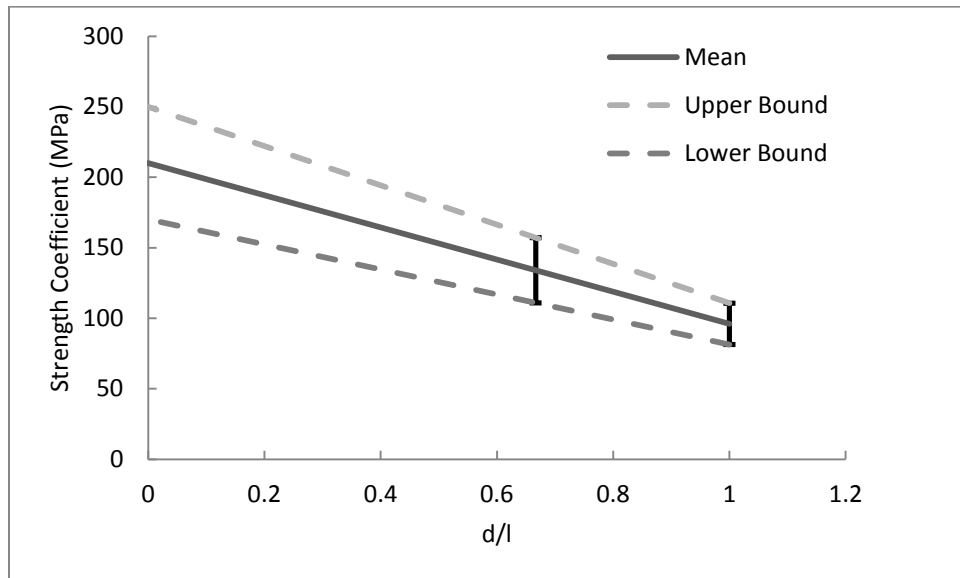


Figure 5.18 Extrapolation of Strength Coefficient to $d/l = 0$

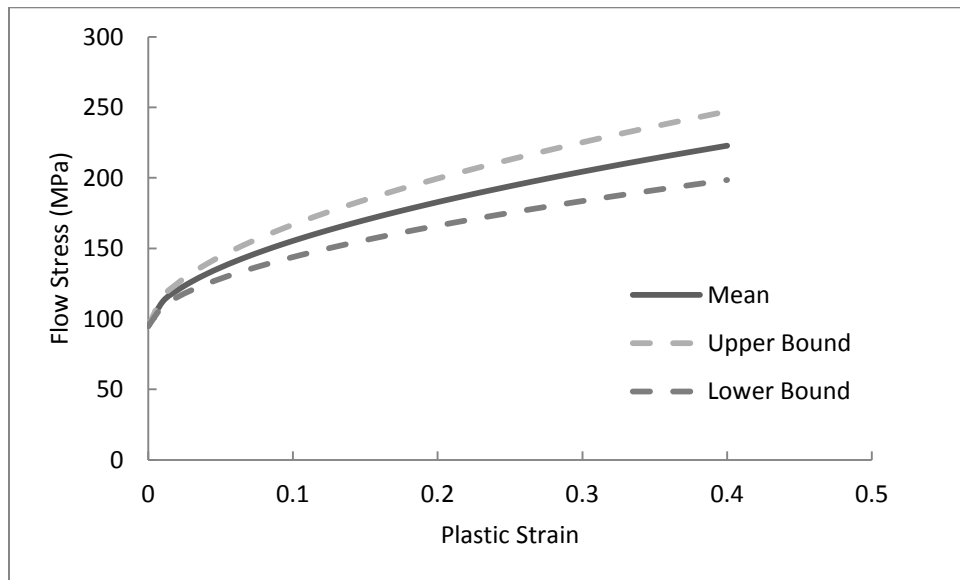


Figure 5.19 Flow Stress for three different values of the Strength Coefficient

Upon using the extrapolated Strength Coefficient, its upper bound and lower bound values are found to be 249.9 MPa and 170.1 MPa, respectively. The flow stress is plotted for all three values of the Strength Coefficient in Figure 5.19.

Three parameters are needed to define flow stress in DEFORM 3D; Yield Strength, Strain Hardening Exponent, and Strength Coefficient. The first two parameters show negligible variation for reciprocal of aspect ratio $d/l = 0$ obtained after extrapolating the experimental data. Therefore, these parameter values are used without any upper or lower bounds. However, the last parameter i.e. Strength Coefficient showed some significant variation for the extrapolated results. Therefore, simulations were carried out for three different Strength Coefficient values; the mean, the lower bound, and the upper bound. The results of peak punching force obtained by all three models with three different strength coefficients are compared with the experimentally obtained peak punching forces.

Chapter 6

Cryogenic Micropunching of Polycaprolactone

6.1. Introduction

A high volume micropunching method is essential to fabricating a vascular 3D tissue scaffold by multilayer membrane stacking. This method requires that thousands of hole features be punched in the extruded PCL membranes prior to bonding individual 2D layers. However, as demonstrated in pilot studies, PCL is difficult to punch at room temperature due to its high fracture strain. The circular punch-outs are inclined to stick to the surface of the PCL membrane as they are often partially sheared or the punch simply forms a pocket in the membrane without initiating shear. Therefore, the micropunching setup introduced in Chapter 3 is modified to reduce the temperature of PCL to below its glass transition temperature by using liquid nitrogen to invoke a brittle material response. In this modified micropunching method, coined here as “cryogenic micropunching,” through holes are punched quite easily in PCL, but the required punching force increases substantially when compared to requirements at room temperature.

Single punching of circular holes is considered in this research, but non-circular holes are of interest as they enable engineers to have more flexibility in designing the microarchitecture required for fully vascularized tissue scaffolds. For example, a series of holes and rectangular slots can be punched in several membranes, which are then aligned,

stacked, and bonded to form microtubules for profusion of nutrients and removal of cellular waste products.

To improve manufacturing capacity and efficiency, it is desirable to punch more than one hole feature during a single stroke of the press. This requires a male die with multiple punches and a female die with a mating hole pattern. However, due to manufacturing constrains, it is difficult to make non-circular punches from contemporary metallic die materials and related manufacturing processes. To date, a compound die set with multiple microscale punches has not been successively manufactured and demonstrated.

An attractive alternative to metal die sets is to use silicon wafers as a die block and to capitalize on manufacturing methods developed by the microelectronics industry, such as photolithographic masking and ionic etching. With these methods, punches of virtually any size and shape can be fabricated to produce silicon micropunches at a relatively low cost. In addition, several punches can be fabricated on a single die set for the same cost as producing a single punch. However, die life is a concern as silicon is a brittle material so it is important to have an estimation of punching force when designing silicon die sets.

In this chapter, the finite element method is investigated to predict the maximum punching force when creating 200 um diameter holes in PCL membranes that are cooled by liquid nitrogen. Given the brittle nature of silicon dies, experimental verification is pursued here with a cryogenic punching arrangement that uses a single ground steel punch and a mating laser cut stainless steel female die. A Design of Experiments approach is used to determine the experimental trials while investigating the effect of different die clearances and film thicknesses on punching force and hole pattern quality.

6.2. Material and Methods

6.2.1. Polycaprolactone Membrane

To produce PCL membranes, pellets with an average length and diameter of 3mm were purchased from Sigma Aldrich (Part No. 440744, Saint Louis, MO). Note, these are the same pellets that were previously described in Chapter 5 for making injection molded specimens for compression testing. However, for membrane fabrication, a hot melt extrusion process was pursued with a DSM Xplore Micro 15 cc twin screw micro-compounder, Figure 6.1.



Figure 6.1 DSM Xplore Micro 15 cc twin screw micro-compounder. Figure courtesy: [4]

The thickness of the extruded membrane (film) is controlled by changing temperature, extrusion slot width, and extruded film tension. Film tension is controlled by rotational speed of the material rollers that collect the finished product. PCL films obtained by hot melt extrusion were of thicknesses varying from 25 to 80 μm , with a constant width of approximately 15 mm.

6.2.2. Cryogenic Micropunching Machine

Two liquid nitrogen reservoirs were added to the micropunching machine that was previously described in Chapter 3. The reservoirs facilitated the cryogenic micropunching process by cooling the die sets and PCL film to below -60 degrees Celsius. One liquid nitrogen reservoir was added to the female die holder, Figure 6.2, while a second was added to the male die holder, Figure 6.3.

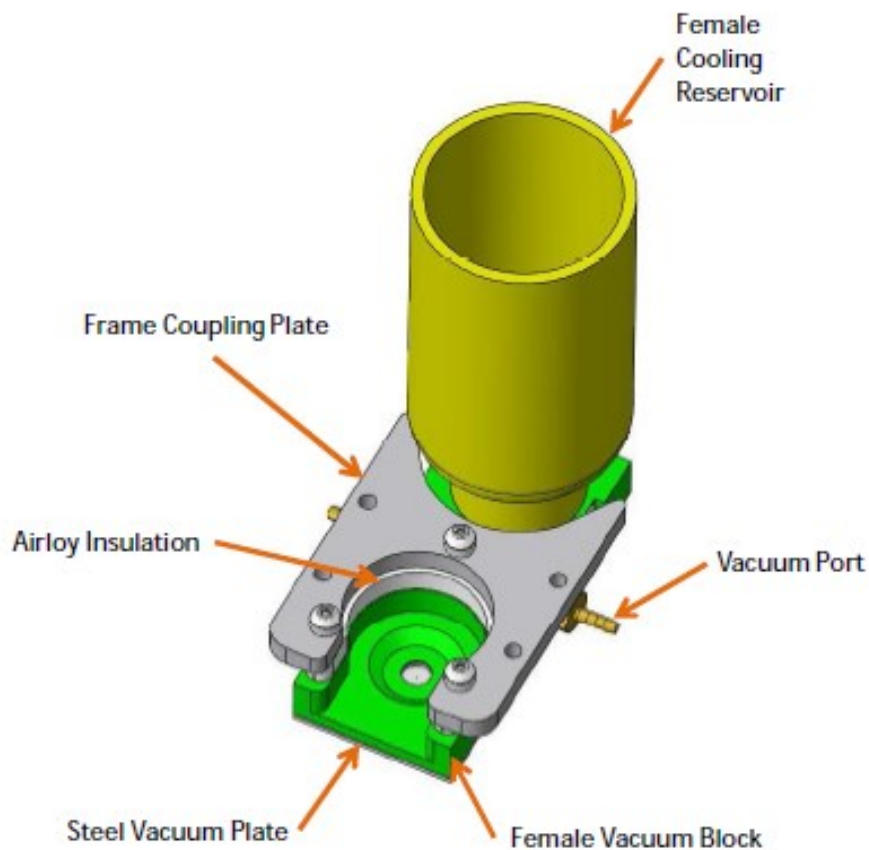


Figure 6.2 Female die assembly with liquid nitrogen reservoir.

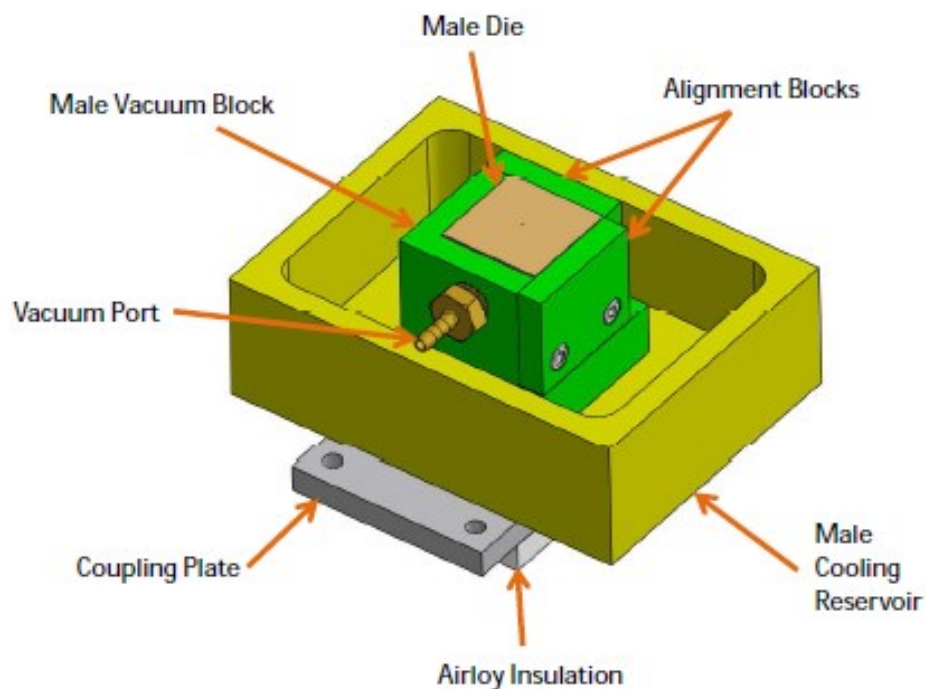


Figure 6.3 Male die block assembly with liquid nitrogen reservoir

When liquid nitrogen is poured into the Female Cooling Reservoir, the Female Vacuum Block comes in direct contact with liquid nitrogen. A series of fins in the Female Vacuum Block assists with heat transfer, Figure 6.4. The Female Vacuum Block is also in direct contact with the Steel Vacuum Plate, which in turn makes indirect contact with the stainless steel laser cut female die.

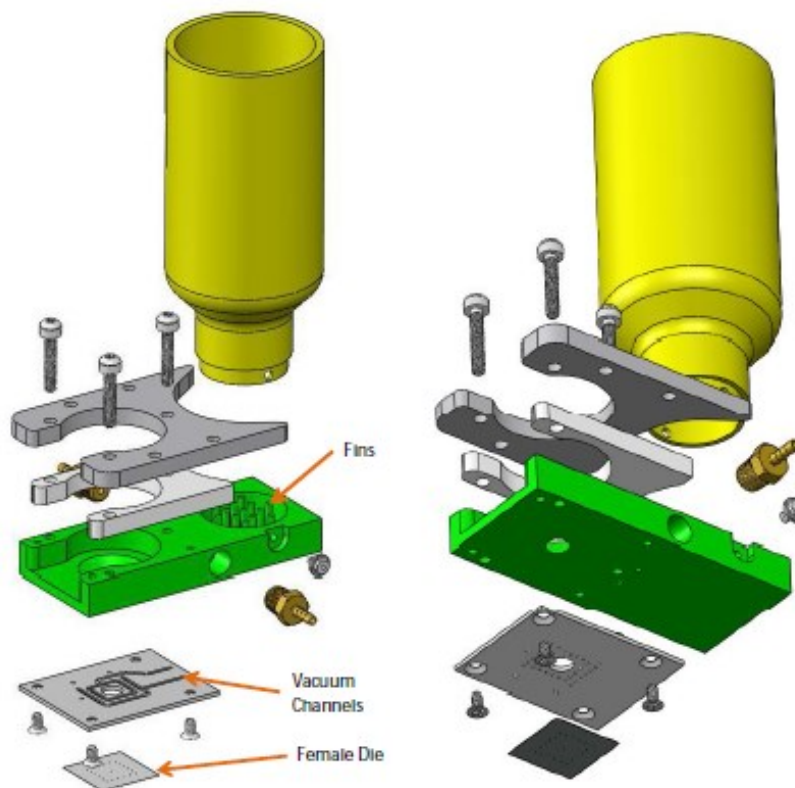


Figure 6.4 Exploded view of the female die cooling system

Prior to micropunching, the PCL film is brought into intimate contact with the female die by applying slight tension to the film. The entire female die block assembly, including the liquid nitrogen reservoir, is thermally isolated from the machine frame by Airloy blocks. Hence, within a few minutes of filling the reservoir with liquid nitrogen, the thin PCL film obtains thermal equilibrium at a temperature well below the glass transition temperature of $-60\text{ }^{\circ}\text{C}$. During the micropunching experiments, it is necessary to periodically fill the reservoirs to account for the volume of liquid nitrogen lost as it slowly boils.

As the die block assemblies begin to cool, a frost accumulates on the components due to moisture in the air. To avoid frosting near the dies, the upper half of

micropunching machine is enclosed in an airtight, transparent plastic bag. The inside of the bag is backfilled with dry nitrogen gas and maintained at a pressure slightly above atmospheric pressure to avoid an influx of humid air. This process keeps the dies and microscope viewing port free from frost.

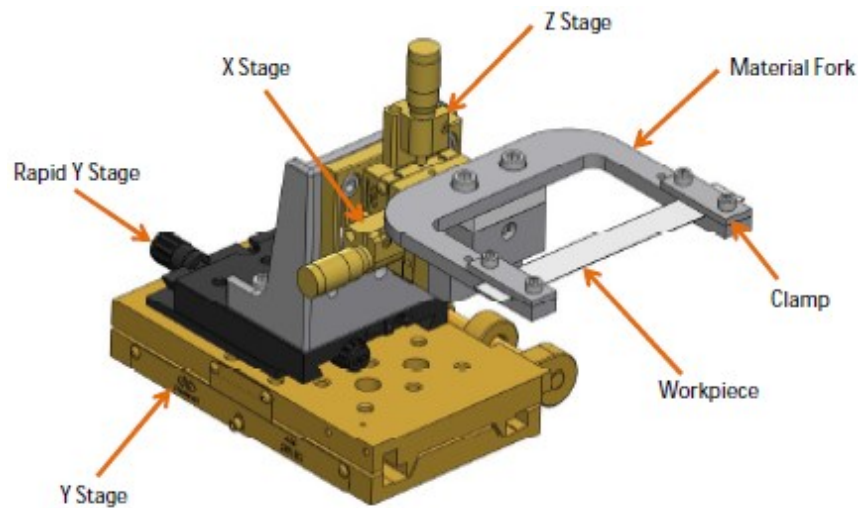


Figure 6.5 Material holder with XYZ translation staging.

The PCL film is held in tension by a material holder, Figure 6.5, which keeps the film in contact with the female die and the Female Vacuum Block. The material holder is attached to a precision three axis stage. The material can be moved against the female die to ensure a positive contact and additional tension in the film. The material holder can also be moved in a transverse direction to precisely control the location of the hole within the workpiece.

6.2.3. Male and Female Dies

Similar to copper foil punching experiments explained in Chapter 3, stainless steel gage pins, 200 μm in diameter (Model 21135A71, McMaster-Carr, Princeton, NJ, USA), are used for all experiments, Figure 6.6.

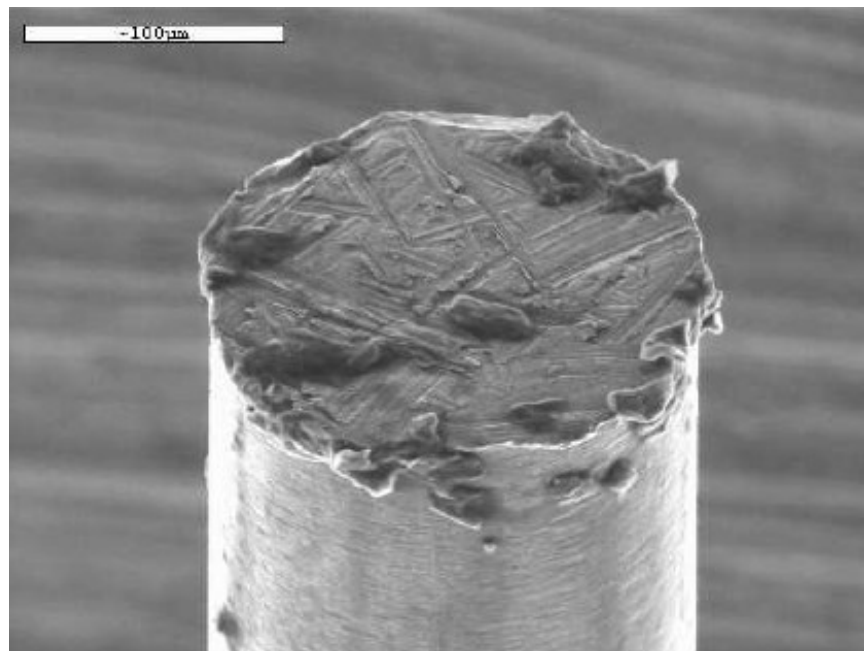


Figure 6.6 SEM image of a gage pin used as a punch.

With some gage pins, a manufacturing defect was observed where the punch face in the as received condition was not flat, Figures 6.7 and 6.8. A slanted punch results in a lower punching force as described in Chapter 4. Therefore, all gage pins used to validate the FE simulation were observed to be free from manufacturing defects i.e. the punch faces were confirmed to be flat.

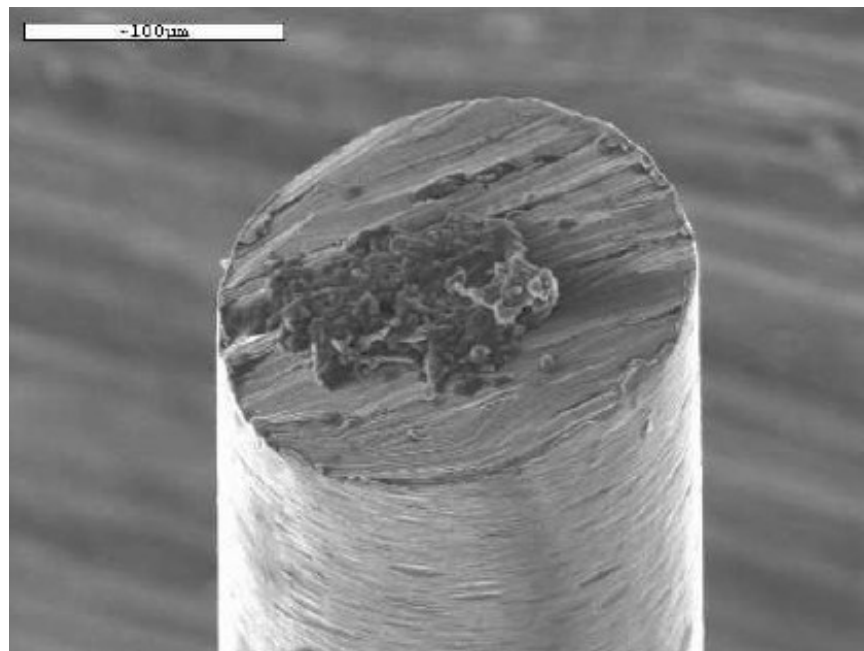


Figure 6.7 SEM image of a slanted punch face

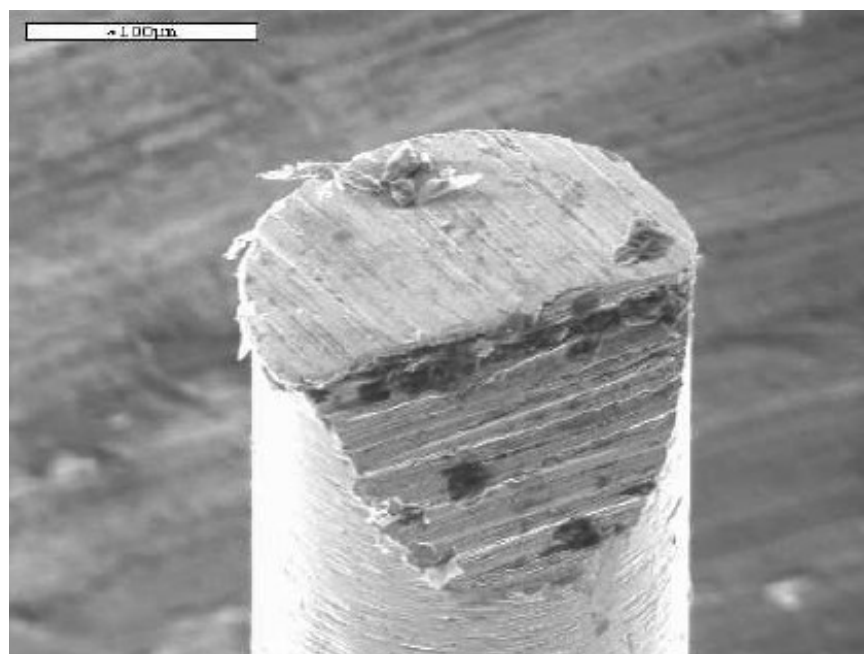


Figure 6.8 SEM image of sheared facet at the end of a punch face

The female die is manufactured by laser cutting holes of various diameters in 150 μm thick, 25 mm by 25 mm square, ground stainless steel plate (Photo Etch Technology, Lowell, MA, USA). The entry side of the laser can create a splash of molten metal, Figure 6.9, while the exit side can exhibit a burr, Figure 6.10.

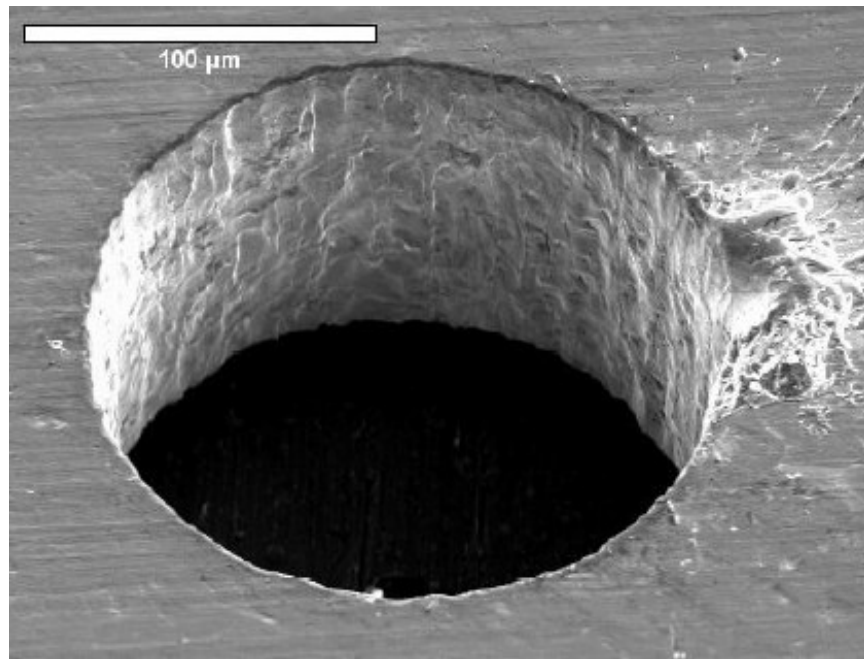


Figure 6.9 SEM image of the entry side of a laser cut stainless steel female die (210 μm hole diameter, 150 μm thick stainless steel)

A laser cut hole exhibits some taper, with the entrance side diameter larger than the exit side diameter. When referring to a hole size for the female die, the diameter herein refers to the exit side, which is the side that faces the workpiece and first engages the male punch. The tapered hole has the benefit of assisting in stripping the punch-out from the male die.

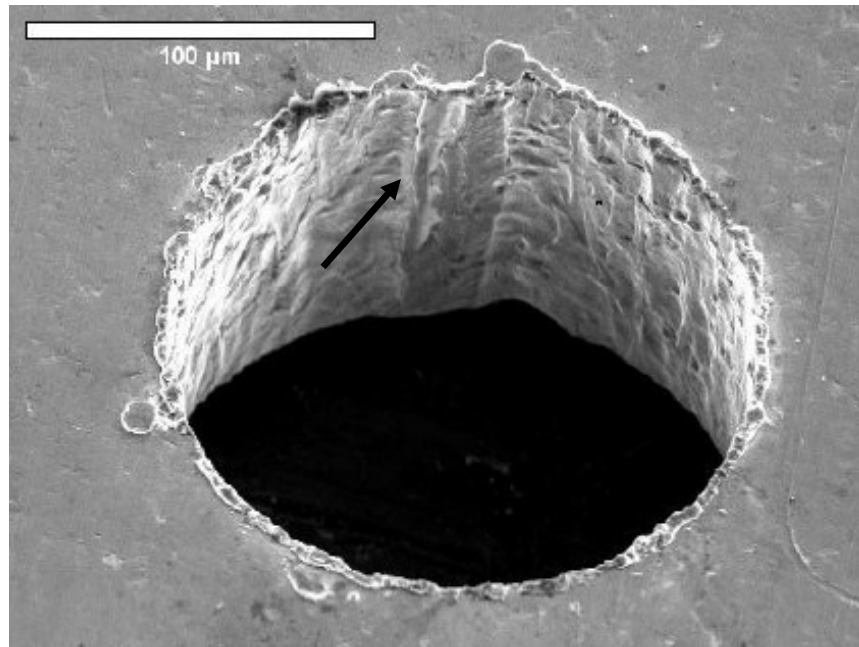


Figure 6.10 SEM image of the exit side of a laser cut stainless steel female die. The arrow shows a small step along the perimeter of the hole. The step is an artifact from the laser cutting process.

Imperfections in the shape of the hole can exist when fabricating the female die by laser cutting as denoted by the arrow in Figure 6.10. This issue can be minimized by creating the hole by two passes of the laser. The first pass i.e. roughing cut is for a hole slightly smaller than desired, while the second pass i.e. finishing cut removes a slight amount of material from the hole circumference.

6.2.4. Finite Element Method

DEFORM v10.2.1 (Scientific Forming Technology Corporation, Columbus, OH, USA) is used to simulate cryogenic micropunching of PCL. The details of DEFORM 3D and the implemented finite element models were introduced in Chapter 3 for simulating copper micropunching. As in the copper punching simulations, there are three parts to the PCL micropunching model: (1) female die, (2) male die, and (3) workpiece.

6.2.4.1. Model Geometry

In the experiment, the female die base is approximately 25 mm by 25 mm square and the strip of PCL film is approximately 12 mm wide by 125 mm long. However, in the FE model, a 1 mm by 1 mm section of the female die and workpiece is considered to avoid an unnecessarily high number of elements during meshing.

The male die is a cylinder with a 200 μm diameter and a 400 μm length. Simulations were carried out for three combinations of male punch diameter and female hole diameter: 1) male 200 μm , female 212 μm , 2) male 200 μm , female 224 μm , and 3) male 200 μm , female 236 μm . This resulted in a single sided radial die clearance of 6 μm , 12 μm , and 18 μm , respectively.

Considering the difference in modulus between the steel dies and the PCL workpiece, the dies were assumed to be perfectly rigid.

Two different PCL film thicknesses were considered for simulation: (1) 40 μm , and (2) 70 μm . The combination of material thickness and radial die clearance resulted in six simulations of various die clearance. Die clearance is defined as a percentage of the material thickness i.e. $(\text{material thickness} / \text{single sided die clearance}) \times 100\%$. Therefore, the die clearances investigated are 8.6%, 15%, 17.1%, 25.7%, 30%, and 45%. For these six cases, symmetry permits the use of a quarter model to reduce computational time, Figure 6.11.

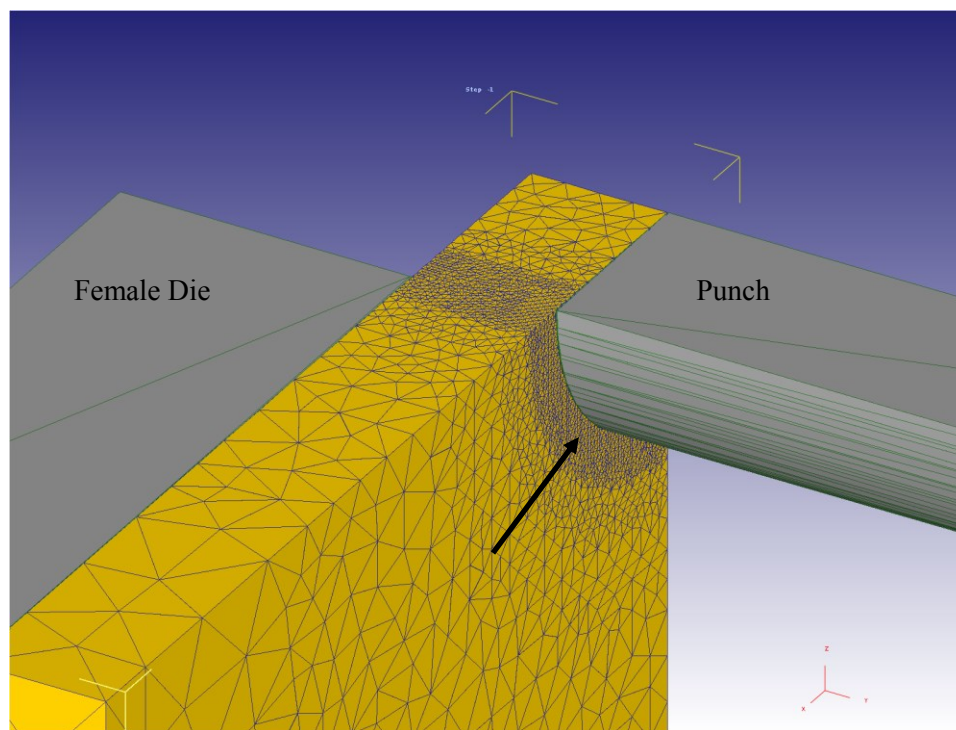


Figure 6.11 FEA model of fully aligned die sets during cryogenic micropunching of PCL. Symmetry permits a quarter model. The mesh is refined in the shear zone (arrow).

Apart from the six FE models pursued to investigate the effect of die clearance on maximum punching force, one additional model is simulated. This model has a male die diameter of $200\ \mu\text{m}$, a female die diameter of $236\ \mu\text{m}$, and a PCL film thickness of $70\ \mu\text{m}$, resulting in a die clearance of 25.7%. However, the male and female dies are not aligned coaxially, but rather a die eccentricity of $17\ \mu\text{m}$ is used to simulate die misalignment. For this case, the lack of full symmetry requires a half model for simulation.

6.2.4.2. Application of Boundary Conditions

To keep the model representative of the actual experimental setup, two parallel ends of the square shaped workpiece are fixed and other two are free. As one can imagine, although the boundary conditions are not axisymmetric, the arrangement affords planar symmetry about both axes on the workpiece plane. Therefore, a one quarter model is valid for simulation.

The contact surfaces between the die halves and the workpiece were modeled with shear friction. According to the DEFORM 3D manual, this friction model is recommended for most forming processes where there is negligible sliding. In this model, the frictional stress is defined as the product of friction factor and the shear yield strength. DEFORM also offers modeling contacts with Coulomb friction, however, that is recommended for cases where at least one of the objects is deforming elastically. In order to understand the degree of sliding and the effect of the friction model used, simulations were run with both friction models. The obtained punching force profiles were compared and found to be almost identical in their shape and peak value. Therefore, the DEFORM recommended shear friction model is used for all simulations.

Apart from shear and coulomb friction models, DEFORM 3D has a hybrid model, which is a combination of shear and coulomb friction models, and a constant Tau model, where the friction stress can be set as a constant value by the user. Since both shear and coulomb models have the same effect on punching force, the hybrid model was not considered. Similarly, the constant Tau model was not considered as it is not suitable for the current forming process.

A coefficient of friction for PCL in contact with steel at room temperature or at cryogenic temperatures is not available in literature. However, since there is very little

sliding between the workpiece and the dies during micropunching, the exact friction coefficient may not be needed. The DEFORM 3D manual has a procedure to decide whether a typical friction coefficient is sufficient or if a careful determination of the friction coefficient is required. According to the manual, one should run the simulation at two different friction coefficients approximately 20 % different from the typical value. If the resulting load values are not significantly different, a typical value of the friction coefficient is sufficient.

Although the friction coefficient between PCL and steel is not available, friction coefficients are available for Polystyrene-Steel and Polythene-Steel in [90] and are equal to 0.30-0.35 and 0.20, respectively. Therefore, to understand the effect of friction coefficient, three different simulations were done with three different friction coefficients; 0.10, 0.30, and 0.40. The punching force obtained from all three simulations were compared. The difference in punching forces were negligible indicating that a typical value of friction coefficient is sufficient. Therefore, a friction coefficient of 0.30 is used for all contacting surfaces.

6.2.4.3. Verification of Model Convergence

A number of convergence tests were carried out to obtain the optimal values of smallest element size, solution increment step size, work piece dimensions, and boundary conditions. The smallest element size considered for the 70 μm film thickness was set to be 4.0 μm . However, after meshing, the measured smallest element side length was 2.8 μm . DEFORM 3D creates tetrahedron shaped elements for punching simulations. These tetrahedrons are not regular in shape in order to cover the complete workpiece geometry, including edges and high curvature surfaces. Therefore, although the meshing algorithm tries to achieve the minimum element size set by the user, most of the time it ends up creating elements with the smallest side length slightly smaller than the user set element

size. This ensured approximately 40 to 50 elements across the thickness of the workpiece. Note that since the elements are tetrahedral in shape, the effective number of elements across the thickness is more than the ratio of the thickness and the smallest element size. Similarly, for the case with material thickness of 40 μm , the smallest element side length measured was 1.9 μm . In all simulations, modified mini-elements were used, details of which are not published by DEFORM.

The solution increment step (incremental movement of the punch into the workpiece) was set at 0.10 μm , which is approximately 20 times smaller than the smallest element size. This exceeds the requirement that the solution increment step be at least 10 times smaller than element size as recommended in the DEFORM 3D user manual to avoid large deformation of the elements, which can result in numerical instability.

The workpiece dimensions were optimized to have a minimum number of elements without losing accuracy. The high deformation zone lies within the die clearance regime. The largest radial clearance simulated is 18 μm , which is much smaller than the 1 mm square work piece specified. A pilot study indicated that small variations in the workpiece dimensions did not have a significant effect on the calculated peak punching force.

Similarly, to mimic the experimental conditions, tension boundary conditions were applied to the workpiece and compared to simulations with fixed boundary conditions (two sides fixed and two sides free). There was no statistically significant difference in the calculated maximum punching force when considering the various workpiece boundary conditions. Hence, fixed boundary conditions were used for all simulations to minimize complexity and to reduce computational time.

6.2.5. Workpiece Material Modeling

Polycaprolactone cooled with liquid nitrogen is used as the workpiece material for studying cryogenic micropunching. Although material properties of PCL at room temperature are available in literature, no information about the material properties is available below its glass transition temperature. Therefore, the material properties of PCL in liquid nitrogen are obtained experimentally to be used in DEFORM 3D finite element simulations to predict micropunching forces.

Recalling the material characterization outlined in Chapter 5, Ludwik's equation was used for the flow stress of PCL in liquid nitrogen.

$$\sigma = Y + K\varepsilon_p^n \quad (6.1)$$

The parameters Y , K , and n obtained experimentally are equal to 94.8 MPa, 210 MPa, and 0.5405, respectively. Besides 210 MPa as the mean strength coefficient, the variations in K from 170.1 MPa to 249.9 MPa are also considered for the simulations to see the upper and lower bound of the predicted punching force. Similar to copper punching simulations described in Section 3.2.6, Normalized Cockcroft and Lantham model is used to simulate fracture, however, element deletion is used for PCL micropunching instead of element softening to obtain a better visualization of the fractured surface.

6.2.6. Design of Experiments

A pilot study was conducted to determine the appropriate sample size for the main set of experiments. The study consisted of punching twenty holes of nominal diameter 200 μm in 25 μm thick PCL films with a die clearance of 7.6 %.

Punching forces are measured using a dynamometer (Type 9047C, Kistler, Winterthur, Switzerland), accompanied by a charge amplifier (ICAM 5073, Kistler

Instrument Corp., Amherst, NY). Data collection is done through a multifunctional data acquisition board (PCI 6132, National Instruments, Austin, TX). The raw force data is smoothed in Matlab using the function “LOWESS” (locally weighted scatter plot smooth) function, a local linear regression filter with a tricube weight function.

Results of the pilot study are given in Table 6.1.

Table 6.1 Summary of punching forces for a pilot study

Parameter	Value
N	20
Average Peak Punching Force	1.69 N
St. Dev.	0.27 N
C.V.	16.1 %
Maximum	2.24 N
Minimum	1.31 N

Methods given in ASTM E178-08 were used to determine the outliers. One sided Student’s T-test was used with an α level of 0.05. The test parameters corresponding to the maximum and the minimum observed force values are calculated and compared with the critical value corresponding to $\alpha = 5\%$.

$$T_{min} = \frac{(\bar{x} - x_{min})}{s} = \frac{(1.69 - 1.31)}{0.27} = \mathbf{1.407} < 2.557(T_{0.05}) \quad (6.2)$$

$$T_{max} = \frac{(\bar{x} - x_{min})}{s} = \frac{(2.24 - 1.69)}{0.27} = \mathbf{2.037} < 2.557(T_{0.05}) \quad (6.3)$$

Since, both T_{min} and T_{max} are smaller than $T_{0.05}$, none of the data points are considered to be outliers. Considering the mean and the standard deviation of the force values given in Table 6.1, a sample size calculation was done to detect an effect level of 10 % of the mean punching force (0.169 N) with a power of 80 % ($\beta = 0.2$).

$$N = \frac{2\sigma^2(Z_{\alpha/2} + Z_{\beta})^2}{(\Delta F)^2} = \frac{2(0.27)^2(1.96 + 0.84)^2}{(0.169)^2} \approx 41 \quad (6.4)$$

Therefore, at least 41 holes must be punched to detect a 10% difference in the peak punching force as a function of die clearance.

6.3. Results

6.3.1. Peak Punching Force

Peak punching force was recorded for cryogenic micropunching on PCL films with different die clearances. At least 41 holes were punched for most cases to detect a difference of approximately 0.17 N with a power of 80 %. Figure 6.12 shows a comparison of the experimentally determined peak punching force for three different die clearances (8.6%, 17.1% and 25.7%) and a film thickness of 70 μm . Similarly, Figure 6.13 shows a comparison of the experimentally determined peak punching force for three different die clearances (15%, 30%, and 45%) and a film thickness of 40 μm .

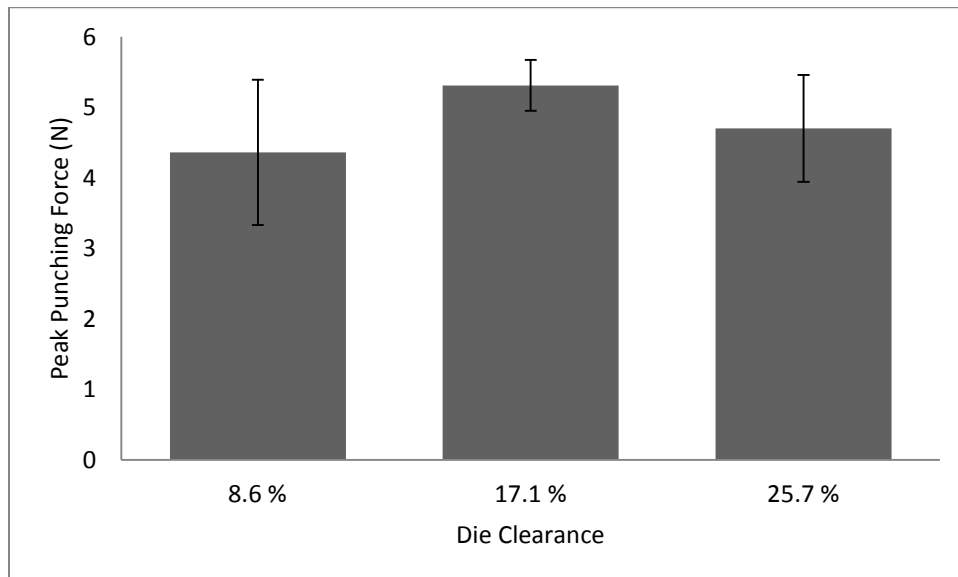


Figure 6.12 Peak punching force as a function of die clearance for 70 μm thick PCL film

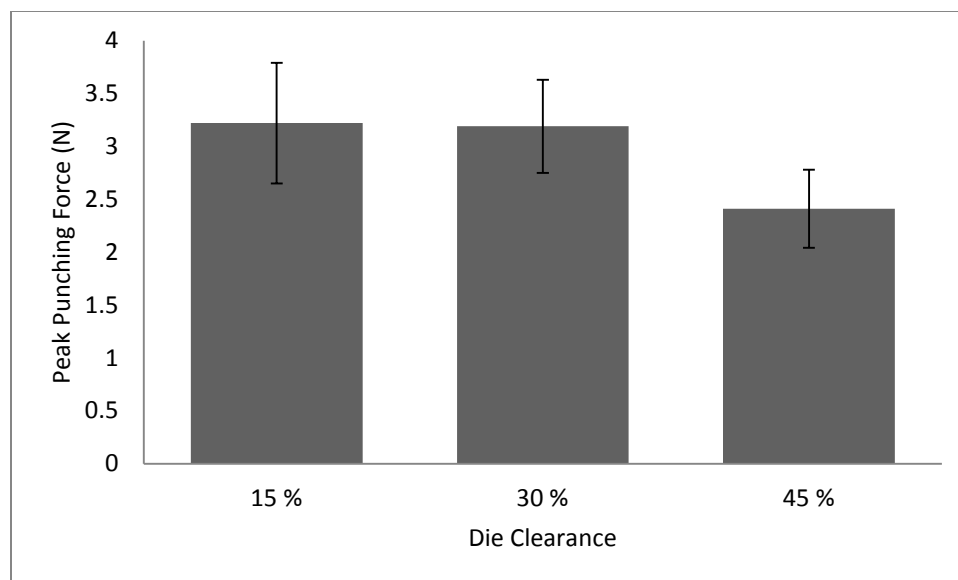


Figure 6.13 Peak punching force as a function of die clearance for 40 μm thick PCL film

The error bars in Figures 6.12 and 6.13 represent plus and minus one standard deviation from the mean peak punching force.

6.3.2. Hole Quality

The quality of the punched micro holes was investigated by taking SEM images. Figure 6.14 and Figure 6.15 show representative images for die clearances of 8.6% and 17.1%, respectively.

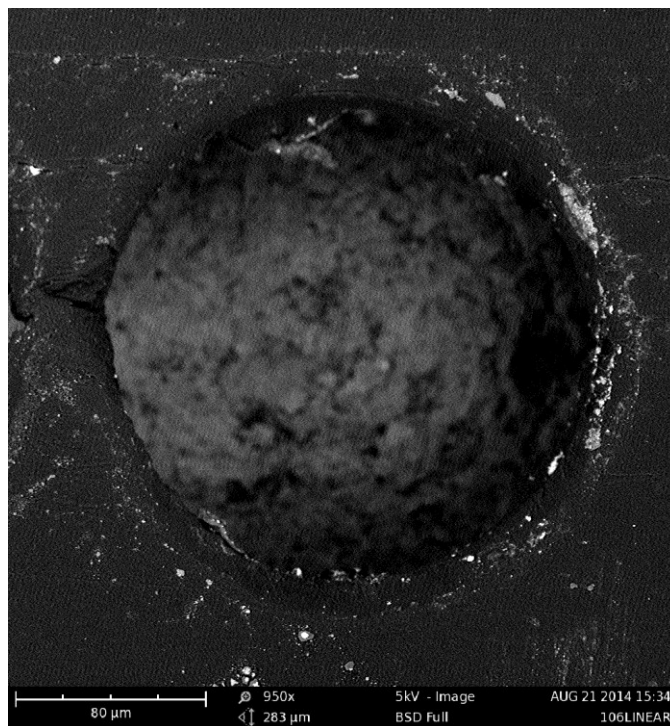


Figure 6.14 SEM image of a micro hole punched with 8.6 % die clearance (70 μm thick PCL film)

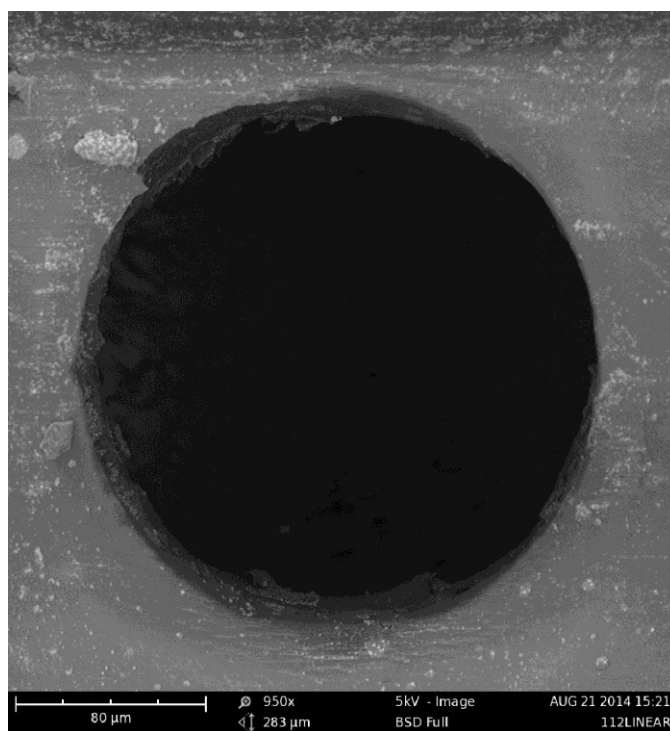


Figure 6.15 SEM image of a micro hole punched with 17.1 % die clearance (70 μm thick PCL film)

Note that as the die clearance increases, a slight misalignment of the dies can result in incomplete punching as shown in Figure 6.16 for the case with 25.7 % die clearance. However, since most of the circumference of the hole is sheared, the measured forces for the incomplete punches are comparable to the forces obtained from simulation.

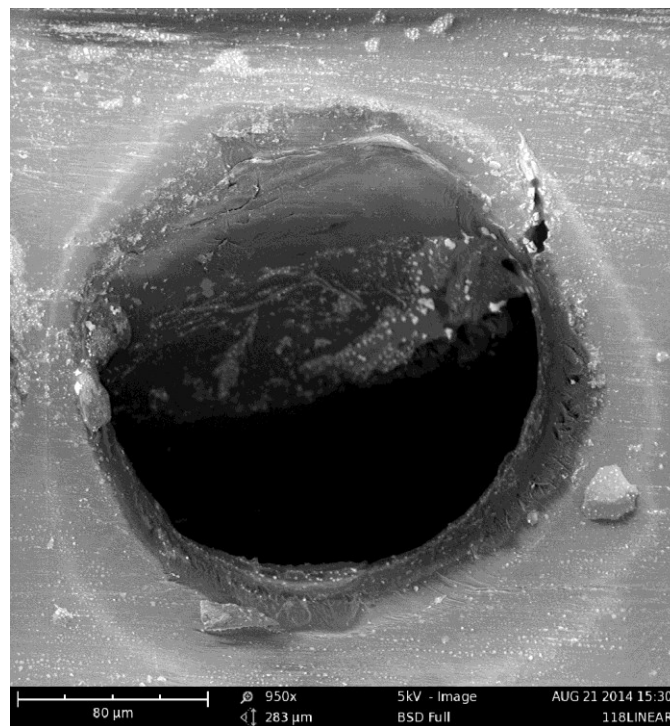


Figure 6.16 SEM image of an incomplete micro hole punched with 25.7 % die clearance (70 μm thick PCL film)

6.3.3. Finite Element Simulations

Apart from the peak punching force, finite element simulation results are processed to obtain stress and strain distribution plots. Figure 6.17 to 6.19 show the stress distribution plots for cryogenic micropunching in 70 μm thick PCL film for 8.6 %, 17.1 %, and 25.7 % die clearance, respectively.

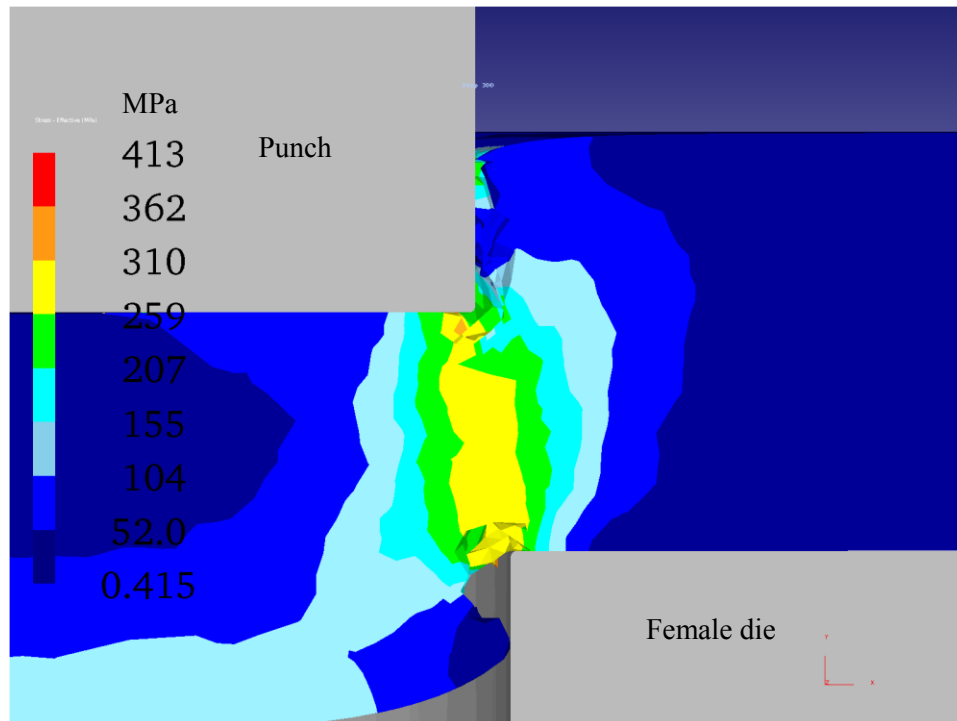


Figure 6.17 Effective stress distribution plot at 30 μm punch stroke for 8.6% die clearance in 70 μm thick PCL film

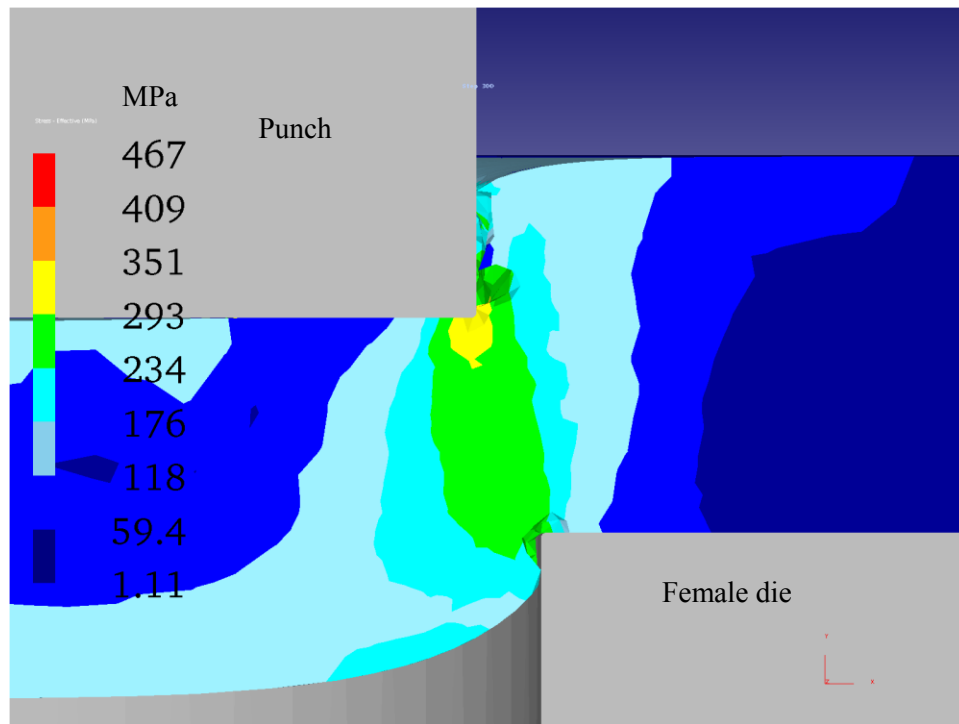


Figure 6.18 Effective stress distribution plot at 30 μm punch stroke for 17.1% die clearance in 70 μm thick PCL film

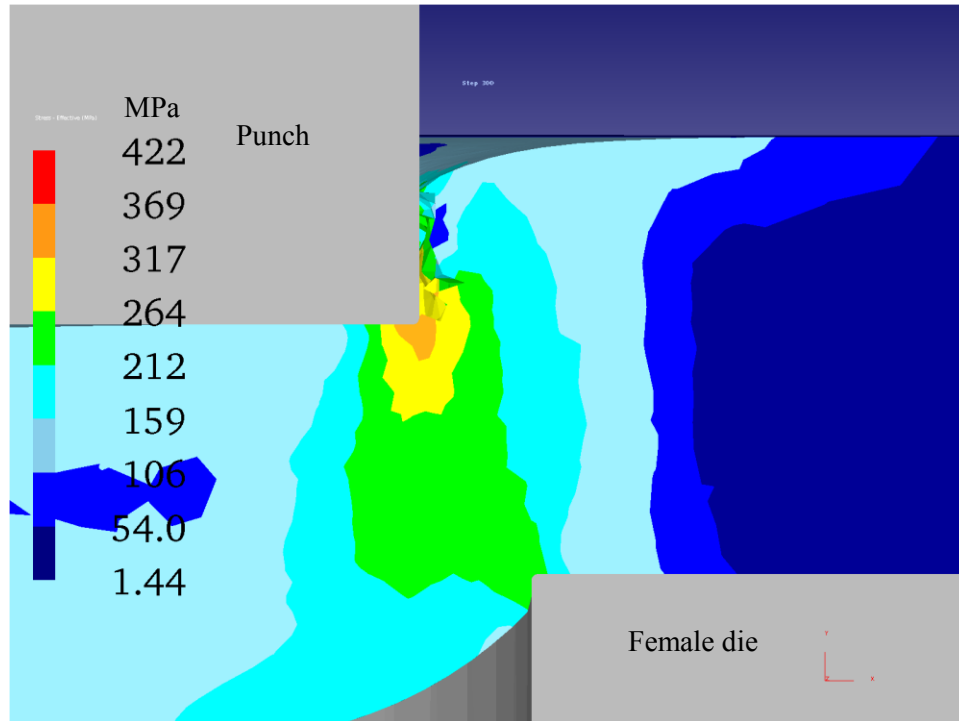


Figure 6.19 Effective stress distribution plot at 30 μm punch stroke for 25.7% die clearance in 70 μm thick PCL film

Figure 6.20 to 6.22 show the strain distribution plots for cryogenic micropunching in 70 μm thick PCL film for 8.6 %, 17.1 %, and 25.7 % die clearances, respectively. Similarly, Figure 6.23 to 6.25 and Figure 6.26 to 6.28, show similar stress and strain distribution plots, respectively, for PCL film thickness of 40 μm . Note, in the case of 40 μm thick PCL, the punch stroke length is reduced from 30 μm to 15 μm in the figures.

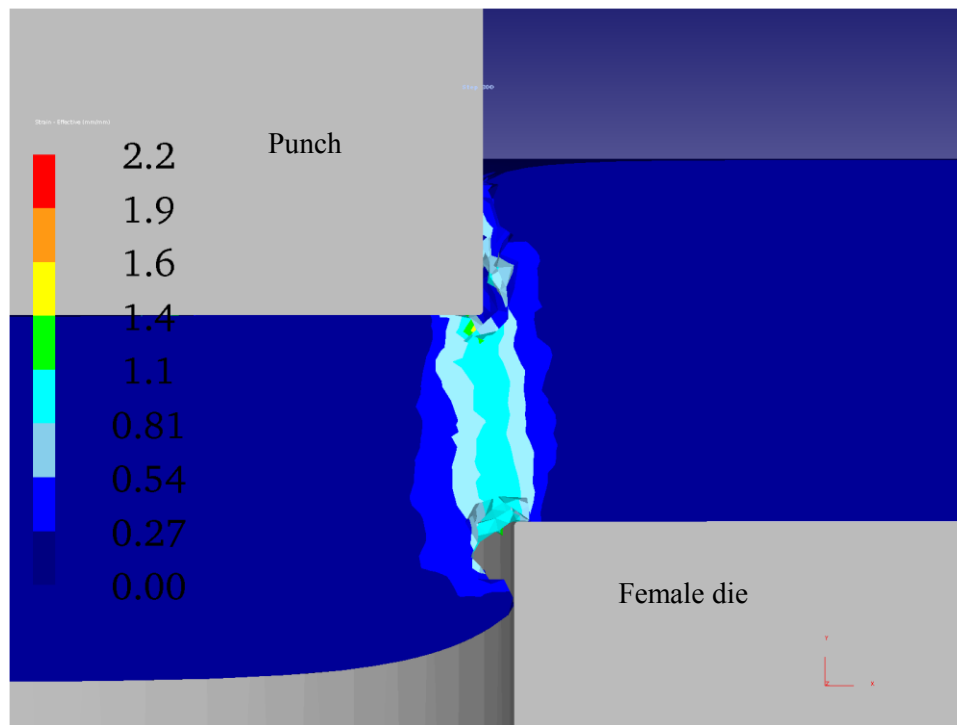


Figure 6.20 Effective strain distribution plot at 30 μm punch stroke for 8.6% die clearance in 70 μm thick PCL film

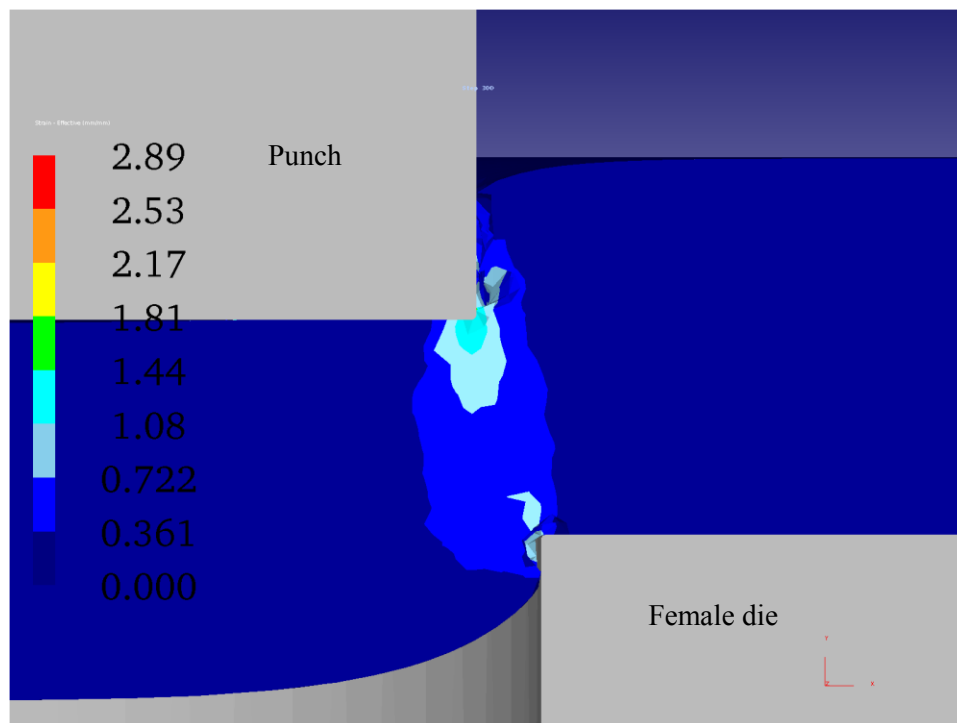


Figure 6.21 Effective strain distribution plot at 30 μm punch stroke for 17.1% die clearance in 70 μm thick PCL film

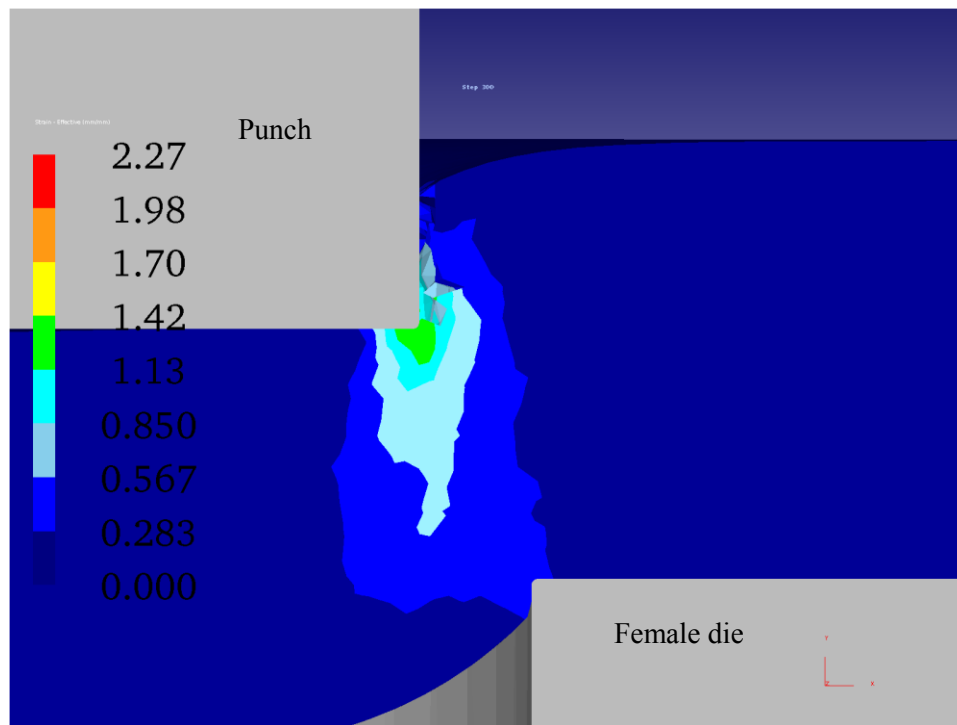


Figure 6.22 Effective strain distribution plot at 30 μm punch stroke for 25.7% die clearance in 70 μm thick PCL film

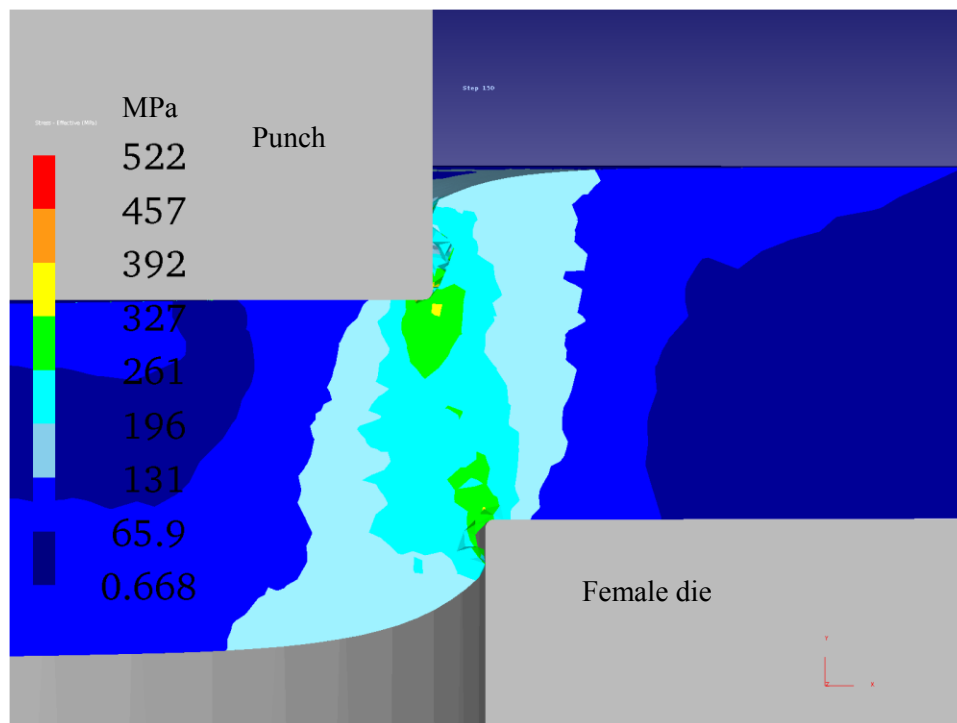


Figure 6.23 Effective stress distribution plot at 15 μm punch stroke for 15% die clearance in 40 μm thick PCL film

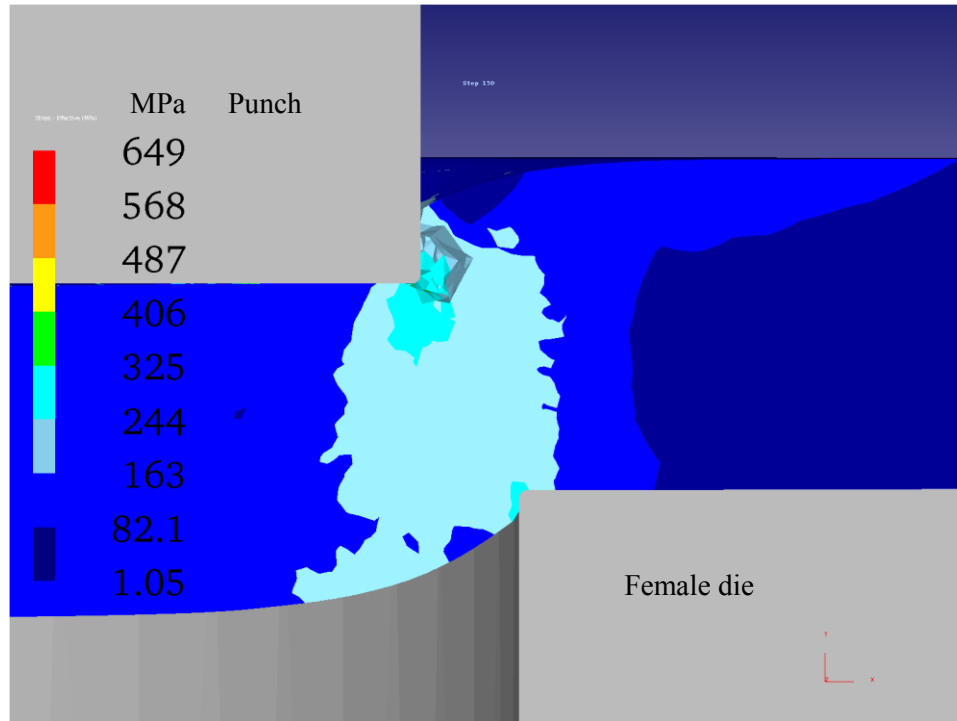


Figure 6.24 Effective stress distribution plot at 15 μm punch stroke for 30% die clearance in 40 μm thick PCL film

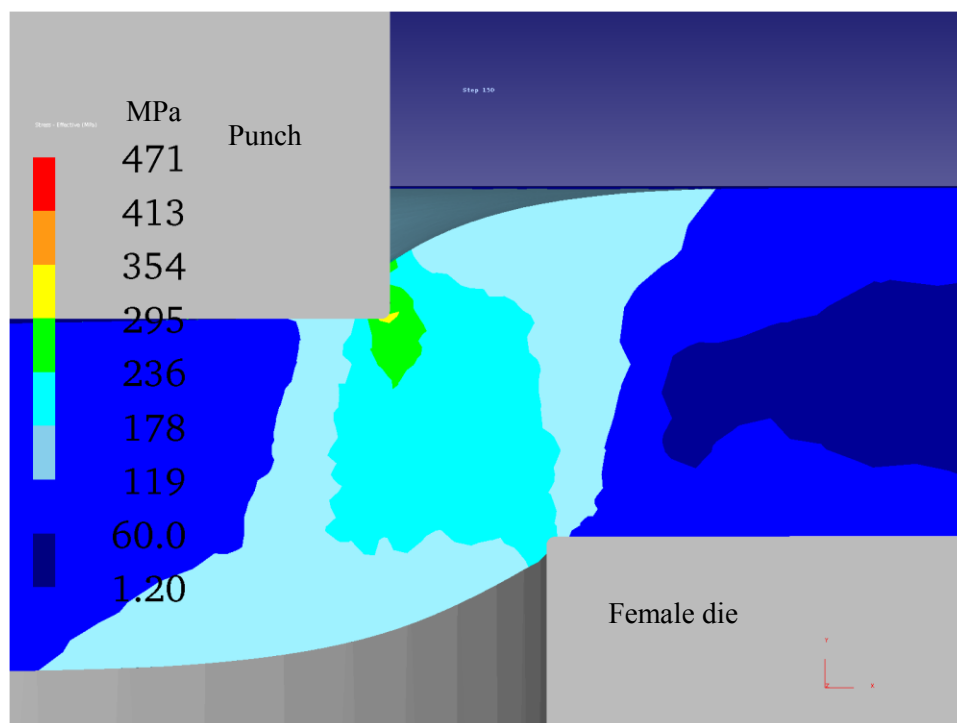


Figure 6.25 Effective stress distribution plot at 15 μm punch stroke for 45 % die clearance in 40 μm thick PCL film

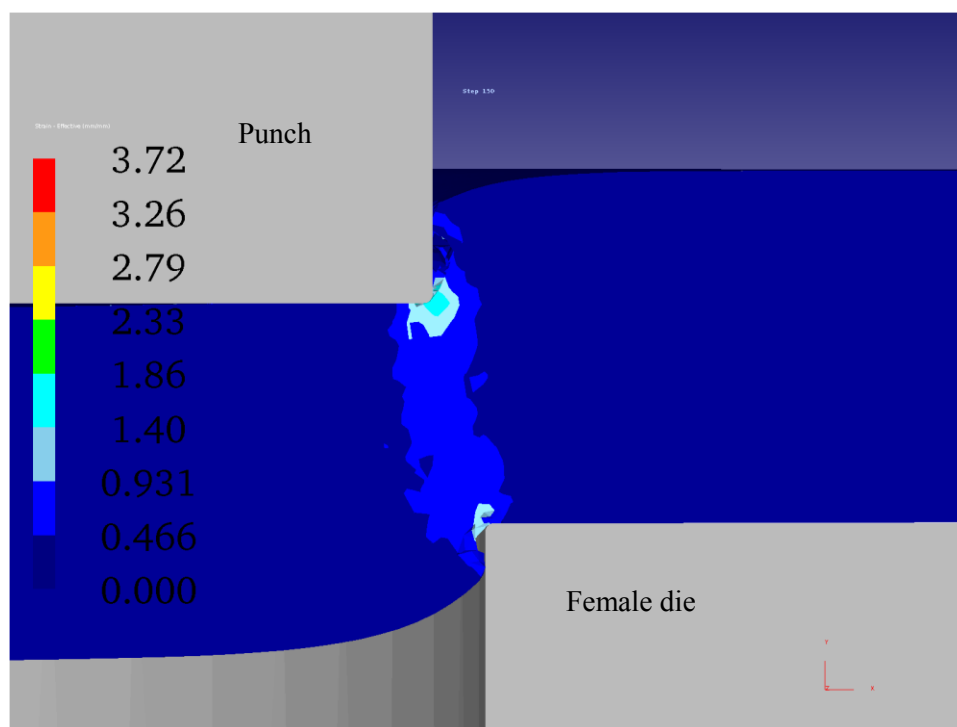


Figure 6.26 Effective strain distribution plot at 15 μm punch stroke for 15 % die clearance in 40 μm thick PCL film

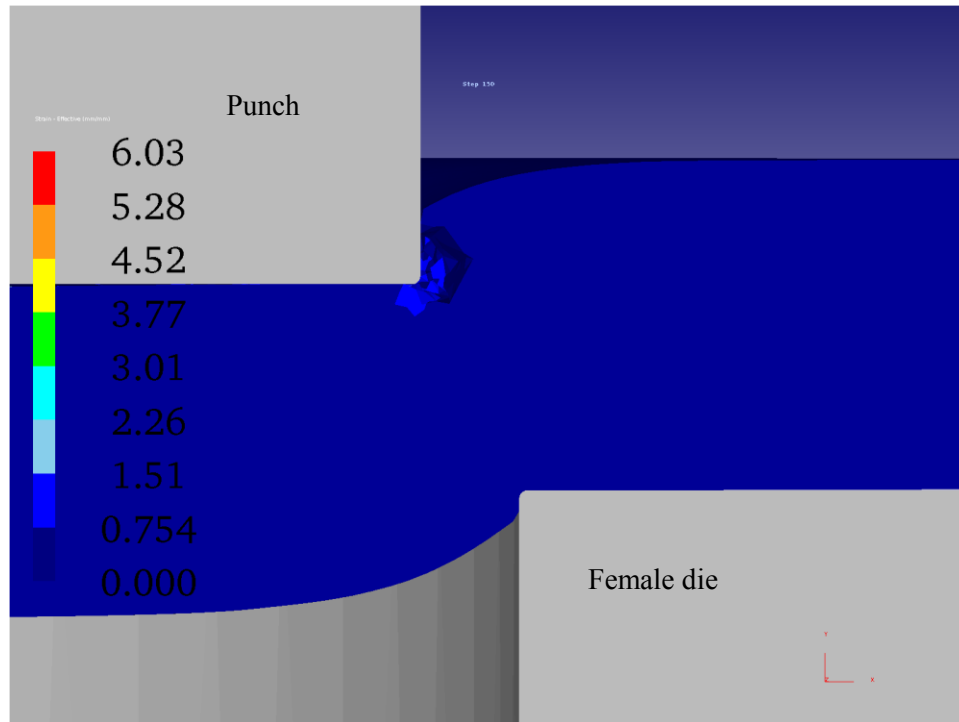


Figure 6.27 Effective strain distribution plot at 15 μm punch stroke for 30 % die clearance in 40 μm thick PCL film

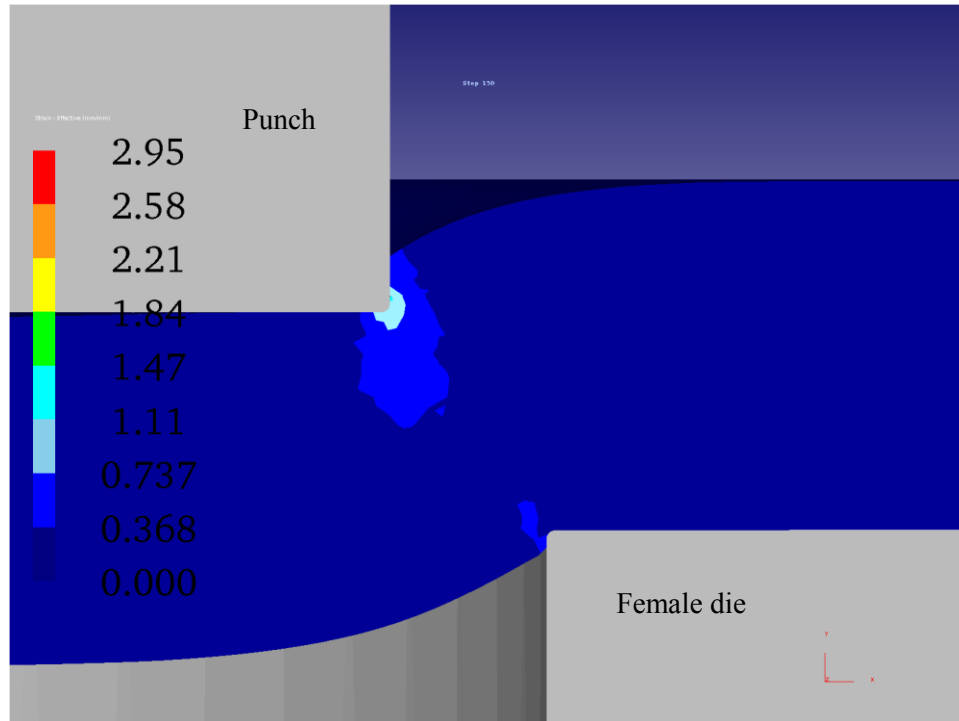


Figure 6.28 Effective strain distribution plot at 15 μm punch stroke for 45 % die clearance in 40 μm thick PCL film

The cross section of the finite element model for the misaligned punching case is given in Figure 6.29.

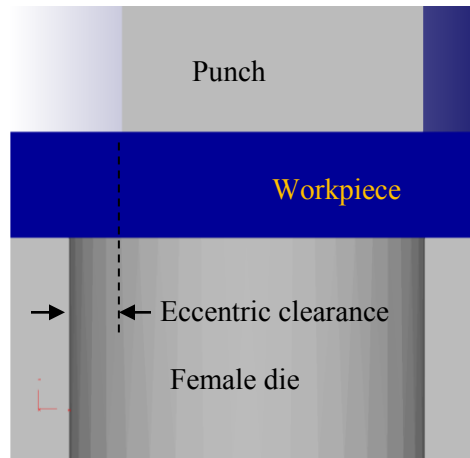


Figure 6.29 Finite element model for simulating misaligned micropunching.

The misaligned punch results in incomplete shearing of the punch out, Figure 6.30.

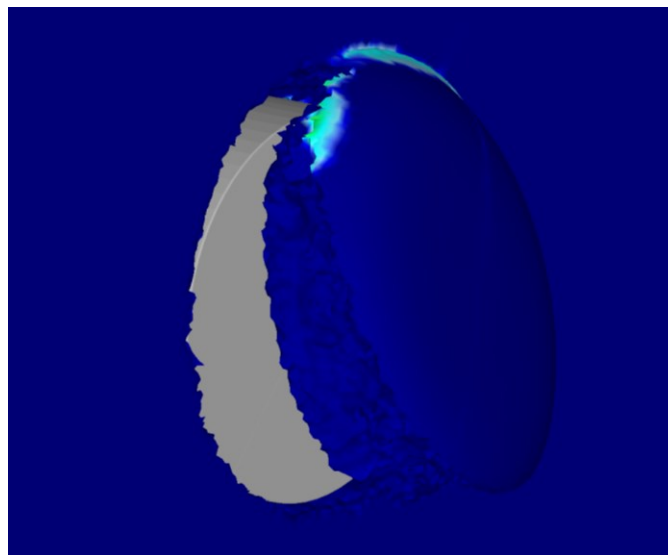


Figure 6.30 Non-symmetric opening of micro hole due to misaligned punching

The stress and strain distribution plots for the misaligned micropunching case are given in Figure 6.31 and Figure 6.32, respectively, for six different punch stroke lengths from

10 μm to 60 μm in increments of 10 μm . Incomplete shearing is visible in Figure 6.31(f), corresponding to the top view shown in Figure 6.30.

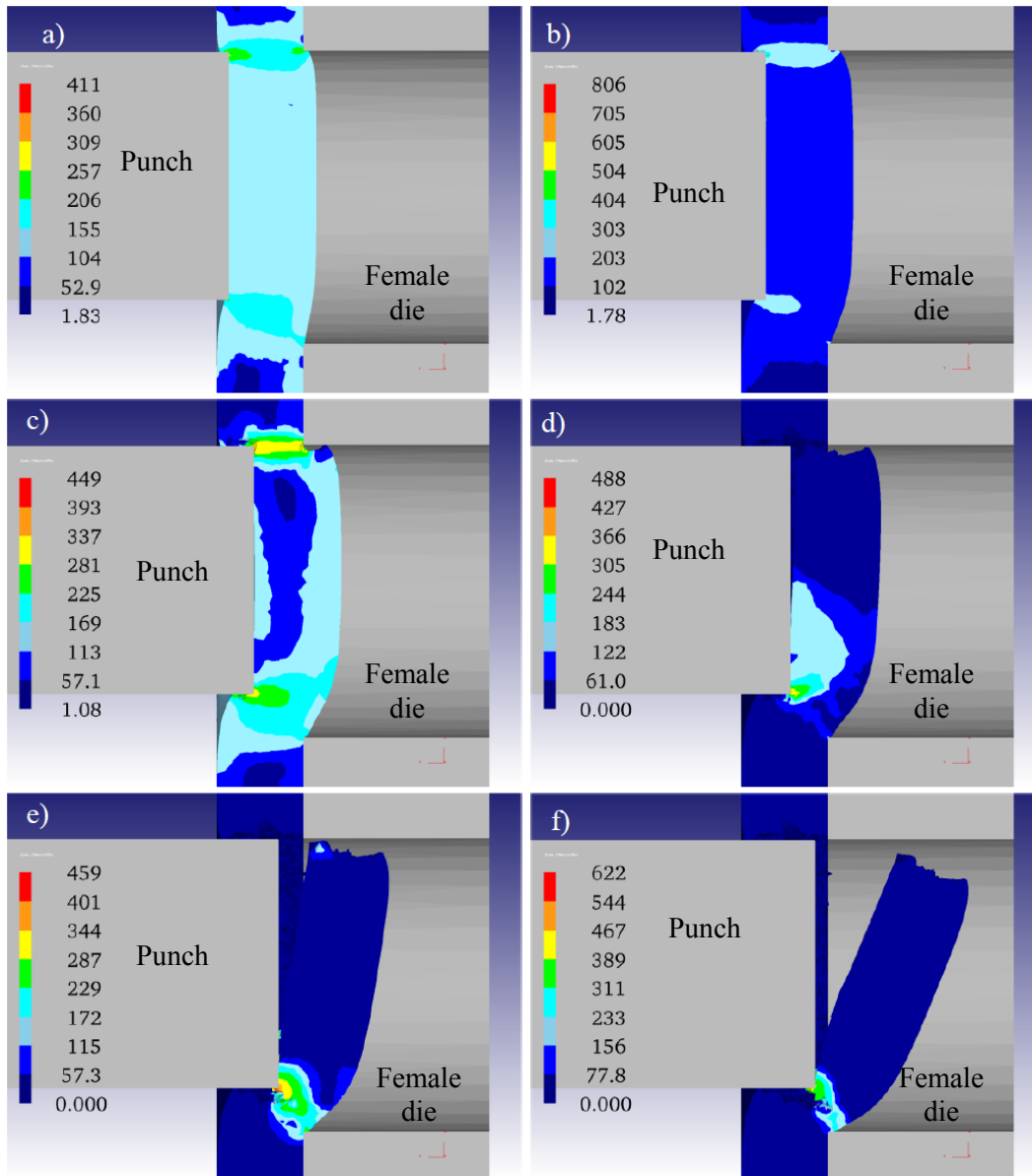


Figure 6.31 Stress (MPa) distribution plot for misaligned punch at punch strokes of a) 10 μm , b) 20 μm , c) 30 μm , d) 40 μm , e) 50 μm , and f) 60 μm .

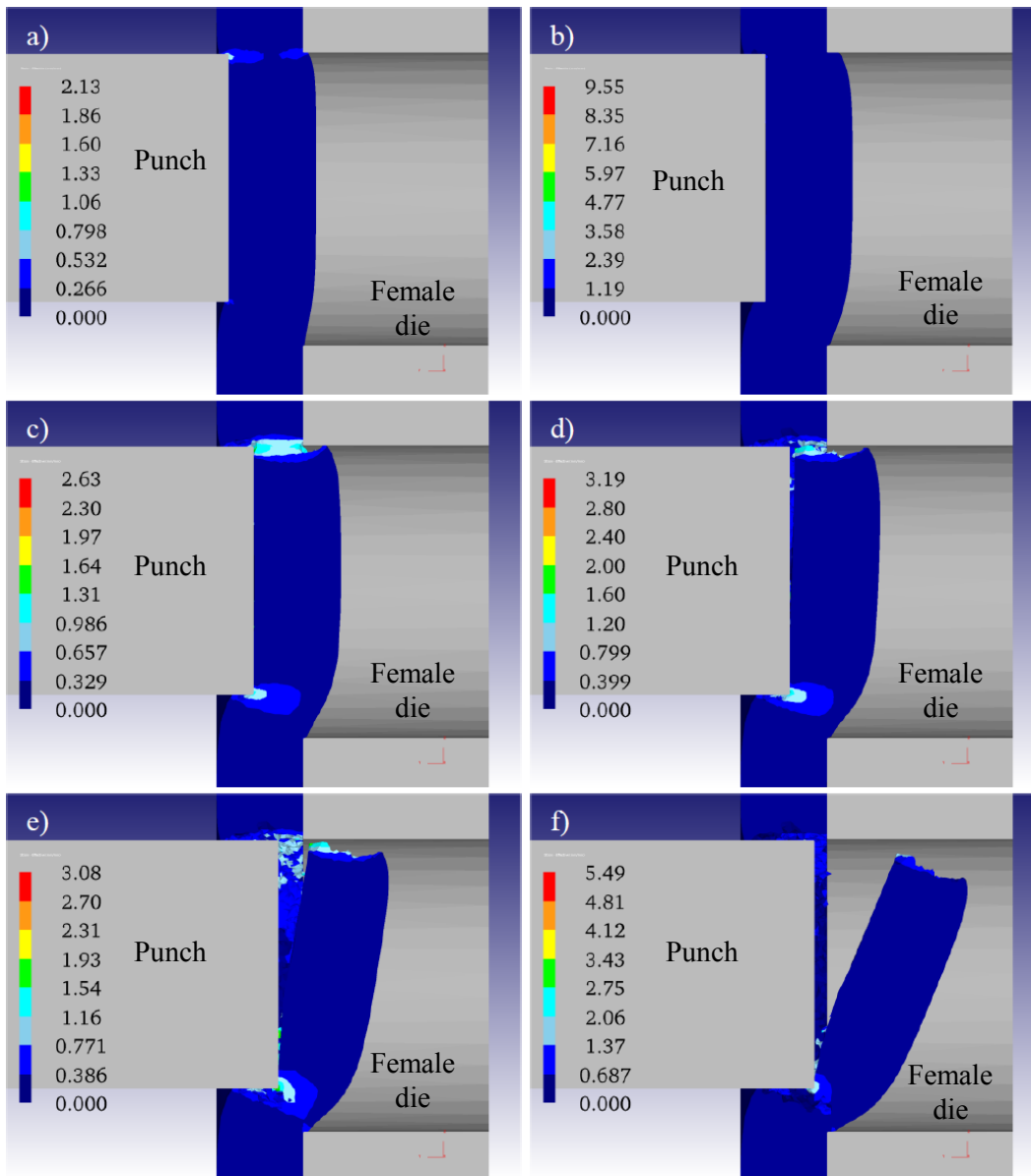


Figure 6.32 train distribution plot for misaligned punch at punch strokes of a) 10 μm , b) 20 μm , c) 30 μm , d) 40 μm , e) 50 μm , and f) 60 μm .

An important objective of this research is to demonstrate the predictive capability of a micropunching finite element simulation. Therefore, the measured peak punching forces for all experimental cases are compared with the simulated results, Figure 6.33.

The simulation was conducted with the material model derived from experimental results of compression testing, Chapter 5. In order to incorporate variations of material parameters in the model, and to see the effect on simulation results, the simulations were carried out at two additional Strength Coefficients; one representing the upper bound of the flow stress and one representing the lower bound of the flow stress. Figure 6.33 and Figure 6.34 show the comparison of measured and simulated peak punching force for a material thickness of 40 μm and 70 μm , respectively.

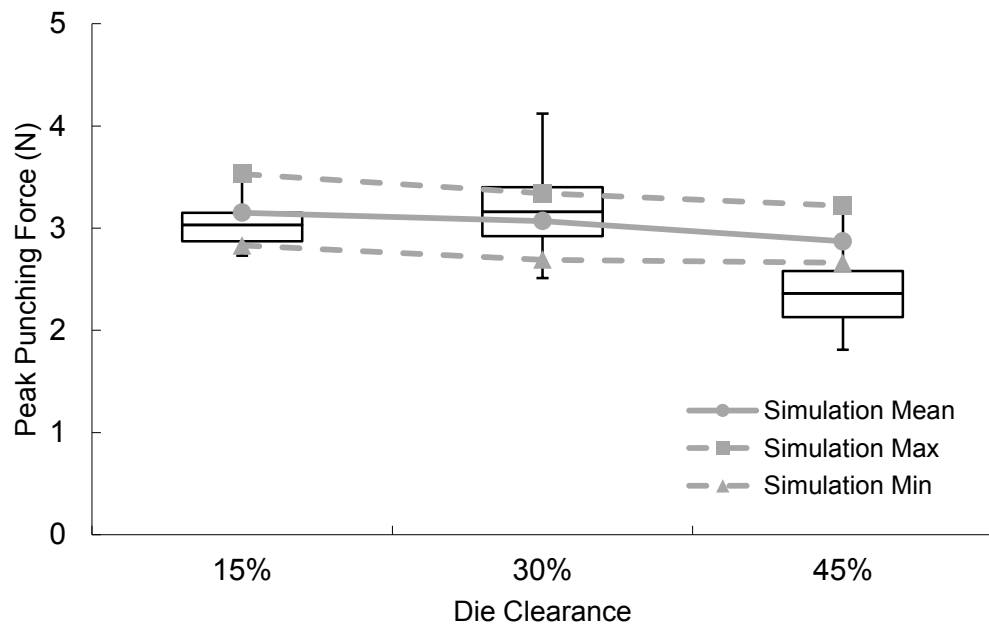


Figure 6.33 Comparison of measured and simulated peak punching force for film thickness of 40 μm

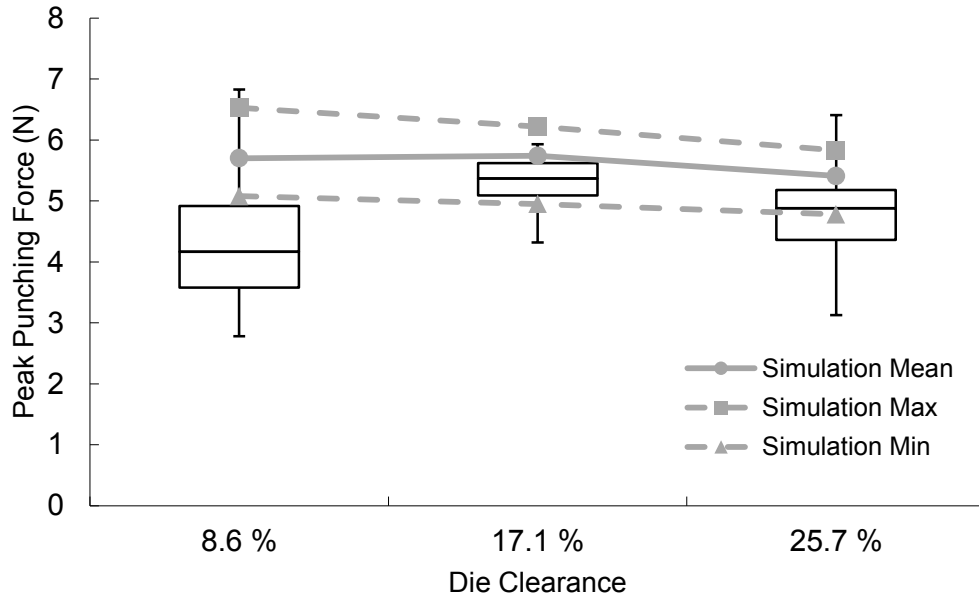


Figure 6.34 Comparison of measured and simulated peak punching force for film thickness of 70 μm

Regarding the box plots in Figures 6.33 and 6.34, the three horizontal lines of the box represent 1st quartile, median, and 3rd quartile, respectively. The whiskers are extended to 1.5 times the interquartile range (3rd quartile – 1st quartile) below the 1st quartile and above the 3rd quartile. If any data point exits outside the whisker ends, they are regarded as outliers and are not plotted. If the minimum or the maximum value data is not an outlier, the whisker is extended to that data point.

6.4. Discussion

When designing a die set, it is important to know how the peak punching force varies with die clearance. It is difficult to maintain small die clearances in both the setup and use of micropunching equipment. From Figure 6.34, it is clear that peak punching force in 70 μm thick PCL film is relatively low for 8.6 % die clearance as compared with 17.1% die clearance. However, the force seems to decrease slightly as the clearance

increases to 25.7%. Similarly, for 40 μm thick PCL, the reduction of peak punching force was observed while going from 30% to 45% die clearance.

The reason for this reduction of peak punching force can be explained by incomplete punching due to die misalignment. For higher clearance micropunching, particularly for cryogenic conditions, die misalignment is encountered quite frequently. This results in opening of the hole from one side, Figure 6.30, rather than axisymmetric shearing of the film.

Incomplete punching at high clearance results in a reduction of the measured peak punching force, but the force still remained close to what is predicted from finite element simulation where the opening is axisymmetric. In order to further investigate, a misaligned punching process was simulated as shown in Figure 6.31 and 6.32. Here, the simulated peak punching force still remained close to what was obtained from a well aligned punching simulation.

The stress and strain distribution plots for 70 μm thick PCL films show that at 30 μm of punch stroke, the crack has already initiated from the punch tip for all three die clearances. However, the crack propagation from the female die tip differs significantly with die clearance. For example, at 8.6 % die clearance, the crack from the female die tip has already propagated, for 17.1 % die clearance, the crack has just initiated from the female die tip, and for 25.7 % die clearance, the crack has not yet started from the female die tip. Also, the strain distribution plots show a significant reduction of effective strain values near the female die tip as the die clearance increases at the same punch stroke length.

Similarly, the stress distribution plots for 40 μm thick PCL films show that for 15% die clearance at 15 μm punch stroke length, cracks appear from both the male and

the female die tips. However, for the same punch stroke, at 30% die clearance, cracks appear from only the male die tip, and for 45% die clearance, there are no cracks from either of the die tips. As expected, for a 40 μm thick film, a reduction of effective strain is observed as the die clearance increases.

The comparison of measured and predicted peak punching force, as shown in Figure 6.34 for 70 μm film thickness, reveals that at low clearance the finite element simulation overestimates the peak punching force and becomes more accurate as the die clearance increases. In fact, the lower bound of the predicted peak punching forces matches closely with the measured values at 17.1% and 25.7% clearance. For micropunching of 40 μm thick PCL films, the predicted peak punching force matched closely for 15% and 30% of die clearance, but over estimates the punching force for 45% die clearance.

Although finite element simulation results do not show a minima or maxima in peak punching force, it seems likely that the predicted punching force decreases gradually as the die clearance increases, which was also observed for copper foil punching. However, from the measured peak punching force, it can be concluded that a smaller die clearance will result in a lower peak punching force. Clearly, in all cases, a higher die clearance is susceptible to die misalignment, resulting in incomplete punching.

6.5. Conclusion

- i. Peak punching force was measured and compared with predicted values from finite element simulation for micro holes of a nominal diameter of 200 μm in 40 μm and 70 μm thick PCL films with three different die clearances.
- ii. The predicted peak punching forces were close to the measured values for most cases. For 40 μm thick PCL film and 15 % die clearance, the error

between measured and predicted peak punching force was approximately 2 %. However, for the case with 70 μm film thickness and 8.6 % of die clearance, the error was approximately 31 %.

- iii. The finite element simulations did not predict an optimal die clearance to minimize peak punching force. However, the measured peak punching forces demonstrated that a smaller die clearance will result in a lower punching force for the range of die clearances investigated (8.6% to 45%).
- iv. Micropunching at high clearance may lead to incomplete punching due to die misalignment.

Chapter 7

Porosity Analysis of 2D Polycaprolactone Membranes

7.1. Introduction

To create a synthetic 3D tissue scaffold by multilayer stacking, 2D porous membranes require a well engineered hole pattern. To achieve the desired microvascular network, it may also be suitable to create a random distribution of holes with sufficiently high porosity to facilitate the natural formation (tubulogenesis) of micro channels. In either case, knowledge is required to determine material and manufacturing constraints when attempting to achieve the closest proximity of two neighboring micro-holes i.e. determining a minimum web thickness.

The minimum distance between two holes is governed by either an immediate material failure due to tearing of the adjoining web or the bulk material properties of the porous membrane become too degraded to withstand the tensile forces imparted during handling. Membrane tensile stresses can be imparted during the micropunching process as the material is stretched over the female die, thereby eliminating the need for a hold down (stripper) plate, or during the subsequent stacking, alignment, and bonding of membrane layers to create a 3D construct.

The goal of the research summarized in this chapter is to investigate the maximum porosity that can be achieved in PCL membranes just prior to failure of the web between adjacent holes as a result of shear forces and surface tension. The research

approach taken is to conduct FE simulations of 70 μm thick PCL membranes at various die clearances while maintaining a constant punch diameter of 200 μm . The simulations are then verified by experiment, where the minimum web thickness is compared to predicted results through inspection of SEM images. Finally, an analytical framework is proposed to predict an upper bound for the maximum porosity level achievable to withstand in-plane tension as a result of membrane handling.

Membrane porosity p is defined as the ratio of open to closed surface area, with porosity often stated as a percentage. For typical tissue engineering applications, it is desirable to achieve a porosity level well above 50% so as to maximize the number of home sites available for cell differentiation and growth, while concurrently minimizing the volume of material susceptible to biodegradation.

Considering the spatial geometry of a 2D membrane hole pattern, web thickness f refers to the minimum web thickness, which occurs along the centerline of two adjacent holes, Figure 7.1.

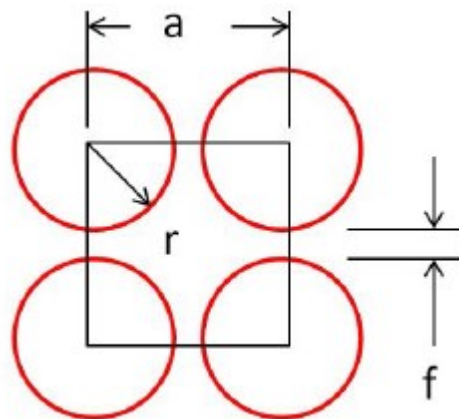


Figure 7.1 A membrane with holes arranged in a squared pattern. The minimum web thickness is defined by f .

The distance between two adjacent holes a in a square hole pattern can be written as a function of hole radius r and web thickness according to

$$a = 2r + f \quad (7.1)$$

By definition, the porosity follows as

$$p = \frac{\pi r^2}{a^2} \quad (7.2)$$

Substitution of Equation 7.1 into Equation 7.2 results in an expression for membrane porosity for a square pattern of holes, Figure 7.1, in terms of the manufacturing parameters i.e. punch radius and desired web thickness,

$$p = \frac{\pi r^2}{(2r + f)^2} \quad (7.3)$$

According to Equation 7.3, porosity of a membrane is roughly dependent on the square of web thickness and reaches its maximum value as the web thickness approaches zero.

$$p_{max,square} = \frac{\pi}{4} \approx 78.5\% \text{ porosity} \quad (7.4)$$

From a purely geometric standpoint, the maximum porosity increases from 78.5% to 90.7% when the relative positioning of a row of holes is shifted, transforming a square pattern of holes into a nested pattern of holes i.e. a “close pack” or “hexagonally-close-packed” (HCP) arrangement. However, the geometric maximum porosity level is not achievable due to web failure during the micropunching process.

The initiation of catastrophic web failure is dependent upon both the material properties of the biocompatible, biodegradable membrane and the stresses induced during the micropunching process. Through FE modeling, as verified by experiment, it is possible to predict a minimum web thickness during cryogenic micropunching of PCL.

7.2. Materials and Methods

7.2.1. Micropunching in PCL

Similar to the previous study on peak punching force, micropunching is conducted with a 200 μm diameter punch in 70 μm thick PCL membranes for three die clearances (8.6%, 17.1%, and 25.7%). The various die clearances are obtained by using a female die with three different hole diameters. All punching is done with the same punch due to a lack of appreciable wear as verified by SEM.

After punching each hole, a precision micrometer controlled stage, Figure 6.5, is adjusted to linearly translate the material holder a prescribed distance. This method results in the fabrication of a linear pattern of holes, where the spacing between adjacent holes is reduced incrementally until web tearing is observed. For experiments, the center distance between adjacent holes is reduced by 10 μm increments after each successive punching cycle.

7.2.2. Finite Element Modeling

A FE model exhibiting half symmetry is developed with a 200 μm diameter hole prefabricated and meshed in a virtual 70 μm thick PCL workpiece, Figure 7.2. The model facilitated an analysis of web stresses and fracture during the cryogenic micropunching simulation of an adjacent 200 μm diameter hole.

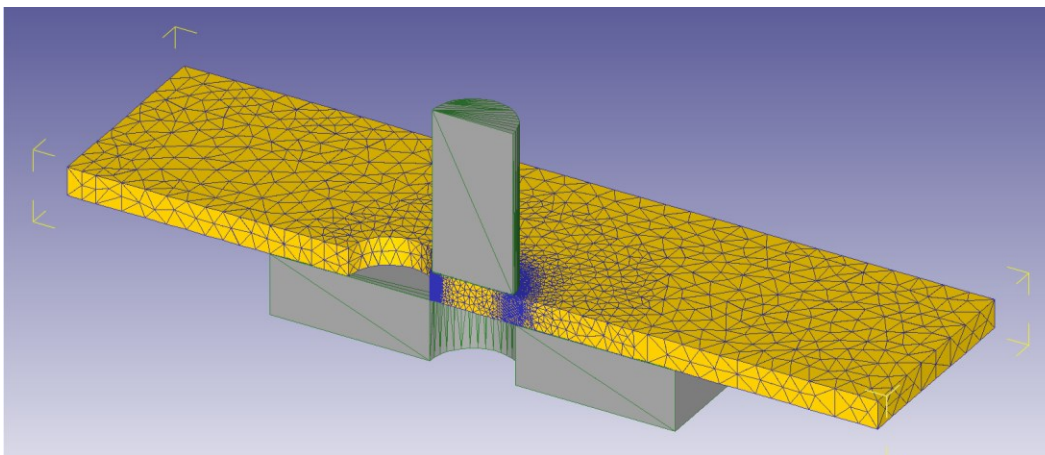


Figure 7.2 Finite element model used to simulate micropunching a 200 μm hole adjacent to a pre-existing hole (70 μm thick PCL)

The same boundary conditions and material model are employed as previously described in Chapter 6 for simulations of peak punching force. However, to accommodate the additional hole, the workpiece size is increased from 1 mm square to a rectangular strip with a width of 1 mm and a length of 2 mm, resulting in an increase of average simulation time from 1 hour to 4 hours.

As in the experiment, simulated web thickness is gradually reduced by decreasing the distance between the centers of the pre-existing hole and the new hole being punched. Having conducted the experiments prior to the simulations, it was apparent that the analysis of web stress should begin when the web thickness is less than or equal to approximately 20 μm .

7.3. Results

Micropunching holes in a linear pattern, with progressively smaller hole spacing, is investigated by taking SEM images. Figure 7.3 shows a linear pattern of holes from a

200 μm diameter punch in a 70 μm thick PCL membrane that was fabricated with 8.6 % die clearance.

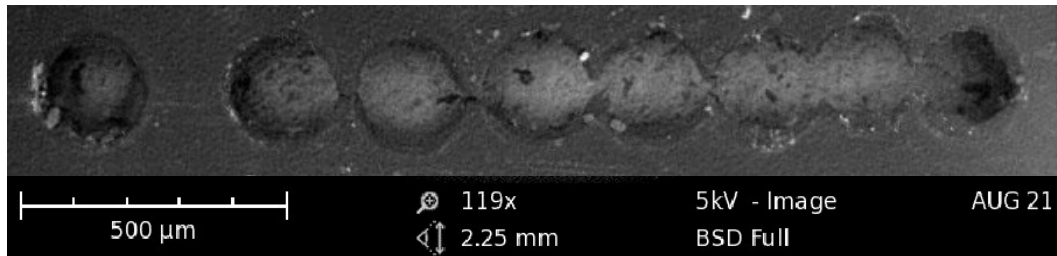


Figure 7.3 Test case for 8.6% die clearance showing a linear pattern of micropunched holes to observe web tearing as the holes are punched progressively closer together (200 μm punch, 70 μm thick PCL)

Similarly, Figure 7.4 is an SEM image of a linear pattern of holes for a 17.1% die clearance.

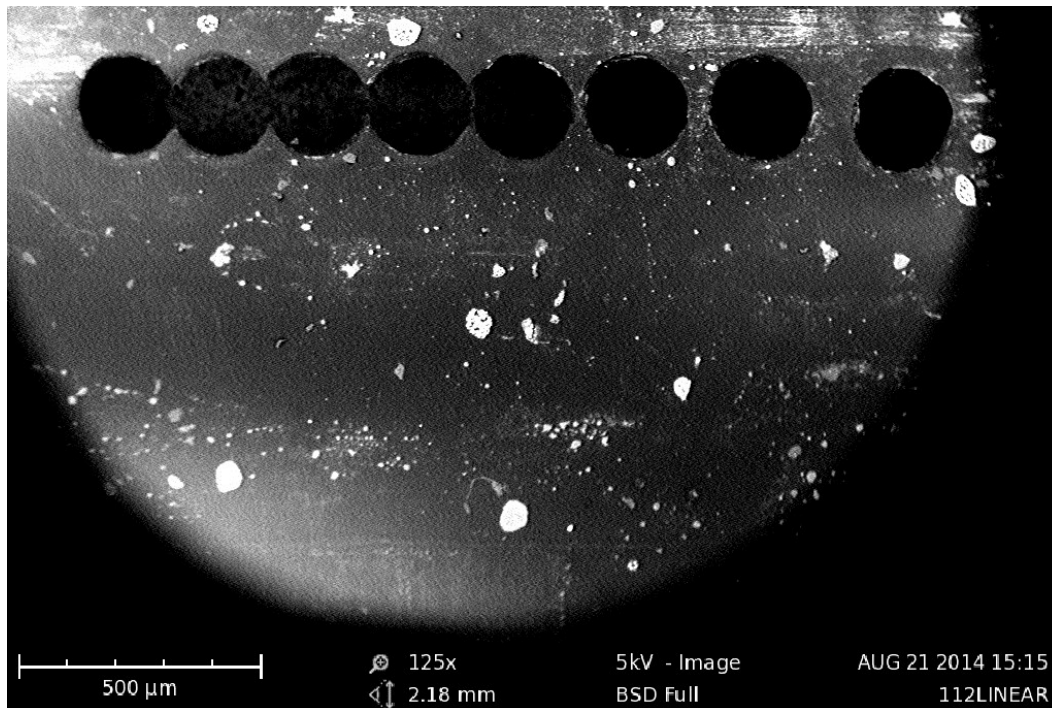


Figure 7.4 Test case for 17.1% die clearance showing a linear pattern of micropunched holes to observe web tearing as the holes are punched progressively closer together (200 μm punch, 70 μm thick PCL)

Micropunching experiments with 25.7% die clearance resulted in incomplete holes being formed, Figure 7.5, as the punch-out remained tethered to the membrane surface. However, web tearing with reduced spacing between two adjacent holes is observable from the SEM image. Notably, consistency in the location of the sheared edge of the hole is indicative of die misalignment, Figure 7.5.

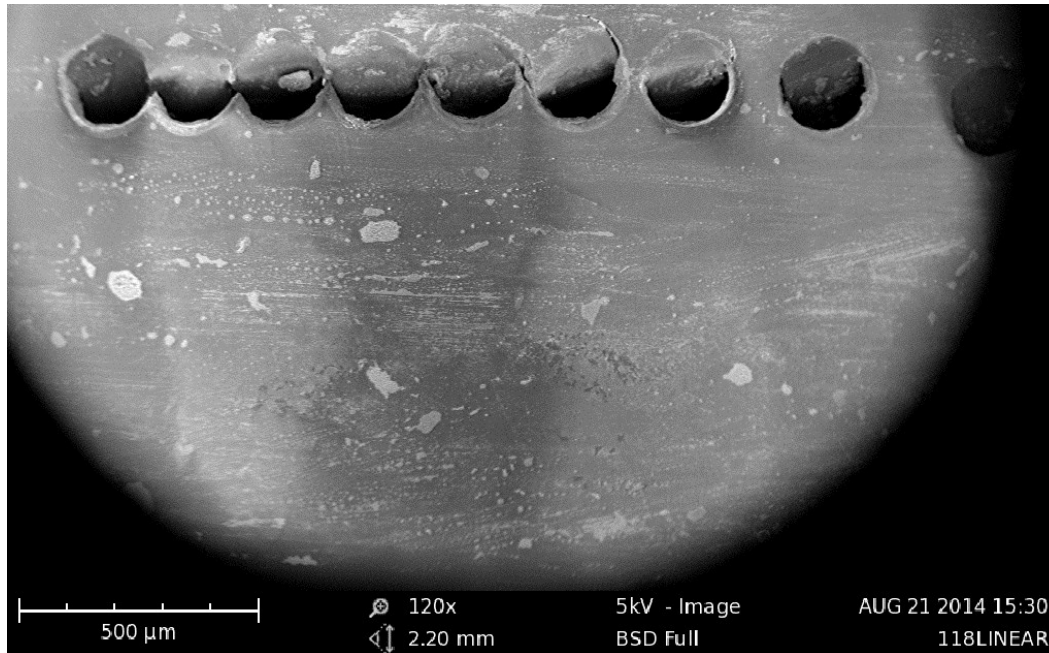


Figure 7.5 Test case for 25.7% die clearance showing a linear pattern of micropunched holes to observe web tearing as the holes are punched progressively closer together. Partial shearing was observed, with a geometric consistency indicative of die misalignment (200 μm punch, 70 μm thick PCL).

Upon inspection of the SEM results at higher magnification, images reveal web tearing as the web thickness is reduced. For example, considering a punch center-to-center distance of 230 μm (nominal web thickness of 30 μm), complete fracture of the web is not observed over the range of die clearances tested. However, as the center distance between two successive holes is reduced to 220 μm (nominal web thickness of 20 μm), web fracturing occurs. SEM images for a 30 μm thick web at 8.6% and 17.1%

die clearance are shown in Figure 7.6 and 7.7, respectively. Similarly, the results for a 20 μm thick web at 8.6% and 17.1% die clearances are shown in Figures 7.8 and 7.9, respectively. Results for 25.7% die clearance are not shown due to incomplete holes.

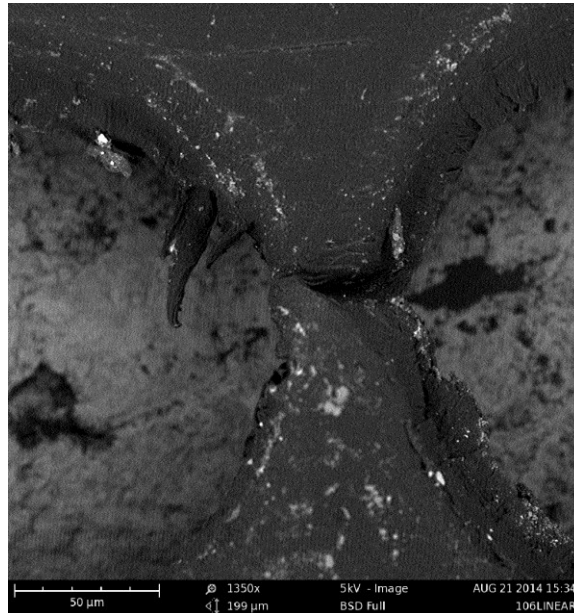


Figure 7.6 Partially fractured, but unbroken web for 8.6% die clearance and a center-to-center hole distance of 230 μm resulting in a nominally 30 μm thick web (70 μm thick PCL)

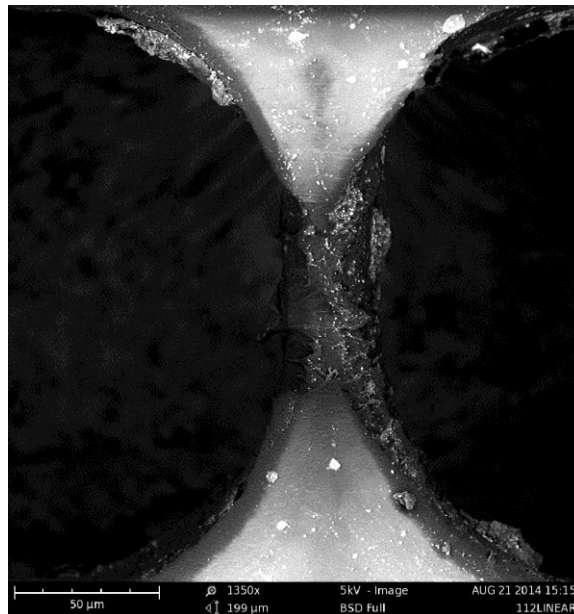


Figure 7.7 Unbroken web for 17.1% die clearance and a center-to-center hole distance of 230 μm resulting in a nominally 30 μm thick web (70 μm thick PCL)

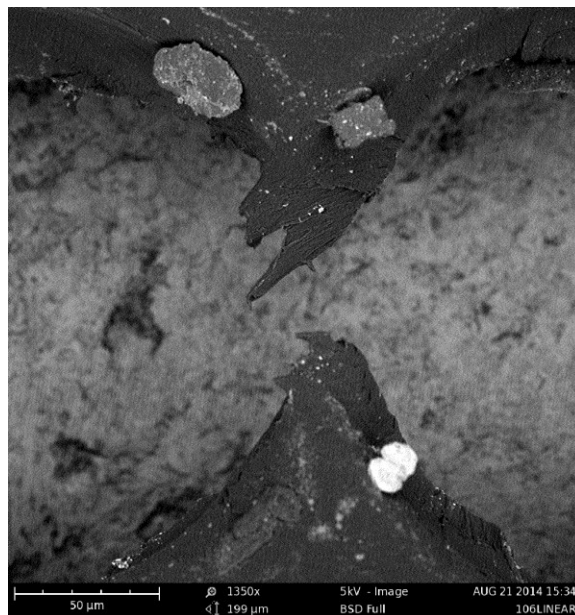


Figure 7.8 Broken web for 8.6% die clearance and a punch center-to-center distance of 220 μm resulting in a nominal 20 μm thick web (70 μm thick PCL)

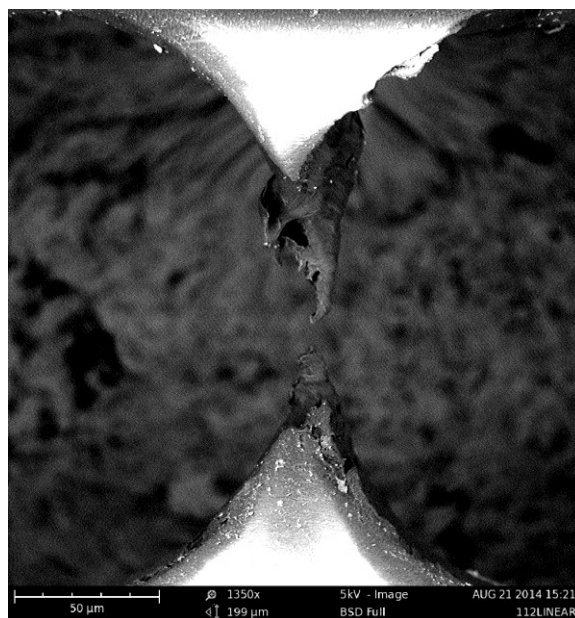


Figure 7.9 Broken web for 17.1% die clearance and a punch center-to-center distance of 220 μm resulting in a nominal 20 μm thick web (70 μm thick PCL)

In order to create a greater breadth of images for comparison of the experimental and FE simulation results, additional punching was carried out for punch center-to-center distances less than required to initiate web fracture. Specifically, while holding die clearance constant at 8.6%, center distances of 210 μm , 200 μm , and 190 μm , were investigated. A nominal web thickness of 10 μm is expected for a punch center-to-center distance of 210 μm , whereas a distance of 200 μm produces a line-on-line condition, and a center distance of 190 μm causes the hole diameters to overlap by 10 μm . SEM images of the fractured webs, corresponding to these three punching conditions, are shown in Figures 7.10 to 7.12.

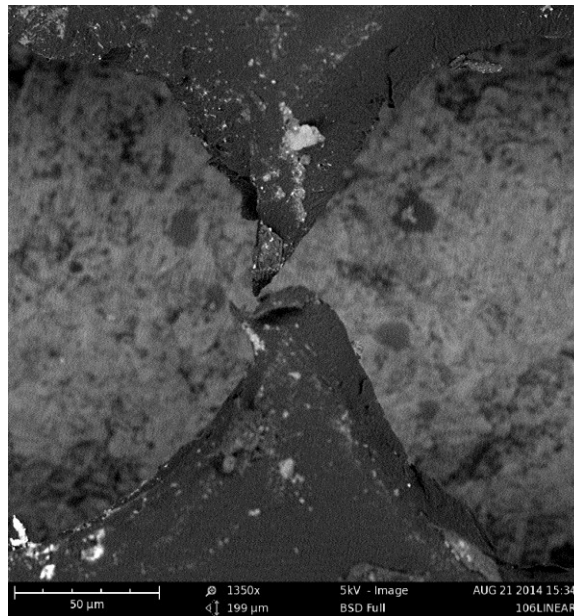


Figure 7.10 Fractured web for punch center-to-center distance of 210 μm , resulting in a nominal web thickness of 10 μm (8.6% die clearance, 70 μm thick PCL)

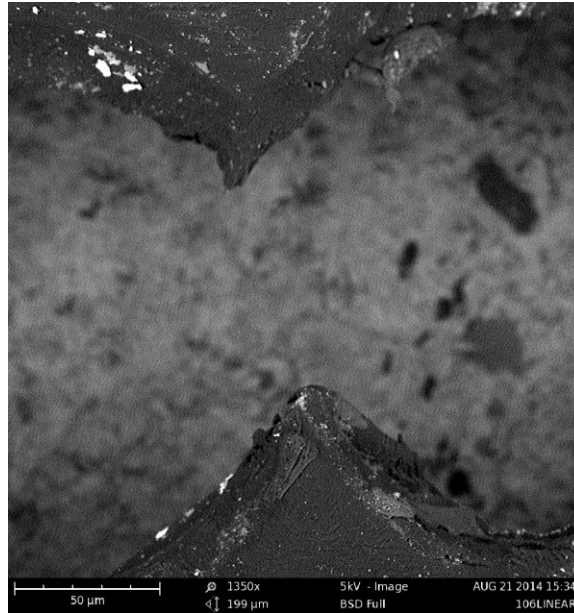


Figure 7.11 Fractured web for punch center-to-center distance of 200 μm , resulting in a line-on-line condition between adjacent holes (8.6% die clearance, 70 μm thick PCL)

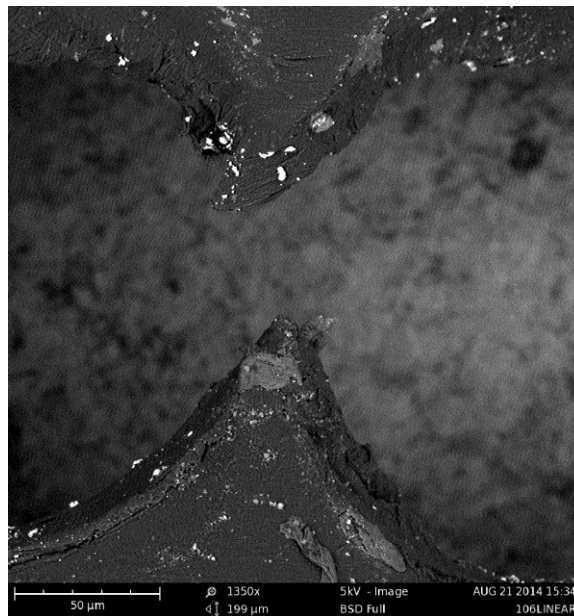


Figure 7.12 Fractured web for punch center-to-center distance of 190 μm , resulting in 10 μm overlap along the center line between adjacent holes (8.6% die clearance, 70 μm thick PCL)

Figure 7.13 to 7.15.

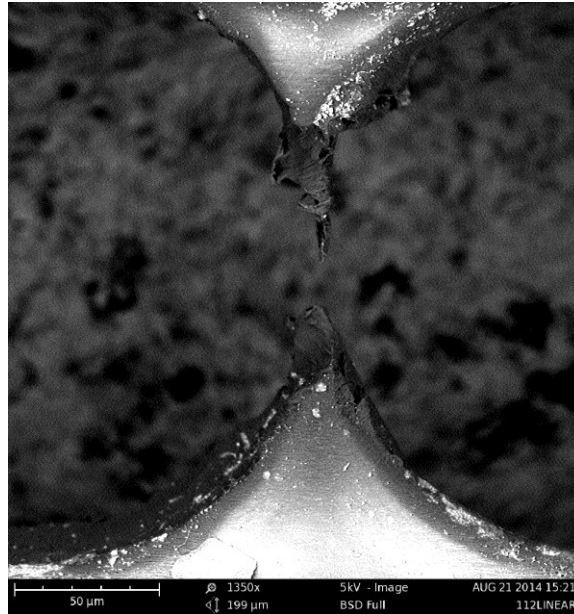


Figure 7.13 Fractured web for punch center-to-center distance of 210 μm , resulting in a nominal web thickness of 10 μm (17.1% die clearance, 70 μm thick PCL)

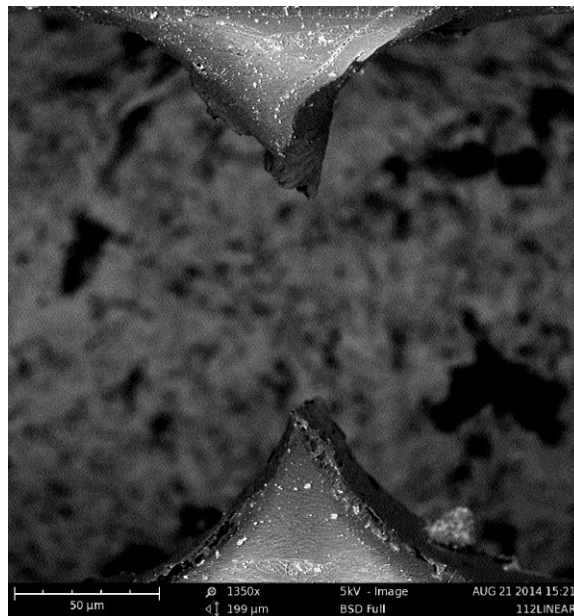


Figure 7.14 Fractured web for punch center-to-center distance of 200 μm , resulting in a line-on-line condition between adjacent holes (17.1% die clearance, 70 μm thick PCL)

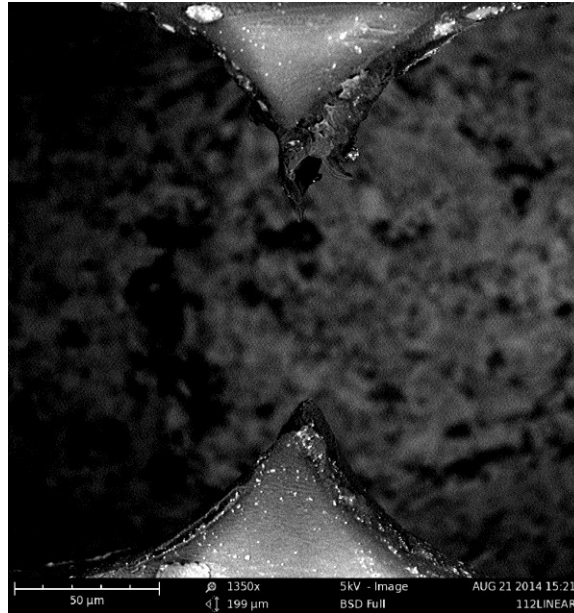


Figure 7.15 Fractured web for punch center-to-center distance of 190 μm , resulting in 10 μm overlap along the center line between adjacent holes (17.1% die clearance, 70 μm thick PCL)

Summarizing the experimental phase, successive holes were punched to create nominal web thicknesses of 30 μm , 20 μm , 10 μm , 0 μm (line-on-line), and -10 μm (overlapping holes). This was accomplished by moving the material holder in increments of 10 μm while successively punching holes. Tolerance on the nominally prescribed web thickness is estimated to be +/- 2 μm based on micrometer control of the material translation stage. Results from the experiments are summarized in Table 7.1.

Table 7.1 Summary of experimental results (200 μm diameter holes, 70 μm thick PCL)

Die Clearance (%)	Center-to-Center Hole Distance (μm)	Minimum Web Thickness (μm)	Web Fracture Observed?
8.6	230	30	No
8.6	220	20	Yes
8.6	210	10	Yes
8.6	200	0	Yes
8.6	190	-10 (overlapping)	Yes
17.1	230	30	No
17.1	220	20	Yes
17.1	210	10	Yes
17.1	200	0	Yes
17.1	190	-10 (overlapping)	Yes
25.7	230	30	No
25.7	220	20	Yes
25.7	210	10	Yes
25.7	200	0	Yes
25.7	190	-10 (overlapping)	Yes

Following the experimental phase, simulations were carried out to determine the predictive capability of the FE model. Similar to the terminology used in the experimental phase, “center-to-center” now refers to the distance between the axis of the preexisting hole and the axis of the punch, Figure 7.16.

Unlike the experimental phase, there are no tolerance constraints when simulating the micropunching process. As such, simulations were run for center-to-center distances in increments of less than 10 μm , with a focus on determining more precisely the web thickness where fracture is first initiated.

The FE simulations correlated quite well with experiments. Regardless of die clearance, simulations predicted web failure when the minimum web thickness approached 20 μm . The results are summarized in Table 7.2.

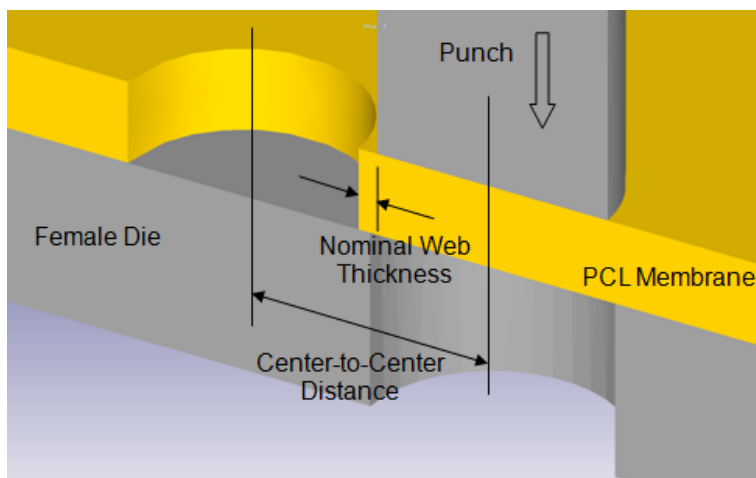


Figure 7.16 Model geometry for the finite element simulation of micropunching a hole adjacent to a preexisting hole

Table 7.2 Summary of FE simulation results (200 μm diameter holes, 70 μm thick PCL)

Die Clearance (%)	Center-to-Center Hole Distance (μm)	Minimum Web Thickness (μm)	Web Fracture Simulated?
8.6	223	23	No
8.6	216	16	Yes
8.6	210	10	Yes
8.6	200	0	Yes
8.6	190	-10 (overlapping)	Yes
17.1	230	30	No
17.1	222	22	Nearly
17.1	217	17	Yes
17.1	210	10	Yes
25.7	223	23	No
25.7	218	18	Yes

The method of element elimination was a successful technique for predicting the resulting web geometry by simulation. For example, in the case of a center-to-center distance of 210 μm (10 μm nominal web thickness) the simulated web geometry and the SEM image from experiment at 8.6% die clearance are very comparable, Figures 7.17(a) and 7.17(b), respectively .

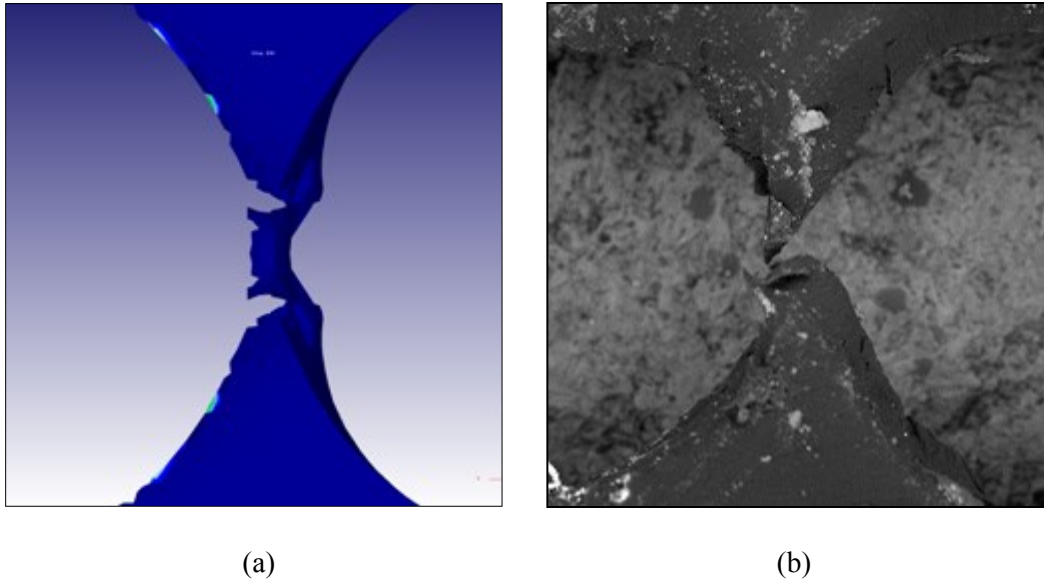


Figure 7.17 Comparison of (a) simulated geometry from FE model and (b) SEM image from experiment for adjacent micro-hole punching at a center-to-center distance of $210\ \mu\text{m}$ with a die clearance of 8.6% (nominal $10\ \mu\text{m}$ web thickness, $70\ \mu\text{m}$ thick PCL)

In another example, the simulated geometry of the line-on-line micropunching case and the SEM images from the experiment for 8.6% die clearance are also very comparable, Figure 7.18(a) and 7.18(b), respectively.

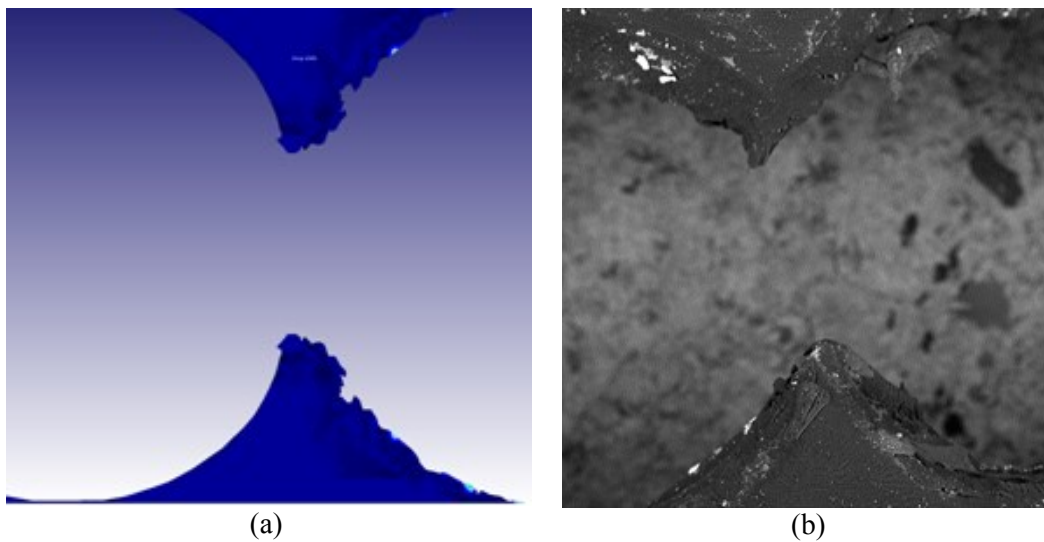


Figure 7.18 Comparison of (a) simulated geometry from FE model and (b) SEM image from experiment for adjacent micro-hole punching at a center-to-center distance of $200\ \mu\text{m}$ (line-on-line condition) with a die clearance of 8.6% ($70\ \mu\text{m}$ thick PCL)

A cross sectional view of the simulated hole geometry reveals the stress distribution and the extent of punch travel prior to complete fracture of the punch-out. In general, at 8.6% die clearance, shear of the punch-out occurs first on the side of the hole opposite the web.

Figure 7.19 shows the stress distribution in cross section after the punch has traveled 30 μm into the surface of the 70 μm thick PCL membrane. At this point, the punch-out is still attached to the bulk material around the full circumference of the hole. However, as the punch advances to a depth of 40 μm , the punch-out is sheared completely from the side wall opposite the web, Figure 7.20.

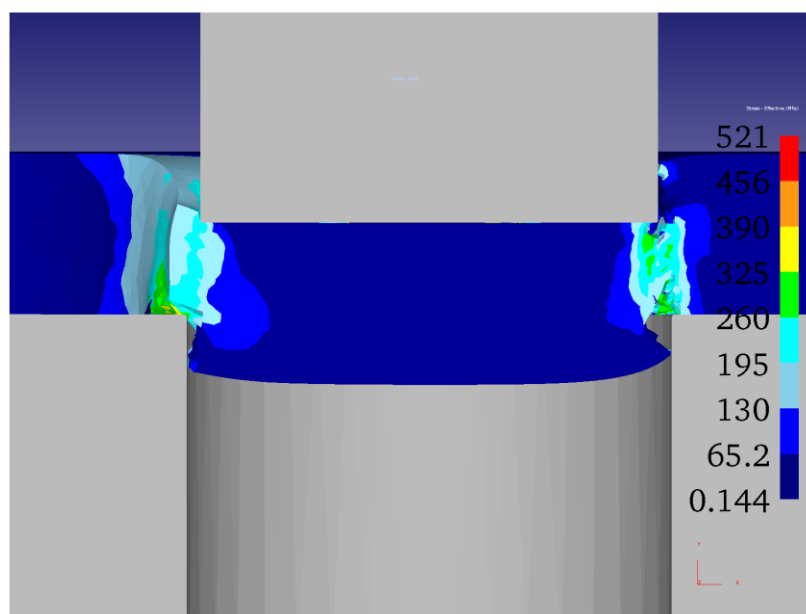


Figure 7.19 Stress (MPa) distribution plot of the cross section during adjacent punching at center to center distance of 210 μm with die clearance of 8.6 % at punch stroke length of 30 μm

At 8.6% die clearance, complete shearing of the punch-out is observed after the punch has traveled approximately two thirds through the material thickness. The required stroke length for complete shear is extended to nearly material thickness for 17.1% die clearance and as observed, at 25.7% die clearance the gap between the male

and female die ($18\ \mu\text{m}$) is often too large for complete shearing to occur at full stroke length i.e. when stroke length is equivalent to material thickness.

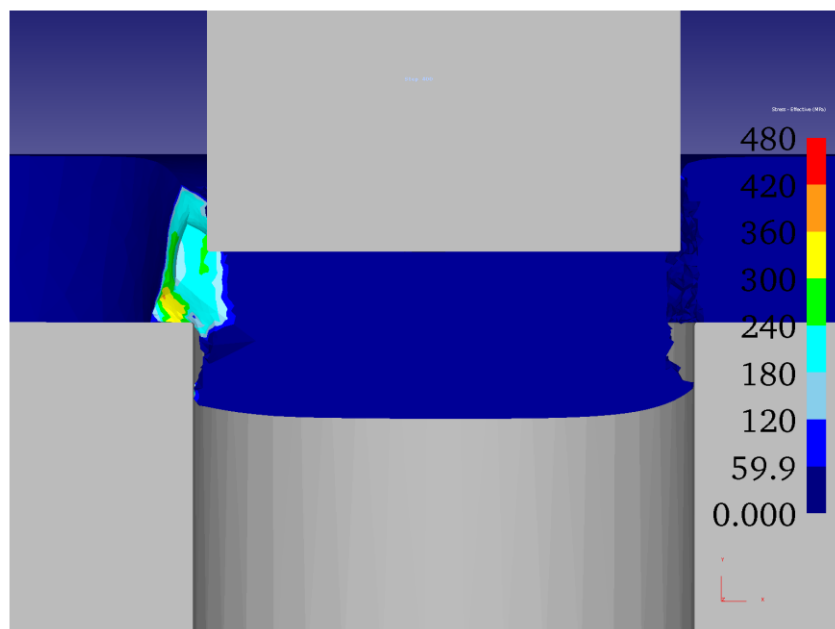


Figure 7.20 Stress distribution plot of the cross section during adjacent punching at center to center distance of $210\ \mu\text{m}$ with die clearance of 8.6 % at punch stroke length of $40\ \mu\text{m}$

Simulations at 17.1% die clearance were also comparable to the web geometry observed in analysis of SEM images from micropunching experiments. Figure 7.21 compares the results when the center-to-center distance is $230\ \mu\text{m}$ ($30\ \mu\text{m}$ nominal web thickness). In both the experiment and in the simulation, the web between adjacent holes remains intact.

As the nominal web thickness is reduced to $10\ \mu\text{m}$, with a center-to-center distance of $210\ \mu\text{m}$, web fracture occurs in both the experiment and in the simulation. For this case, the predicted and actual web geometry is quite comparable as shown in Figure 7.22.

By refining the increment of distance between the punched holes, the FE simulation predicts that web failure is first initiated at a minimum web thickness of

approximately $22\ \mu\text{m}$ for a die clearance of 17.1%, Table 7.2. This corresponds to a porosity of 63.7% for a square hole pattern, Equation 7.3. The stress field can be observed to extend well beyond the punch perimeter and into the web, Figure 7.23.

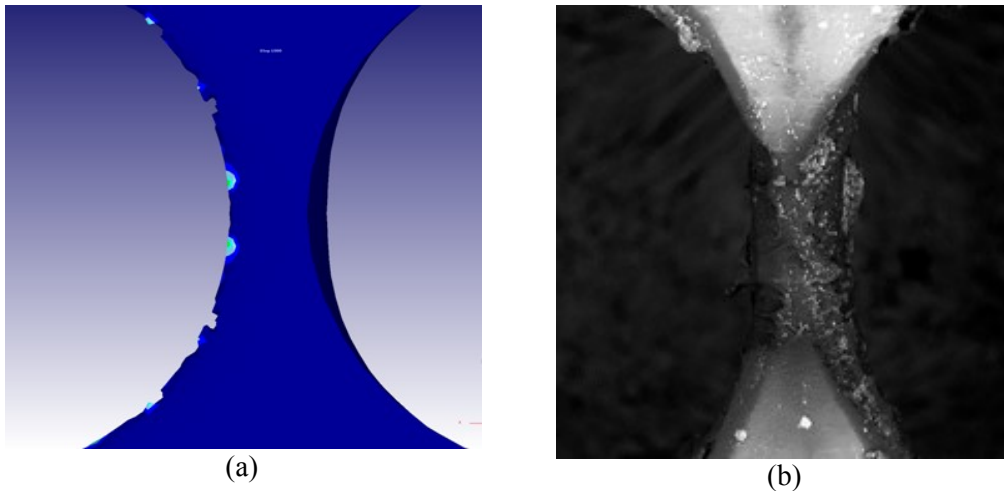


Figure 7.21 Comparison of (a) simulated geometry from FE model and (b) SEM image from experiment for adjacent micro-hole punching at a center-to-center distance of $230\ \mu\text{m}$ ($30\ \mu\text{m}$ nominal web thickness) with a die clearance of 17.1% ($70\ \mu\text{m}$ thick PCL)

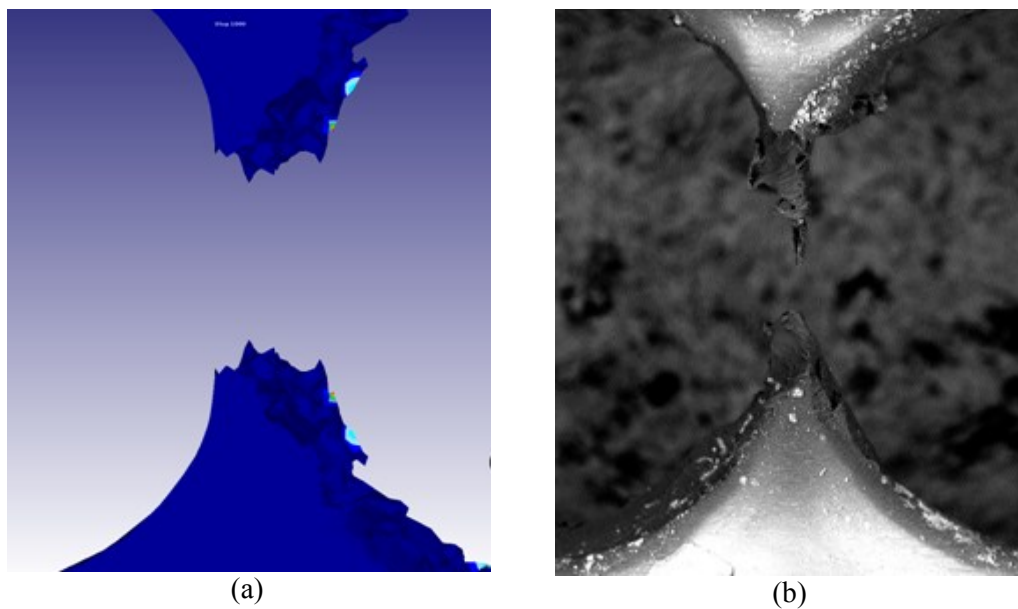


Figure 7.22 Comparison of (a) simulated geometry from FE model and (b) SEM image from experiment for adjacent micro-hole punching at a center-to-center distance of $210\ \mu\text{m}$ ($10\ \mu\text{m}$ nominal web thickness) with a die clearance of 17.1% ($70\ \mu\text{m}$ thick PCL)

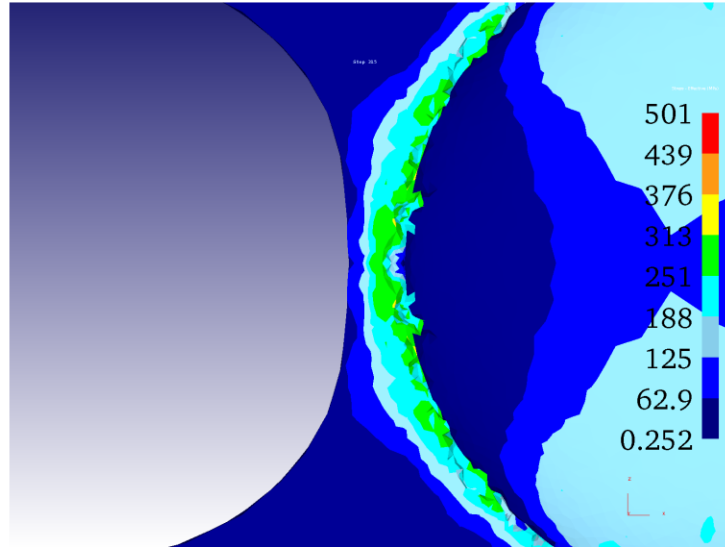


Figure 7.23 Stress (MPa) distribution plot of the web during adjacent punching at a enter-to-center distance of 222 μm with die clearance of 17.1 % at punch stroke length of 31.5 μm

7.4. Discussion

The objective of this study was to determine maximum achievable porosity and its dependency on die clearance. From the experimental data, it is clear that irrespective of die clearance web tearing starts at around a web thickness of 20 μm . Finite element simulations predict that web tearing occurs for a web thickness of approximately 10 μm to 20 μm .

Based on the simulations and experimental results, a conservative estimation of the minimum web thickness is 20 μm . Note that this is valid only for holes with nominal diameter of 200 μm and a film thickness of 70 μm as considered in this study.

Maximum achievable porosity can be obtained by arranging the holes in a hexagonally-close-packed pattern as shown in Figure 7.24. Porosity, in this case can be calculated as

$$p = \frac{\text{Area of the circles in the Hexagon}}{\text{Total area of the the Hexagon}} \quad (7.5)$$

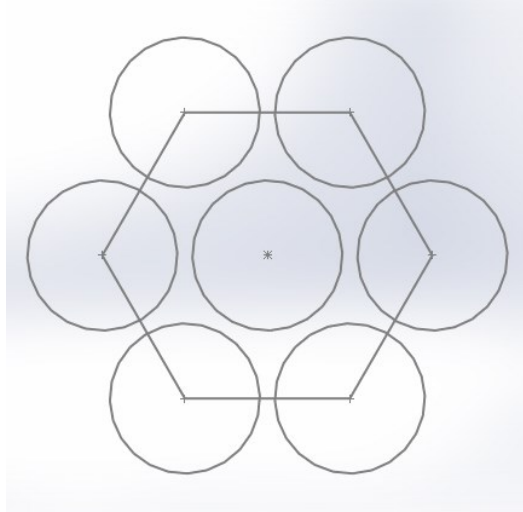


Figure 7.24 Hexagonally-Close-Packed arrangements of holes

Assuming the radius of the circle is r and the web thickness is f , side length of the hexagon is

$$a = (2r + f) \quad (7.6)$$

The area of the hexagon in terms of a can be calculated as

$$A_{hex} = 6 \times \frac{1}{2} \times a \times \frac{a\sqrt{3}}{2} = \frac{3\sqrt{3}}{2} a^2 \quad (7.7)$$

and the area of the circles inside the hexagon by

$$A_{cir} = 3\pi r^2 \quad (7.8)$$

Dividing Equation 7.7 by Equation 7.8, porosity can be calculated as

$$p = \frac{3\pi r^2}{\frac{3\sqrt{3}}{2}a^2} = \frac{2\pi}{\sqrt{3}} \left(\frac{r^2}{a^2} \right) \quad (7.9)$$

Upon substitution of Equation 7.6 into Equation 7.9,

$$p = \frac{2\pi}{\sqrt{3}} \left(\frac{r}{2r+f} \right)^2 \quad (7.10)$$

and after simplification of Equation 7.10, the equation for porosity of a hexagonally-close-packed hole pattern is

$$p = \frac{2\pi}{\sqrt{3}} \frac{1}{\left[2 + \left(\frac{f}{r} \right) \right]^2} \quad (7.11)$$

In the current study, $r = 100 \mu\text{m}$ and $f = 20 \mu\text{m}$. Therefore, the maximum achievable porosity can be calculated as

$$p = \frac{2\pi}{\sqrt{3}} \frac{1}{\left[2 + \left(\frac{20}{100} \right) \right]^2} \approx 0.7495 \quad (7.12)$$

Therefore, it can be concluded that for a nominal hole diameter of $200 \mu\text{m}$ in $70 \mu\text{m}$ thick PCL, the maximum achievable porosity is approximately 75%.

7.5. Maximum Porosity for a Porous Membrane in Tension

In addition to manufacturing limitations that put a ceiling on the maximum achievable porosity, handling of 2D porous membranes without damaging them is also a concern. Here, damage is defined as exceeding the tensile yield point of the material in the webbing between holes.

Assume that during handling of a 2D hexagonally-close-packed membrane, a uniform pressure P is applied along the edges in one direction, Figure 7.25. Let L be the

total length of the membrane perpendicular to the direction of the applied pressure and let t be the thickness of the membrane perpendicular to the planar surface.

The applied pressure will slightly reduce the effective length by reshaping the circles as ellipses, with the major axis of each ellipse in the direction of the applied pressure. For simplicity, neglect the reduction in length and assume that it remains the same as prior to the loading process. Now, by considering any cross section perpendicular to the loading direction, the entirety of the load is transmitted to the thin webs between holes. Provided web thickness is considered quite small as compared to the diameter of the holes, the web stresses are aligned along the loading direction and are uniform. Therefore, the total force applied to the membrane can be written as

$$F = LtP \quad (7.13)$$

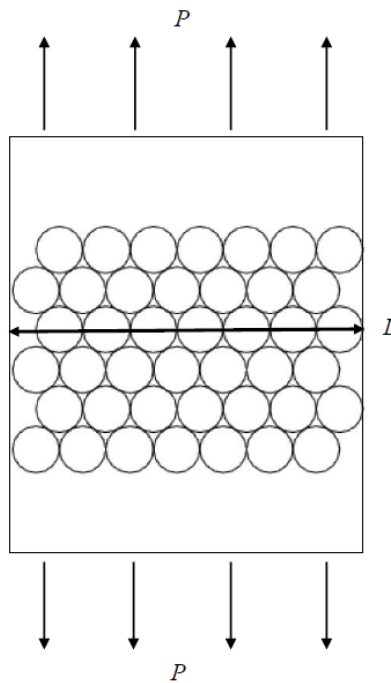


Figure 7.25 A 2D porous membrane under uniaxial loading

This force is balanced by the cumulative web stress across any row of holes. The number of webs across the length L can be written as

$$N = \frac{L}{D} + 1 \quad (7.14)$$

where D is the diameter of the holes. For $L \gg D$, Equation 7.14 can be rewritten as

$$N = \frac{L}{D} \quad (7.15)$$

The cross-sectional area A of each web is

$$A = ft \quad (7.16)$$

where f is the web thickness. The total web cross sectional area can now be written as

$$A_{web} = NA = Nft \quad (7.17)$$

Therefore, web stress can be written as

$$\sigma_{web} = \frac{F}{A_{web}} \quad (7.18)$$

Substituting Equation 7.13 and 7.17 into Equation 7.18,

$$\sigma_{web} = \frac{LtP}{Nft} \quad (7.19)$$

and upon simplification, the web stress can be written as

$$\sigma_{web} = \frac{DP}{f} \quad (7.20)$$

To avoid damaging the membrane as a result of planar tensile forces, the following condition must be met,

$$\sigma_{web} \leq Y_{PCL} \quad (7.21)$$

where Y_{PCL} is the yield strength of PCL at room temperature.

Substituting Equation 7.20 into Equation 7.21, the damage criteria becomes

$$\frac{DP}{f} \leq Y_{PCL} \quad (7.22)$$

and upon solving for web thickness,

$$f \geq \frac{DP}{Y_{PCL}} \quad (7.23)$$

This lower limit of web thickness f is determined by the material yield point Y_{PCL} , the hole diameter D , and the level of pressure P used to handle the 2D membrane.

As previously described, for a 200 μm diameter hole and a 70 μm thick membrane, Equation 7.11 can be used to calculate the maximum achievable porosity – repeated here for convenience.

$$p \leq \frac{2\pi}{\sqrt{3}} \frac{1}{\left[2 + \left(\frac{f_{max}}{r}\right)\right]^2} \quad (7.24)$$

Substituting $f_{max} = \frac{DP}{Y_{PCL}}$ and $D = 2r$, Equation 7.24 becomes

$$p_{max} \leq \frac{2\pi}{\sqrt{3}} \frac{1}{\left[2 + \left(\frac{2P}{Y_{PCL}}\right)\right]^2} \quad (7.25)$$

Equations 7.24 and 7.25 can be used to determine the maximum handling pressure while achieving the desired porosity level for a given hole size.

7.6. Conclusion

- i. Through cryogenic micropunching, a linear pattern of 200 μm diameter holes was fabricated by reducing the web thickness between adjacent holes in 10 μm increments. For a 70 μm thick PCL membrane, it was

determined that web tearing started at a minimum web thickness of approximately 20 μm .

- ii. Finite element simulations of the micropunching process demonstrated that web tearing started at a minimum web thickness of 10 μm to 20 μm , which is in close agreement with what was observed experimentally.
- iii. Finite element simulations demonstrated that there was no dependency of minimum achievable web thickness on die clearances between 8.6% and 25.7%.
- iv. For a membrane that is not subjected to external loading, the maximum achievable porosity for a hexagonally-close-packed arrangement of holes is 75% while micropunching 200 μm diameter holes.
- v. An analytical model was presented to calculate the maximum achievable porosity in the presence of an external tensile load as result of handling.

Chapter 8

Summary

Research was conducted using a newly developed cryogenic micropunching technique to create engineered porosity in Polycaprolactone membranes. The process was simulated using finite element methods and validated using experiments.

8.1. Conclusions

- i. Conventional finite element simulations were validated for their predictive capability in estimating peak punching force while micropunching thin copper foils, eliminating the need for cumbersome crystal plasticity finite element simulations.
- ii. An analytical model was developed to understand the force profile shape while punching with a slanted punch. It was found that the instantaneous punching force is related to the instantaneous creation rate of shear area.
- iii. Material properties of Polycaprolactone were determined for room temperature compression tests, as well as for samples immersed in liquid nitrogen, in order to determine material behavior below the glass transition temperature.
- iv. Experimentally determined material properties of PCL were used to determine the flow stress curve for finite element simulations of the cryogenic micropunching process.

- v. Experiments were conducted to understand if an optimal die clearance results in minimum peak punching force while micropunching Polycaprolactone films. For the range of clearances considered, experimental results showed that punching force reduces slightly with die clearance. However, no minimum was found. Finite element simulations were able to estimate the peak punching force with reasonable accuracy as compared to experiment, but did not show any sign of optimal die clearance for minimum peak punching force.
- vi. Experiments and finite element simulations were in agreement that minimum web thickness between 200 μm diameter adjacent holes in 70 μm thick Polycaprolactone was approximately 20 μm . This minimum web thickness showed no dependency on die clearances between 8.6% and 25.7%. The maximum achievable porosity, for the considered process conditions, was found to be approximately equal to 75% for a hexagonally-close-packed arrangement of holes.
- vii. An analytical model was developed to illustrate the dependency of maximum achievable porosity on the membrane handling forces during multilayer stacking.

8.2. Future Scope

During the course of this research, several new and interesting problems were encountered, a few of which can be considered for future research.

- During the experiments, it was found that many times the dies get misaligned due to repeated cooling and heating of the fixture. At times, this results in a reduction of peak punching force due to incomplete punching. One such case was

simulated and found to mimic the experimental results, which is presented in Chapter 6. A more detailed investigation should be pursued to fully understand misaligned punching as a function of die clearance and material thickness.

- In order to achieve high production volume, the ability to punch multiple holes, simultaneously, is desired. There are serious manufacturing limits to fabricating metal dies for punching multiple micro-scale holes. However, silicon dies can be fabricated using micro-fabrication techniques i.e. masking and etching. It will be interesting to investigate the punching forces and web tearing while simultaneously punching multiple holes. Also, since silicon dies are brittle and more susceptible to failure than metal dies, detailed finite element simulations can be done to estimate die stress and wear, unlike in the current research where the dies are modeled as rigid parts.
- Conventional finite element simulations were able to predict the punching forces while punching copper foils with reasonable accuracy. However, the exact shape and uncertainty in the fractured surface is difficult to predict when the geometry features are of comparable size to the workpiece grains. This can be achieved by conducting Crystal Plasticity Finite Element (CPFE) simulations. However, the material properties of copper in the meso-scopic domain, specific to atomic lattice orientation in individual grains, may not be readily available in the literature. Therefore, prior to CPFE simulations, detailed material characterization of copper can be considered.
- It would be interesting to see the experimental results for the force profile while punching with various slanted punch faces (single and symmetrical double slanted). Male dies can be fabricated with a slant angle by sanding and polishing a gage pin while mounted in a tool holder with a specific slant angle.

- When punching micro holes in copper foil with high production rates, strain rates may be very high, and therefore a strain rate sensitive material model must be used. In order to predict the repeatability in quality of the punched holes, a strain rate sensitive CPFEE model can be used.
- The research on maximum achievable porosity can be extended to see the effect of film thickness and hole diameter. A smaller hole diameter will have a higher curvature and hence may prevent twisting of the web while punching near a pre-existing hole. This could result in a lower minimum web thickness, which will increase the effective porosity. Also, it can be investigated if there lies a cross coupling between film thickness and hole diameter while predicting maximum achievable porosity.

References

- [1] U.S. Department of Health & Human Services, The Office of Minority Health, Organ Donation Data/Statistics. <<http://minorityhealth.hhs.gov/templates/browse.aspx?lvl=3&lvlid=555>>. (accessed on 1 September 2013)
- [2] Novosel, E. C., Kleinhans, C. and Kluger, P. J., 2011, "vascularization is the key challenge in tissue engineering," *Adv. Drug Deliv. Rev.*, **63**, pp. 300-311.
- [3] Freed, L.E., Engelmayer, G.C., Borenstein, J.T., Moutos, F.T., and Guilak, F., 2009, "Advanced material strategies for tissue engineering scaffolds," *Adv. Mater.*, **21**(32-33), pp. 3410-3418.
- [4] Schmitt, E. C., 2013, "Design and Development of a Stamping Press Capable of Punching Microscale Holes in Polymer Membranes," MS Thesis, Tufts University, Medford, MA.
- [5] "Blanking and piercing" http://en.wikipedia.org/wiki/Blanking_and_piercing (accessed on August 29, 2014).
- [6] U.S. Department of Health & Human Services, Donate The Gift of Life, The Need Is Real: Data. <<http://organdonor.gov/about/data.html>>. (accessed on 1 September 2013)
- [7] Zorlutuna, P., Annabi, N., Camci-Unal, G., Nikkhah, M., Cha, J. M., Nichol, J. W., Manbachi, A., Bae, H., Chen, and S., Khademhosseini, A., 2012, "Microfabricated Biomaterials for Engineering 3D Tissues," *Adv. Mater.*, **24**, pp. 1782-1804.
- [8] Kurtz, S., Ong, K., Lau, E., Mowat, F. and Halpern, M., 2007, "Projections of primary and revision hip and knee arthroplasty in the united states from 2005 to 2030," *J. Bone Joint Surg. Am.*, **89A**(4), pp. 780-785.
- [9] Liu, T. V., Chen, A. A., Cho, L. M., Jadin, K. D., Sah, R. L., DeLong, S., West, J. L., and Bhatia, S. N., 2007, "Fabrication of 3D hepatic tissues by additive photopatterning of cellular hydrogels," *FASEB J.*, **21**, pp. 790-801.
- [10] Khademhosseini, A., Eng, G., Yeh, J., Fukuda, J., Blumling, J. III, Langer, R., and Burdick, J. A., 2006, "Micromolding of photocrosslinkable hyaluronic acid for cell encapsulation and entrapment," *J. Biomed. Mater. Res.* **79A**: pp. 522-532.
- [11] Kane, R. S., Takayama, S., Ostuni, E., Ingber, D. E., and Whitesides, G. M., 1999, "Patterning proteins and cells using soft lithography," *Biomaterials*, **20**, pp. 2363-2376.
- [12] Rivest, C., Morrison, D. W. G., Ni, B., Rubin, J., Yadav, V., Mahdavi, A., Karp, J. M., and Khademhosseini, A., 2007, "Microscale Hydrogels For Medicine And Biology: Synthesis, Characteristics And Applications" *J. Mech. Mater. Struct.*, **2**(6), pp. 1103-1119.
- [13] Yeh, J., Ling, Y., Karp, J. M., Gantz, J., Chandawarkar, A., Eng, G., Blumling, 3rd. J., Langer, and R., Khademhosseini, A., 2006, "Micromolding of shape-controlled, harvestable cell-laden hydrogels," *Biomaterials*, **27**, pp. 5391-5398.
- [14] Lu, Y., Mapili, G., Suhali, G., Chen, S. C., and Roy, K., 2006, "A digital micro-mirror device-based system for the microfabrication of complex, spatially patterned tissue engineering scaffolds," *J. Biomed. Mater. Res.*, **77A**, pp. 396-405.

- [15] Han, L-H., Suri, S., Schmidt, C. E., and Chen, S., 2010, "Fabrication of three-dimensional scaffolds for heterogeneous tissue engineering" *Biomed. Microdevices*, **12**, pp. 721-725.
- [16] Mapili, G., Lu, Y., Chen, S., and Roy, K., 2005, "Laser-layered microfabrication of spatially patterned functionalized tissue-engineering scaffolds," *J. Biomed. Mater. Res. B Appl. Biomater.*, **75B**, pp. 414-424.
- [17] Williams, J. M., Adewunmi, A., Schek, R. M., Flanagan, C. L., Krebsbach, P. H., Feinberg, S. E., Hollister, and S. J., Das, S., 2005, "Bone tissue engineering using polycaprolactone scaffolds fabricated via selective laser sintering," *Biomaterials*, **26**, pp. 4817-4827.
- [18] Shuai, C., Gao, C., Nie, Y., Hu, H., Zhou, and Y., Peng, S., 2011, "Structure and properties of nano-hydroxyapatite scaffolds for bone tissue engineering with a selective laser sintering system" *Nanotechnology*, **22**, 285703
- [19] Liu, F. H., Chen, S. H., Lee, R. T., Lin, W. S., and Liao, Y. S., 2011, "Bioceramic Scaffolds Fabrication by Rapid Prototyping Technology," *Proc. World Acad. Sci. E*, **52**, pp. 214-216.
- [20] Bukharova, T. B., Antonov, E. N., Popov, V. K., Fatkhudinov, T. K., Popova, A. V., Volkov, A. V., Bochkova, S. A., Bagratashvili, V. N., and Gol'Dshtein, D. V., 2010, "Biocompatibility of Tissue Engineering Constructions from Porous Polylactide Carriers Obtained by the Method of Selective Laser Sintering and Bone Marrow-Derived Multipotent Stromal Cells," *Bull. Exp. Biol. Med.*, **149**, pp. 148-153.
- [21] Eshraghi, S. and Das, S., 2010, "Mechanical and microstructural properties of polycaprolactone scaffolds with one-dimensional, two-dimensional, and three-dimensional orthogonally oriented porous architectures produced by selective laser sintering," *Acta Biomater.*, **6**, pp. 2467-2476.
- [22] Duan, B., Cheung, W. L., and Wang, M., 2011, "Optimized fabrication of Ca-P/PHBV nanocomposite scaffolds via selective laser sintering for bone tissue engineering," *Biofabrication*, **3**, 015001
- [23] Duan, B., Wang, M., Zhou, W. Y., Cheung, W. L., Li, Z. Y., and Lu, W. W., 2010, "Three-dimensional nanocomposite scaffolds fabricated via selective laser sintering for bone tissue engineering," *Acta Biomater*, **6**, pp. 4495-4505.
- [24] Eosoly, S., Brabazon, D., Lohfeld, S., and Looney, L., 2010, "Selective laser sintering of hydroxyapatite/poly-ε-caprolactone scaffolds" *Acta Biomater*, **6**, pp. 2511-2517.
- [25] Antonov, E. N., Bagratashvili, V. N., Whitaker, M. J., Barry, J. J. A., Shakesheff, K. M., Kononov, A. N., Popov, and V. K., Howdle, S. M., 2005, "Three-Dimensional Bioactive and Biodegradable Scaffolds Fabricated by Surface-Selective Laser Sintering," *Adv. Mater.*, **17**, pp. 327-330.
- [26] Tai, H., Popov, V. K., Shakesheff, K. M., Howdle, and S. M., 2007, "Putting the fizz into chemistry: applications of supercritical carbon dioxide in tissue engineering, drug delivery and synthesis of novel block copolymers," *Biochem. Soc. Trans.*, **35**, pp. 516-521.
- [27] Tai, H., Mather, M. L., Howard, D., Wang, W., White, L. J., Crowe, J. A., Morgan, S. P., Chandra, A., Williams, D. J., Howdle, S. M., and Shakesheff, K. M., 2007, "Control Of Pore Size And Structure Of Tissue Engineering Scaffolds Produced By Supercritical Fluid Processing," *Eur. Cells Mater.*, **14**, pp. 64-77.
- [28] Kazarian, S. G., 2000, "Polymer Processing with Supercritical Fluids" *Polym. Sci, Ser. C*, **42**, pp. 78-101.

- [29] Annabi, N., Fathi, A., Mithieux, S. M., Weiss, A. S., and Dehghani, F., 2011, "Fabrication of porous PCL/elastin composite scaffolds for tissue engineering applications," *J. Supercrit. Fluids*, **59**, pp. 157-167.
- [30] Annabi, N., Mithieux, S. M., Weiss, A. S., and Dehghani, F., 2010, "Cross-linked open-pore elastic hydrogels based on tropoelastin, elastin and high pressure CO₂," *Biomaterials*, **31**, pp. 1655-1665.
- [31] Annabi, N., Nichol, J. W., Zhong, X., Ji, C., Koshy, S., Khademhosseini, A., Dehghani, F., 2010, "Controlling the Porosity and Microarchitecture of Hydrogels for Tissue Engineering," *Tissue Eng. B.*, **16**, pp. 371-383.
- [32] Park, J. S., Woo, D. G., Sun, B. K., Chung, H.-M., Im, S. J., Choi, Y. M., Park, K., Huh, K. M., and Park, K.-H., 2007, "In vitro and in vivo test of PEG/PCL-based hydrogel scaffold for cell delivery application," *J. Control. Release*, **124**, pp. 51-59.
- [33] Dadsetan, M., Hefferan, T. E., Szatkowski, J. P., Mishra, P. K., Macura, S. I., Lu, L., and Yaszemski, M. J., 2008, "Effect of hydrogel porosity on marrow stromal cell phenotypic expression," *Biomaterials*, **29**, pp. 2193-2202.
- [34] Kim, J. H., Lee, S. B., Kim, S. J., and Lee, Y. M., 2002, "Rapid temperature/pH response of porous alginate-g-poly(Nisopropylacrylamide) hydrogels," *Polymer*, **43**, pp. 7549-7558.
- [35] Horak, D., Hlidkova, H., Hradil, J., Lapcikova, M., Slouf, M., 2008, "Superporous poly(2-hydroxyethyl methacrylate) based scaffolds: Preparation and characterization," *Polymer*, **49**, pp. 2046-2054.
- [36] Draghi, L., Resta, S., Pirozzolo, M., and Tanzi, M., 2005, "Microspheres leaching for scaffold porosity control," *J. Mater. Sci. Mater. Med.*, **16**, pp. 1093-1097.
- [37] Gong, Y., Zhou, Q., Gao, C., and Shen, J., 2007, "In vitro and in vivo degradability and cytocompatibility of poly(L-lactic acid) scaffold fabricated by a gelatin particle leaching method," *Acta Biomater.*, **3**, pp. 531-540.
- [38] Salerno, A., Guarnieri, D., Iannone, M., Zeppetelli, S., and Netti, P. A., 2010, "Effect of Micro- and Macroporosity of Bone Tissue Three-Dimensional-Poly(e-Caprolactone) Scaffold on Human Mesenchymal Stem Cells Invasion, Proliferation, and Differentiation In Vitro," *Tissue Eng.*, **16**, pp. 2661-2673.
- [39] Salerno, A., Guarnieri, D., Iannone, M., Zeppetelli, S., Maio, E. Di., Iannace, S., and Netti, P. A., 2009, "Engineered I-bimodal poly(e-caprolactone) porous scaffold for enhanced hMSC colonization and proliferation," *Acta Biomater.*, **5**, pp. 1082-1093.
- [40] Zhang, J., Wu, L., Jing, D., and Ding, J. A., 2005, "A comparative study of porous scaffolds with cubic and spherical macropores," *Polymer*, **46**, pp. 4979-4985.
- [41] Suh, S. W., Shin, J. Y., Kim, J., Kim, J., Beak, C. H., Kim, D.-I., Kim, H., Jeon, S. S., and Choo, I.-W., 2002, "Effect of Different Particles on Cell Proliferation in Polymer Scaffolds Using a Solvent-Casting and Particulate Leaching Technique," *ASAIO J*, pp. 460-464.
- [42] Joo, B. Y., Oh, S. I., and Jeon, B. H., 2001, "Development of micro punching system," *CIRP Annals – Manuf. Technol.*, **50**(1), pp. 191-194.
- [43] Joo, B., Rhim, S., and Oh, S., 2005, "Micro-hole fabrication by mechanical punching process," *J. Mater. Process. Technol.*, **170**, pp. 593-601.
- [44] Rhim, S., H., Son, Y. K., and Oh, S. I., 2005, "Punching of ultra small size hole array," *CIRP Annals – Manuf. Technol.*, **54**(1), pp. 261-264.

- [45] Chern, G-L., Wu, Y-J. E., and Liu, S-F., 2006, "Development of a micro-punching machine and study on the influence of vibration machining in micro-EDM," *J. Mater. Process. Technol.*, **180**, pp. 102-109.
- [46] Chern, G-L. and Chuang, Y., 2006, "Study on vibration-EDM and mass punching of micro-holes," *J. Mater. Process. Technol.*, **180**, pp.151-160.
- [47] Chern, Gwo-Liang and Wang, Sen-De, 2007, "Punching of noncircular micro-holes and development of micro-forming," *Precision Engineering*, **31**, pp. 210-217.
- [48] Xu, J., Wang, C., Guo, B., Shan, D., Sugiyama, Y., and Ono, S., 2009, "Surface finish of micro punch with ion beam irradiation," *Transactions of Nonferrous Metals Society of China*, **19**, pp. 526-530.
- [49] Kolleck, R., Vollmer, R., and Veit, R., 2011, "Investigation of a combined micro-forming and punching process for the realization of tight geometrical tolerances of conically formed hole patterns," *CIRP Annals – Manuf. Technol.*, **60**, pp.331-334.
- [50] Di, J., Zhoua, M., Li, J., Li, C., Zhang, W., and Amoako, G., 2011, "Micro-punching process based on spallation delamination induced by laser driven-flyer," *Applied Surface Science*, **258**, pp. 2339-2343.
- [51] Xu, J., Guo, B., and Shan, D., 2011, "Size effects in micro blanking of metal foil with miniaturization," *Int. J. Adv. Manuf. Technol.*, **56**, pp. 515-522.
- [52] Xu, J., Guo, B., Wang, C., and Shan, D., 2012, "Blanking clearance and grain size effects on micro deformation behavior and fracture in micro blanking of brass foil," *Int. J. Mach. Tool. Manu.*, **60**, pp. 27-34.
- [53] Xu, J., Guo, B., Shan, D., Wang, C., Li, J., Liu, Y., and Qu, D., 2012, "Development of a micro-forming system for micro-punching process of micro-hole arrays in brass foil," *J. Mater. Process. Technol.*, **212**, pp. 2238-2246.
- [54] Domblesky, J. P. and Zhao, L., 2002, "Fracture criteria evaluation and finite element modeling of plate shearing," *Proc. Instn. Mech. Engrs.*, **216**, Part B, pp. 25-38.
- [55] Sun, J. S., Lee, K. H., and Lee, H. P., 2000, "Comparison of implicit and explicit finite element methods for dynamic problems," *J. Mater. Process. Technol.*, **105**, pp. 110-118.
- [56] Kim, J., Kang, Y. H., Choi, H. H., Hwang, S. M., and Kang, B. S, 2002, "Comparison of implicit and explicit finite-element methods for the hydroforming process of an automobile lower arm," *Intl.J. Manuf. Technol.*, **20**, pp. 407-413.
- [57] Lee, T. C., Chan, L. C., and Zheng, P. F., 1997, "Application of the finite-element deformation method in the fine blanking process," *J. Mater. Process. Technol.*, **63**, pp. 744-749.
- [58] Oh, S. I., Wu, W.T., Tang, J.P., and Vedhanayagam, A., 1991, "Capabilities and applications of FEM code DEFORM: the perspective of the developer," *J. Mater. Process. Technol.*, **27**, pp. 25-42.
- [59] Integrated 2D3D System Documentation – DEFORM v10.2.1 User Manual
- [60] Zhu, Y. Y., Cescotto, S., and Habraken, A-M., 1992, "A fully coupled elastoplastic damage modeling and fracture criteria in metalforming processes," *J. Mater. Process. Technol.*, **32**, pp. 197-204.
- [61] Cockcroft, M. G. and Latham, D. J., 1968, "Ductility and the Workability of Metals," *J. Inst. Metals*, **96**, pp. 33-39.
- [62] Domblesky, J. P. and Zhao, L., 2002, "Assessment of a finite element model for plate shearing," *Proceedings of the I MECH E Part B J. Eng. Manuf.*, **216**, pp. 519-529.

- [63] Huang, Y., June 1991, "A User-material Subroutine Incorporating Single Crystal Plasticity In The Abaqus Finite Element Program", Division of Applied Sciences, Harvard University, Cambridge, Massachusetts, 02138.
- [64] Shirkoohi, G. H., and Liu, J., 1994, "A Finite Element Method for Modeling of Anisotropic Grain-Oriented Steels," *IEEE T. Magn.*, **30**(2), pp. 1078-1080.
- [65] Glaessgen, E. H., Saether, E., Phillips, D. R., and Yamakov. V., 2006, "Multiscale Modeling of Grain-Boundary Fracture Cohesive Zone Models Parameterized from Atomistic Simulations," *AIAA 2006*, pp. 1674-1686.
- [66] Hu, L., Rollett, A.D., Iadicola, M., Foecke, T., and Banovic, S., 2011, "Constitutive Relations for AA 5754 Based on Crystal Plasticity," *Metal. Mater. Trans. A*, **43**, pp. 854-869.
- [67] Kim, G. Y., Ni, J., and Koc. M., 2007, "Modeling of the Size Effects on the Behavior of Metals in Microscale Deformation Processes," *Transactions of the ASME*, **129**, pp. 470-476.
- [68] Peng, L., Liu, F., Ni, J., and Lai, X., 2007, "Size effects in thin sheet metal forming and its elastic-plastic constitutive model," *Mater. Design*, **28**, pp. 1731-1736.
- [69] Penga, L., Lai, X., Leeb, H-J., Songb, J-H., and Nic, J., 2009, "Analysis of micro mesoscale sheet forming process with uniform size dependent material constitutive model," *Mater. Sci. Eng. A*, **526**, pp. 93-99.
- [70] Yun, W., Peilong, D., Zhenying, Xu., Hua, Y., Jiangping, W., and Jingjing, W., 2010, "A constitutive model for thin sheet metal in micro-forming considering first order size effects," *Mater. Design*, **31**, pp. 1010-1014.
- [71] Chan, W.L. and Fu, M.W., 2011, "Experimental studies and numerical modeling of the specimen and grain size effects on the flow stress of sheet metal in microforming," *Mater. Sci. Eng. A*, **528**, pp. 7674-7683.
- [72] Raulea, L. V., Goijaerts, A. M., Govaert, L. E., and Baaijens, F. P.T., 2001, "Size effect in the processing of thin metal sheets," *J. Mater. Proces. Technol.*, **115**, pp. 44-48.
- [73] Simons, G., Weippert, C., Dual, J., and Villain, J., 2006, "Size effects in tensile testing of thin cold rolled and annealed Cu foils," *Mater. Sci. Eng. A*, **416**, pp. 290-299.
- [74] Cao, J., Zhuang, W., Wang, S., and Lin, J., 2010, "Development of a VGRAIN system for CPFEM analysis in micro-forming applications," *Int. J. Adv. Manuf. Technol.*, **47**, pp. 981-991.
- [75] Yang, Y., 2013, "Simulating Heterogeneous Deformation in Polycrystalline Metals using Crystal Plasticity Finite Element Method," *J. Postdoctoral Research*, **1**(6), pp. 15-23.
- [76] Perstorp, Biodegradable CAPA Thermoplastics. 2003.
- [77] Pitt, C. G., Chasalow, F. I., Hibionada, Y. M., Klimas, D. M., and Schindler, A., 1981, "Aliphatic polyesters. I. The degradation of poly (ε-caprolactone) in vivo," *J. Appl. Polym. Sci.*, **26**, pp. 3779-3787.
- [78] Wehrenberg, R. H., 1981, "Lactic acid polymers: strong, degradable thermoplastics," *Mater. Eng.*, **94**(3), pp. 63-66.
- [79] Feng, X., Song, C., and Chen, W., 1983, "Synthesis and evaluation of biodegradable block copolymers of ε-caprolactone and D,L-lactide," *J. Polym. Sci. Polym. Lett.*, **21**(8), pp. 593-600.
- [80] Engelberg, I. and Kohn, J., 1991, "Physico-mechanical properties of degradable polymers used in medical applications: a comparative study," *Biomaterials*, **12**(3), pp. 292-304.

- [81] Vandamme, T.F. and Legras, R., 1995, "Physico-mechanical properties of poly(ecaprolactone) for the construction of rumino-reticulum devices for grazing animals," *Biomaterials*, **16**(18), pp. 1395-400.
- [82] Rosa, D. S., Neto, I. C., Calil, M. R., Pedroso, A. G., Fonseca, C. P., and Neves, S., 2004, "Evaluation of the thermal and mechanical properties of poly(ecaprolactone), low-density polyethylene, and their blends," *J. Appl. Polym. Sci.*, **91**(6), pp. 3909–3914.
- [83] Correlo, V. M., Boesel, L. F., Bhattacharya, M., Mano, J. F., Neves, N. M., Reis, and R. L., 2005, "Hydroxyapatite reinforced chitosan and polyester blends for biomedical applications," *Macromol. Mater. Eng.*, **290**(12), pp. 1157-1165.
- [84] Granado, A., Eguiazábal, J. I., and Nazábal, J., 2008, "Structure and mechanical properties of blends of poly(e-caprolactone) with a poly(amino ether)," *J. Appl. Polym. Sci.*, **109**(6), pp. 3892-3899.
- [85] Kurniawan, D., Nor, F. M., Lee, H. Y., and Lim, J. Y., 2011 "Elastic properties of polycaprolactone at small strains are significantly affected by strain rate and temperature," *Proceedings of the Institution of Mechanical Engineers, Part H: J. Eng. Med.*, **225**, pp. 1015-1020.
- [86] Wikipedia, Polycaprolactone,
< <http://en.wikipedia.org/wiki/Polycaprolactone>>. (accessed on 10 October 2013)
- [87] Qin, Y., 2010, *Micromanufacturing Engineering and Technology*, Elsevier, Burlington, MA, Chap. 1.
- [88] Geiger, M., Kleiner, M., Eckstein, N., and Engel, U., 2001, "Microforming," *CIRP Annals – Manuf. Technol.*, **50**(2), pp. 445-462.
- [89] Kalpakjian, S. and Schmid, S., 2007, *Manufacturing Processes for Engineering Materials*. Prentice Hall, Upper Saddle River, NJ, Chap. 2, pp. 32.37,43.
- [90] Oberg, E., Jones, F. D., Horton, H. L. and Ryffel, H. H., 2012, *Machinery's Handbook*, Industrial Press, New York, NY, Chap. 2.
- [91] "Coefficient of Friction" from Roymech:
http://www.roymech.co.uk/Useful_Tables/Tribology/co_of_frict.htm
(accessed on June 16, 2014).
- [92] Geiger, M., Vollersten, F., and Kals, R., 1996, "Fundamentals of the Manufacturing of Sheet Metal Microparts," *CIRP Annals – Manuf. Technol.*, **45**(1), pp. 277-282.
- [93] Hambli, R., 2002, "Design of Experiment Based Analysis for Sheet Metal Blanking Processes Optimisation", *Int. J. Adv. Manuf. Technol.*, **19**(6), pp. 403-410.
- [94] "Polycaprolactone"
<http://en.wikipedia.org/wiki/Polycaprolactone> (accessed on August 29, 2014).
- [95] "Glass transition"
http://en.wikipedia.org/wiki/Glass_transition (accessed on August 29, 2014).
- [96] Jerabek, M., Major, Z., and Lang, R.W., 2010, "Uniaxial compression testing of polymeric materials," *Polym. Test.*, **29**, pp. 302-309.
- [97] Standard Test Method for Compressive Properties of Rigid Plastics – ASTM D695-10